An investigation of the d(^{18}Ne,^{19}Ne*)p reaction and its astrophysical relevance

Alison M. Laird

Thesis submitted for the degree of Doctor of Philosophy

Department of Physics and Astronomy

University of Edinburgh

2000

Abstract

The reaction $^{15}O(\alpha, \gamma)^{19}Ne$ is one of the potential break-out reactions from the Hot CNO cycle to the rp-process. As such, it may play an important role in nuclear astrophysics for the understanding of energy generation rates and the synthesis of proton-rich nuclei in sites of explosive hydrogen burning, such as novae and X-ray bursters.

Experiments were performed at the radioactive ion beam facility, at Louvain-la-Neuve, Belgium, to test the validity of measuring indirectly the $^{15}O(\alpha, \gamma)^{19}Ne$ reaction rate. The method utilised was the population of excited states in ^{19}Ne and the observation of their α-decay. Information on the α branching ratios of the states of astrophysical interest, just above the α-threshold, allows the reaction rate to be calculated, provided other resonance properties, i.e. Γ_T, E_R and J^π, are known.

Excited states in ^{19}Ne were populated via an inverse $^{18}Ne(d,p)$ reaction on a deuterated polyethylene target. The reaction and decay products were measured in an experimental set up that comprised three silicon strip detector arrays, with a total of 320 detector elements. Two experiments were performed at $E_{lab} = 44.1$ MeV and $E_{lab} = 54.3$ MeV. The recoiling protons tagged the populated state and the detection of a coincident α-particle and heavy residue pair identified its decay.

Branching ratios for several states in ^{19}Ne were determined, showing the viability of this experimental approach. Optical model parameters were determined from ^{18}Ne elastic scattering on deuterons. DWBA calculations were performed and compared with experimental angular distributions to yield spectroscopic factors. The results were comparable with a previous measurement using a stable beam, despite the significantly lower beam intensity, and indicated that, provided the necessary beam intensity was available, this method would allow the measurement of the α branching ratio of the resonance of most astrophysical interest at 504 keV and thus the determination of the ^{15}O$(\alpha, \gamma)^{19}$Ne reaction rate.

Declaration

The experiments described in this thesis were carried out by myself and other members of the University of Edinburgh Nuclear Physics Group in collaboration with the Universities of Louvain-la-Neuve, Belgium and Catania, Italy. The data analysis and interpretation are my own work and this thesis has been written by myself.

Alison Laird

Acknowledgements

Contents

List of Figures

Chapter 1

Introduction and Motivation

This chapter describes the importance of radioactive ion beams, particularly in the field of nuclear astrophysics. A brief outline of nuclear astrophysics in the area of element synthesis is given to provide the background to the motivation for this thesis. Finally, current evidence supporting the need for further investigation of this topic is presented.

1.1 Radioactive Nuclear Beams

The advent of radioactive nuclear beams (RNB) has opened up many new areas of research both in nuclear physics and other scientific disciplines. In nuclear physics, the number of known nuclides has increased significantly, extending systematic studies of nuclear parameters along isobar, isotope and isotone chains. In nuclear structure, reactions involving light exotic nuclei led to the discovery of the neutron halo, initiating the extensive study of such stuctures. The production of superheavy nuclei and the study of shell struc-

ture for extreme proton-neutron ratios, as well as the probing of the neutron and proton driplines have all been made possible due to the availability of exotic beams. In fact, the areas of nuclear physics to benefit from radioactive ion beams are as varied as nuclear physics itself and so a comprehensive discussion is outwith the scope of this work. More detailed discussions, both of areas of study and of RIB facilities, can be found in [1], [2] and [3].

1.2 Nuclear Astrophysics

One of the areas to benefit from these new opportunities is the field of nuclear astrophysics. Nuclear astrophysics is the study of the origin and evolution of the chemical elements. Additionally, it endeavours to explain energy generation in various astrophysical scenarios, from main sequence burning to explosive sites, such as novae, supernovae and X-ray bursters. Astronomical observations provide information on individual examples as well as general trends which nuclear astrophysics attempts to interpret. Yet to understand these scenarios and to explain observed abundances, information on masses, lifetimes and other properties of radioactive nuclei are necessary, as are reaction rates involving these nuclei. Since the introduction of RNB facilities, new areas of the nuclear chart have opened up to study and so many of these key parameters have been measured. Despite these successes, much is still unknown and our current understanding often relies on theoretical estimates based on nuclear systematics. In depth reviews of the current position of nuclear astrophysics are given in [4], [5]and [6]. An account concentrating on radioactive beams and their importance for explosive scenarios can be found

in [7]. A very brief outline of the relevant details of nuclear astrophysics relating to nucleosynthesis is given below to provide a background to this work.

From the perspective of abundances, a good qualitative description is available and current nuclear knowledge has been able to explain the gross features, though in essence it is much as was presented in the highly influential paper 'B^{2}FH'[8] from 1957. Figure 1.1 shows the local galactic abundance chart, and an outline of the main features can be found in [9]. Our knowledge of the abundances of the elements arises from many disparate but possibly atypical sources. The composition of the earth's crust and of meteorites combined with knowledge of the solar wind, light from the sun and data from planetary probes allow a good description of Solar System abundances. Cosmic rays and spectra from distant stars and nebulae provide information on galactic abundances.

The current understanding of the origin of the elements is that hydrogen, most of the helium, and some traces of light elements were synthesised during the first few minutes of the Big Bang. Most other elements were produced either during the standard burning stages of stellar evolution or during explosive events that may occur during or at the end of a star's life. An overview of nucleosynthesis can be found in [10].
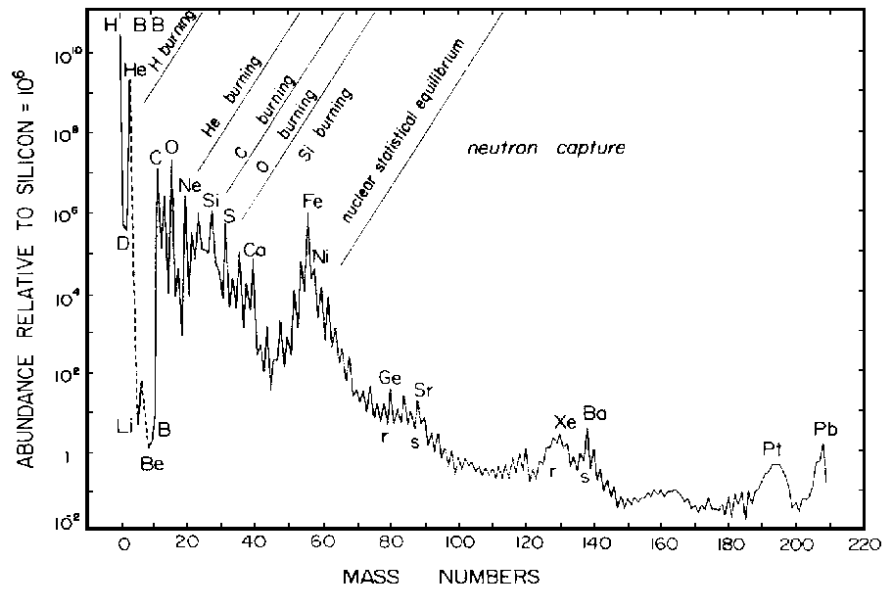
Figure 1.1: *The 'local galactic' abundance distribution of nuclear species, normalised to 10^6 ^{28}Si atoms, taken from Pagel[9].*

1.3 Primordial Nucleosynthesis

The main evidence in support of the Big Bang theory, over other cosmological theories such as the Steady State Theory[11], has been the observation of the cosmic microwave background and the discovery that all galaxies outside the locality are receding from each other. In 1929, Hubble announced that not only were the spectra from all galaxies outside the local group redshifted, but also that this redshift, or in other words the recession velocity of the galaxy, was proportional to the distance of the galaxy[11]. This led to the conclusion that the Universe is expanding. Then in 1965, Penzias and Wilson[12] observed a microwave background, as predicted by Gamow. The COBE (COsmic Background Explorer) satellite measured the background more accurately and fitted the data to a blackbody spectrum at 2.735 K[13].
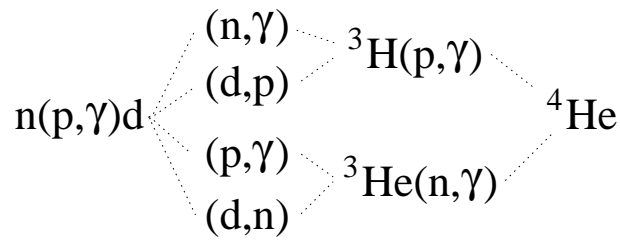
Figure 1.2: *Nuclear reactions producing helium during the Big Bang.*

More importantly, however, it showed this background to be isotropic to 1 part in 10^4[9]. These findings were consistent with the theory that the Universe had once been filled with radiation, which had cooled as the Universe expanded. These two features can only be explained by the theory that the Universe began as a singularity which expanded and cooled into the state in which we observe it at present.

An excellent account of all aspects of the Standard Model of the Big Bang is given in [13]. According to this model, significant rates of nucleosynthesis only occured after about 250s when the temperature of the Universe had fallen to 9×10^8K. Before this, the temperature was such that any deuterons formed were immediately dissociated by photons. Once this 'deuterium bottleneck' had been overcome, all available neutrons were quickly processed into helium via the reaction chains shown in figure 1.2.

Additional reactions producing ^{7}Li and ^{7}Be, which would decay to ^{7}Li, also occured. However, due to the lack of stable nuclei with A=5 or A=8, heavier nuclei were not produced. Additionally, the falling temperature reduced the probability that nuclei with Z>2 would have sufficient energy to overcome their mutual Coulomb repulsion. Therefore, the products of Big

Bang Nucleosynthesis were ^{1}H (75%[1]), ^{4}He(25%), with traces of ^{2}H, ^{3}He and ^{7}Li.

1.4 Hydrostatic Stellar Nucleosynthesis

This section gives an outline of stellar evolution and describes the formalism for calculating stellar reaction rates. Then a summary of the main nucleosynthetic processes that occur during each stage of a star's life is presented.

1.4.1 Stellar Evolution

The evolution and ultimate fate of a star are determined mainly by its mass though chemical composition also plays a role. A Hertzsprung-Russell diagram (H-R) plots a star's surface temperature against luminosity, an example of which is shown in figure 1.3. These diagrams are also known as luminosity-temperature or colour-magnitude diagrams. All stars lie in well defined bands on such a diagram, demonstrating that there is a relationship between luminosity and chromosphere temperature. Each band corresponds to different types of stars, such as red giants or white dwarfs, each of which correspond to different regimes in stellar evolution. For a star of given mass, its evolution can be followed on such a plot. Figure 1.4 shows the evolutionary path for a solar mass star.

The evolution of a star begins in the interstellar medium, which may have been seeded with material from previous generations of stars. The pro-

---

[1]The primordial He/H ratio is not due to nuclear effects but is dependent on the initial neutron/proton ratio, which is governed by the neutron decay properties.
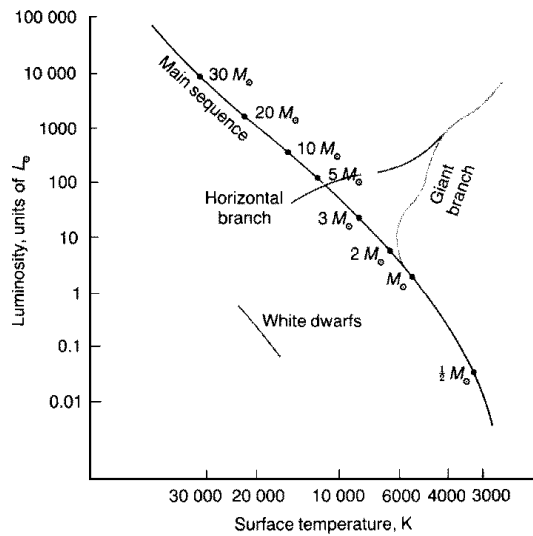
Figure 1.3: *A schematic Hertzsprung-Russell diagram for stars, taken from Longair[14].*

cess by which a gas cloud can collapse to form a star is still largely uncertain. Although the gross features can be explained, there remain several major problems, principally concerning energy and angular momentum[14], which are yet to be solved. In essence though, the gas cloud collapses under gravity and converts its gravitational potential energy into thermal(50%) and radiative(50%) energy, as described by the Virial Theorem[15]. Initially, this collapse is under freefall conditions, i.e. no internal pressure is assumed. Eventually the core reaches a critical density and becomes opaque to radiation. Trapped radiation helps to heat the core and collapse is slowed by the internal pressure. Matter continues to accrete onto the core. Finally if the mass is greater than $0.05 M_\odot$ the core temperature will be high enough ($> 10^6$K, 100 eV) for hydrogen burning to start and the resultant thermal pressure counteracts the effects of gravity, halting the inward collapse. The
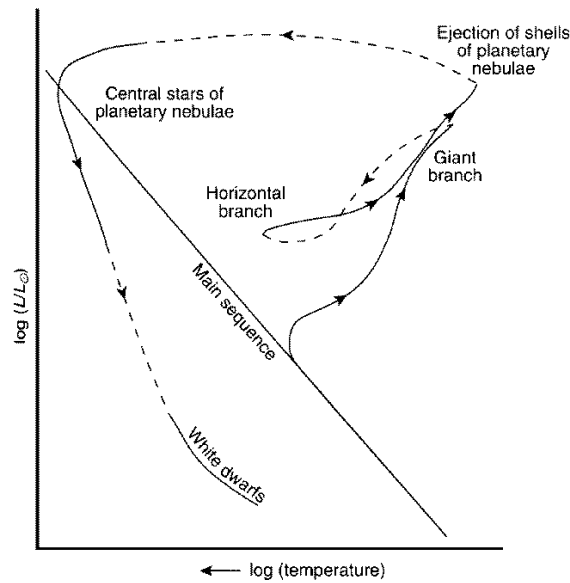
Figure 1.4: *Hertzsprung-Russell diagram showing the evolutionary path for a solar mass star, taken from Longair[14]. Regions where the evolution is not well defined are indicated by dashed lines.*

star is then said to be on the Main Sequence. Hydrogen burning may continue for many millions of years depending on the mass of the star. A massive star will use up its hydrogen within a few million years, whereas a star smaller than our sun may stay on the Main Sequence for more than 10 billion years. Once ten percent of the hydrogen has been consumed, a value known as the Schönberg-Chandrasekhar limit, the energy generation rate has fallen to such an extent that it is no longer sufficient to counter the gravitational forces and the helium core contracts. This contraction heats the shell of hydrogen surrounding the core which ignites. This causes the outer envelope to expand and the star leaves the Main Sequence becoming a red giant.

For stars of less than two to three solar masses, the core is supported by electron degeneracy pressure, in other words the Pauli Exclusion Principle. In this way the core resists gravitational collapse despite the lack of a nuclear energy source. The electrons form a degenerate gas in which the pressure depends on the density and is independent of temperature. Eventually the temperature is high enough to ignite helium burning. The onset of helium burning increases the core temperature significantly. However, since the core is degenerate it cannot respond by expanding and cooling. Consequently, the temperature increases, which in turn increases the rate of energy generation by helium burning leading to thermonuclear runaway known as a "helium flash". When the core temperature reaches 3.5 x 10^8 K (35 keV), the electrons become non-degenerate again and the core can then expand and cool, and helium burning continues under non-degenerate conditions. For stars more massive than this, helium burning commences before the core becomes degenerate.

Eventually, the star will exhaust its supply of helium and how it evolves from here depends critically on its mass. For stars with less than about $10M_{\odot}$, core helium burning is the beginning of the end. Once helium burning in the core stops, burning continues in a shell surrounding the core. As with hydrogen shell burning, this causes the envelope to expand. The carbon rich core becomes degenerate, and the star moves onto the asymptotic giant branch (AGB). Since helium burning is highly temperature dependent, helium shell burning is unstable. The expansion of the envelope causes the temperature and pressure to fall. This causes the energy generation rate also to fall.
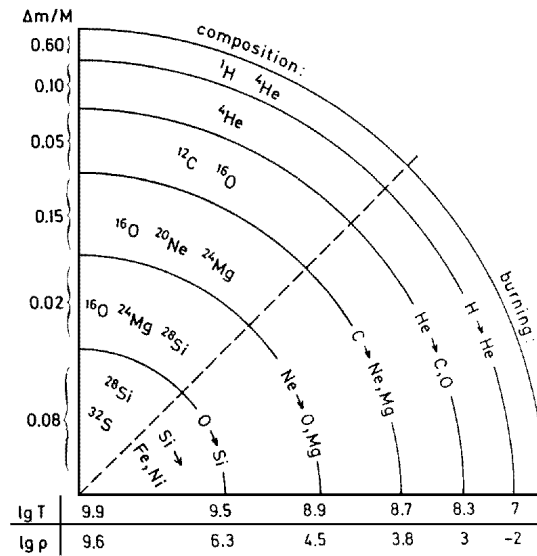
Figure 1.5: *A schematic diagram of the interior structure of a highly evolved star, taken from Longair[14].*

Consequently, the star contracts and the temperature and pressure increase, increasing the helium burning rate. This cycle continues and the bursts of thermonuclear activity are known as thermal pulses. However, these pulses lead to the loss of the star's outer layers. The expanding shell of material thrown off by the star is heated by the core and is known as a planetary nebula. Eventually, there is no longer enough material for shell burning. The core remains as a white dwarf supported by electron degeneracy, which will cool to a black dwarf in a few billion years.

For more massive stars, the core carbon burning occurs non-degeneratively. The star then burns progressively heavier elements, in a cycle of contraction, heating, onset of next burning stage and exhaustion of that fuel. In this way, the star ends up with a silicon burning core, surrounded by shells burning

oxygen, neon, carbon, helium and hydrogen, giving it an onion like structure as shown in figure 1.5. Once silicon burning in the core stops, energy can no longer be derived from fusion since the iron group elements are the most tightly bound. The core contracts under gravity and electron degeneracy pressure is insufficient to counter gravitational collapse. Photodisintegration reactions on the iron group elements occur in the core. These are endothermic and speed up the collapse. If the core collapse can be halted by neutron degeneracy pressure, the collapse will lead to a neutron star formation. This in turn creates a shock wave which propagates out through the star blowing off the outer layers in a Supernova Type II or related explosion. If the core is more then three solar masses however, even neutron degeneracy pressure is not enough and a black hole will result. The details of supernovae explosions are outwith the scope of this work and can be found in [16], [17] and [14].

1.4.2 Stellar Reaction Rate Calculation

The probability for two particles, a and b, to undergo a reaction b(a,c)d depends on the number of each type of particle, and the reaction cross section. Thus the reaction rate is given by:

$$R(ab \rightarrow cd) = N_a N_b \sigma(v) v \qquad (1.1)$$

where N_a = number density of particles of type a

N_b = number density of particles of type b

v = relative velocity of particles a and b

$\sigma(v)$ = velocity dependent cross section for the reaction b(a,c)d

With the exception of neutron stars, nuclei in the stellar interior are generally in a non-degenerate state and can be assumed to be in thermodynamic equilibrium. The distribution of relative velocities for all particle pairs, a and b, can be described by a Maxwell-Boltzmann distribution

$$\phi(v) = 4\pi v^2 (\frac{\mu}{2\pi kT})^{3/2} exp(\frac{-\mu v^2}{2kT}) \qquad (1.2)$$

where μ is the reduced mass and the other symbols have their usual meaning. The total reaction rate, summing over all velocity contributions, is given by

$$R(ab \rightarrow cd) = N_a N_b \int_0^\infty \sigma(v) v \phi(v) dv = N_a N_b < \sigma v > \qquad (1.3)$$

where $< \sigma v >$, the average value of the product of the relative velocity and cross section, is the reaction rate per particle pair. Using the formula, $E = \frac{1}{2} \mu v^2$, the reaction rate per particle pair can be rewritten in terms of relative energy as[17]

$$< \sigma v > = (\frac{8}{\pi\mu})^{1/2} (\frac{1}{kT})^{3/2} \int_0^\infty \sigma(E) E exp(\frac{-E}{kT}) dE \qquad (1.4)$$

1.4.2.1   Non-resonant Reaction Rate

To calculate $< \sigma v >$, information on the cross section as a function of energy is needed. In normal stellar environments, the average thermal energy of the nuclei is much less than the potential barrier due to their mutual Coulomb repulsion. Consequently, the cross section will be proportional to the probability to tunnel through this barrier. The cross section can be expressed as

$$\sigma(E) = \frac{S(E)}{E} exp(-2\pi\eta) \qquad (1.5)$$

where η is the Sommerfeld parameter, $\eta = Z_1Z_2e^2/\hbar\nu$. This equation defines the astrophysical S-factor which represents all the intrinsically nuclear parts of the cross section. In the absence of resonances, S(E) is a slowly varying function of energy and thus can be used to extrapolate to low energies where the cross section drops off rapidly. Taking the average value S_o, of S(E) over the relevant energies gives

$$< \sigma v >= (\frac{8}{\pi\mu})^{1/2}(\frac{1}{kT})^{3/2}S_o \int_0^\infty exp(\frac{-E}{kT} - 2\pi\eta)dE \qquad (1.6)$$

The first term in the exponential is due to the Maxwell-Boltzmann distribution which becomes small at high energies. The second term arises from the penetration probability through the Coulomb barrier and drops off rapidly at low energies. The result of these two factors is a peak in the reaction rate in the overlap region of the two functions. The reaction rate is only significant in the region of this peak, called the Gamow peak, which is at an energy higher than the average thermal energy. This is shown schematically in figure 1.6. The centroid of this peak is the effective mean energy for thermonuclear reactions at a temperature T and can be determined by taking the first derivative of the integrand

$$E_o = (\frac{bkT}{2})^{2/3} \qquad (1.7)$$

where $b = (2\mu)^{1/2}\pi e^2 Z_1 Z_2/\hbar$ and the other symbols have their usual meaning.

1.4.2.2   Resonant Reaction Rate

The above derivation for the cross section is only true in the absence of resonances in the compound system. If resonances are present, the enhancement in the cross section, and therefore reaction rate, due to the increased penetra-
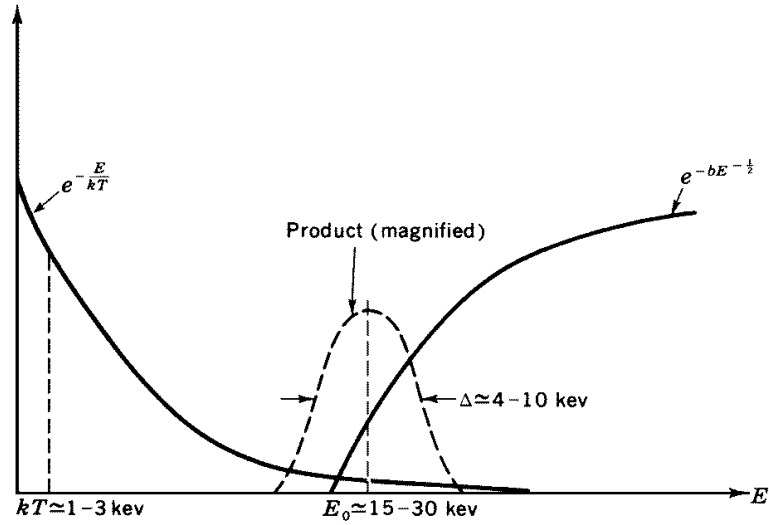
Figure 1.6: *The dominant energy-dependent factors in thermonuclear reactions, taken from Clayton[19]. The combination of the Maxwellian energy distribution and Coulomb barrier penetration function gives the Gamow peak (see text).*

tion probability can be described by the Breit-Wigner formalism. The cross section for a single narrow resonance is given by

$$\sigma_{BW}(E) = \pi \frac{\hbar^2}{2\mu E} \omega \frac{\Gamma_a \Gamma_c}{(E - E_R)^2 + (\frac{\Gamma}{2})^2} \tag{1.8}$$

where $\omega = \frac{2J+1}{(2J_a+1)(2J_b+1)}$ = statistical spin factor

J = angular momentum of excited state in compound nucleus

J_a = angular momentum of particle a

J_b = angular momentum of particle b

Γ_a = partial width of entrance channel

Γ_c = partial width of exit channel

Γ = total width of excited state in compound nucleus

E = relative energy of particles a and b

E_R = energy of resonance

A narrow resonance is one in which the total width, Γ, is much less than the energy of the resonance, E_R, and in this case the assumption is made that the Maxwell-Boltzmann function, Eexp(-E/kT), changes very little over a narrow resonance and so can be taken outside the integral. Rewriting 1.4 gives

$$< \sigma v >= (\frac{8}{\pi\mu})^{1/2}(\frac{1}{kT})^{3/2}E_R exp(\frac{-E_R}{kT})\pi\frac{\hbar^2}{2\mu E_R}\omega\Gamma_a\Gamma_c \int_0^\infty \frac{dE}{(E - E_R)^2 + (\Gamma/2)^2}$$
$$(1.9)$$

assuming negligible energy dependence of the partial and total widths. Integration gives

$$\int_0^\infty \frac{dE}{(E - E_R)^2 + (\Gamma/2)^2} = \frac{2\pi}{\Gamma} \qquad (1.10)$$

Finally, combining equations 1.9 and 1.10 gives[17]

$$< \sigma v >= (\frac{2\pi}{\mu kT})^{3/2}\hbar^2\omega\gamma exp(\frac{-E_R}{kT}) \qquad (1.11)$$

where $\gamma = \frac{\Gamma_a\Gamma_c}{\Gamma}$. Thus the important parameters are the resonance energies, E_R and the resonance strengths, $\omega\gamma$.

1.4.3   PP Chains

Hydrogen burning in main sequence stars can proceed via two different burning sequences. In the case of low mass stars, M < 1.5M$_\odot$[14], or those with low metallicity (low abundances of nuclei heavier than helium), the dominant mechanisms are the proton-proton (PP) chains. The overall result of the PP-chains is to convert four protons into a helium nucleus with the emission of two positrons and two neutrinos. The first reaction is the decay of a proton

$$p(p,e^+\nu)d$$

$$d(p,\gamma)^3He$$

$$^3He(^3He,2p)^4He \qquad\qquad ^3He(\alpha,\gamma)^7Be$$

$$^7Be(e^+,\nu)^7Li \qquad\qquad ^7Be(p,\gamma)^8B$$
$$^7Li(p,\alpha)^4He \qquad\qquad ^8B(e^+\nu)^8Be$$
$$^8Be(\alpha)^4He$$

PPI PPII PPIII
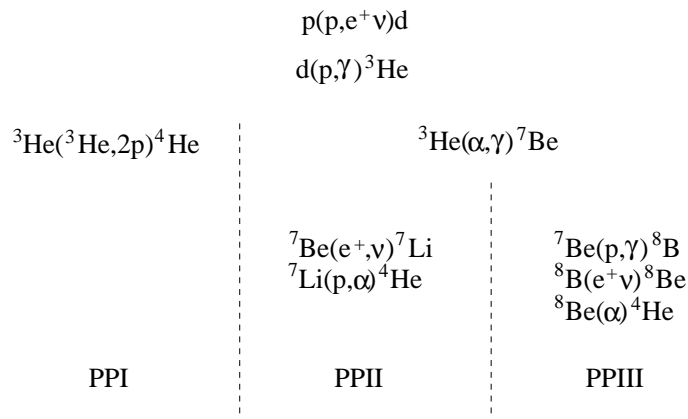
Figure 1.7: *The PP Chains.*

into a neutron within the field of a second proton: $p + p \rightarrow d + e^+ + \nu_e$. As this involves the weak interaction, this process is extremely slow and has such a low cross-section that only a theoretical estimate is currently possible[18]. The immediate consequence of this is the longevity of these stars on the main sequence. The next step is $d + p \rightarrow {}^3He + \gamma$. Subsequently, there are three possible chains[19], which are shown schematically in figure 1.7.

The importance of PPII and PPIII, however, depends on the amount of ${}^4He$ present and thus they contribute more to the energy production as the star evolves.

1.4.4 CNO cycles

In the case of more massive stars with significant amounts of heavier elements, i.e. Population I stars, hydrogen burning occurs predominantly via the carbon-nitrogen-oxygen (CNO) cycles. Predicted by Bethe[20] and von Weizsäcker[21, 22], these cycles convert hydrogen to helium using carbon as
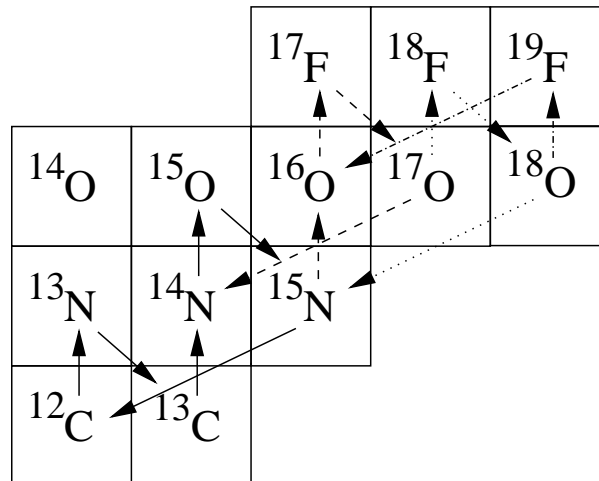
Figure 1.8: *The CNO cycles. The solid line denotes the CN cycle and the dashed line the ON cycle. The dotted and dashed-dotted lines indicate the CNO tri and quadricycles.*

a catalyst for a sequence of proton captures and β-decays as given below and shown schematically in figure 1.8

$$^{12}C(\alpha,\gamma)^{13}N(e^+\nu_e)^{13}C(p,\gamma)^{14}N(p,\gamma)^{15}O(e^+\nu_e)^{15}N(p,\alpha) \tag{1.12}$$
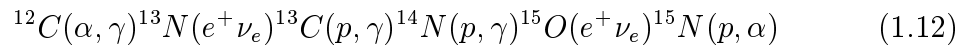
The overall result is the same as that of the PP-chains, i.e. $4p \rightarrow ^4He$ + $2e^+$ + $2\nu_e$, but the energy produced is higher. This is due to the β-decays being of low energy and thus the neutrinos carry away less kinetic energy. As higher charges and thus higher Coulomb barriers are involved, temperatures in excess of 2×10^7 K(2 keV) are necessary before the CNO cycle dominates the PP-chains. Figure 1.9 shows the temperature regimes where the PP-chains and the CNO cycles dominate. At these temperatures, the two β-decays are relatively fast and the reaction rate is determined by the proton captures and so $^{14}N(p,\gamma)$ or $^{15}N(p,\alpha)$ is expected to be the slowest reaction. However, since

the former involves the electromagnetic interaction while the latter is nuclear, it is the former which is the slowest and acts as a bottleneck. Consequently the main product of the CNO cycles is ^{14}N.
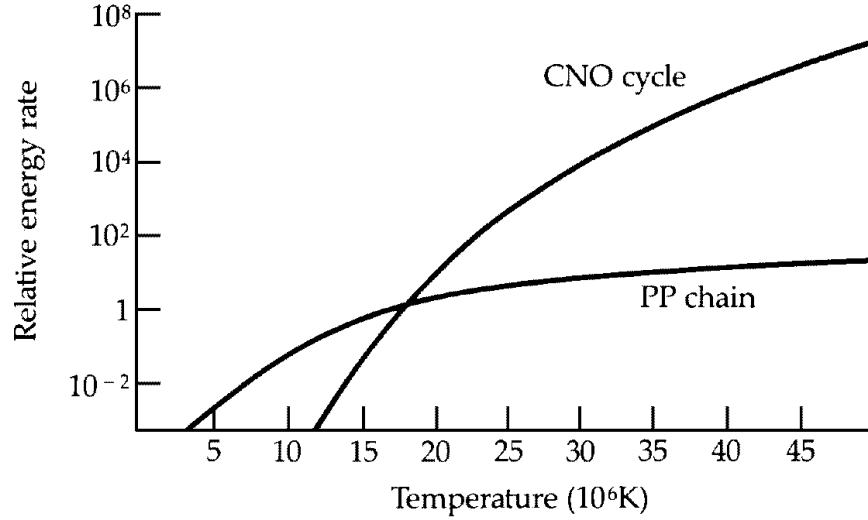
Figure 1.9: *Temperature dependence of energy generation rate for PP chains and CNO cycles for Population I stars, taken from Zeilik and Gregory[15]. Note the crossover at 18 million K.*

In addition to the main cycle, there are several other pathways which are possible and these are also shown in figure 1.8. While these are not expected to contribute greatly to the overall energy generation rate, the isotopes involved are interesting from a nucleosynthesis point of view. The ON cycle bypasses the ^{15}N(p,α) via the chain

$$^{15}N(p, \gamma)^{16}O(p, \gamma)^{17}F(e^+ \nu_e)^{17}O(p, \alpha)^{14}N \qquad (1.13)$$
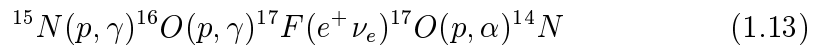
The CNO tricycle bypasses the ^{17}O(p,α) reaction by

$$^{17}O(p, \gamma)^{18}F(e^+ \nu_e)^{18}O(p, \alpha)^{15}N \qquad (1.14)$$
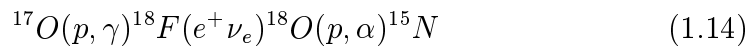
Finally, the CNO quadricycle bypasses the ^{18}O(p,α) by

$$^{18}O(p,\gamma)^{19}F(p,\alpha)^{16}O \qquad (1.15)$$

1.4.5 The NeNa and MgAl Cycles

At temperatures of several 10^7K, additional cycles for burning hydrogen to helium participate. Two important such cycles are the NeNa and MgAl cycles[5]. While these cycles contribute little towards energy production, due to the Coulomb barriers involved, they are nonetheless interesting for nucleosynthesis. The NeNa cycle follows the path

$$^{20}\text{Ne(p,}\gamma)^{21}\text{Na(e}^+\nu_e)^{21}\text{Ne(p,}\gamma)^{22}\text{Na(e}^+\nu_e)\ ^{22}\text{Ne(p,}\gamma)^{23}\text{Na(p,}\alpha)^{20}\text{Ne}$$
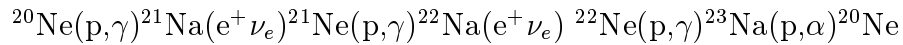
and is probably fed from the CNO cycles by the reaction ^{19}F(p,γ)^{20}Ne. This cycle is thought to explain the enrichment of ^{22}Ne found in meteorites[17].

The MgAl cycle is fed from the NeNa cycle by ^{23}Na(p,γ)^{24}Mg and subsequently follows the path

$$^{24}\text{Mg(p,}\gamma)^{25}\text{Al(e}^+\nu_e)^{25}\text{Mg(p,}\gamma)^{26}\text{Al}\ (\text{p,}\gamma)^{27}\text{Si(e}^+\nu_e)^{27}\text{Al(p,}\alpha)^{24}\text{Mg}$$
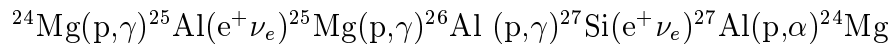
Alternatively, ^{26}Al has an isomeric state which β-decays and completes the cycle via

$$^{26}\text{Al(e}^+\nu_e)^{26}\text{Mg(p,}\gamma)^{27}\text{Al(p,}\alpha)^{24}\text{Mg}$$
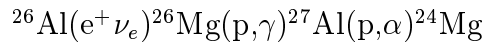
Suggested sites for these cycles include AGB stars[23] during hot-bottom burning (hydrogen burning at the bottom of the convective envelope) and red giants during the later stages of hydrogen shell burning. This has been backed up by observations of enhanced abundances of sodium and aluminium

in some red giants[9]. These cycles also participate to some extent in explosive hydrogen burning[24].

1.4.6   Helium Burning

Once the temperature has reached 10^8 K and the density is of the order of 10^4 gcm^{-3} helium undergoes burning to carbon via the triple alpha process. This mechanism bridges the mass-8 gap due to the relatively long lifetime of ^{8}Be. ^{8}Be is only unstable by 92 keV, and has a ground state width of 2.5 eV giving it a lifetime of 2.6 x 10^{-16} s[16]. This is considerably longer than one would expect for particle decay. Consequently, in the stellar interior, alpha particle collisions are sufficiently frequent compared to this lifetime that a small concentration of ^{8}Be builds up. For example, at 10^8 K with a density of 10^5 gcm^{-3} there is one ^{8}Be for every billion helium nuclei. It follows therefore that there is a certain probability for the reaction ^{8}Be + $\alpha \rightarrow ^{12}$C to occur. This reaction proceeds predominantly through a resonance in the compound system resulting in the carbon being populated in an excited state at E$_x$=7.65MeV(0^+) as was predicted by Hoyle[25]. This prediction was one of the great successes of nuclear astrophysics:

$$2\alpha \rightarrow ^8\text{Be } (-0.092\text{MeV})$$

$$^8\text{Be} + \alpha \rightarrow ^{12}\text{C}^{**}(7.65\text{MeV})(\gamma\gamma)^{12}\text{C(g.s.)}$$
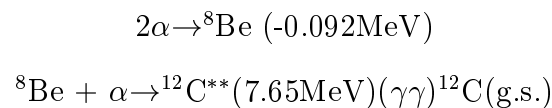
This state preferentially decays back to three alphas with an alpha width of 8.9 eV. However, a small number decay via a γ-ray cascade to the ground state, via the first excited state, with a gamma width of 3.6 meV. As stated previously, the triple-α process has been shown[17] to be highly

temperature dependent. For example, at 10^8 K the energy generation goes with the 41st power of the temperature (given in units of 10^8 K).

Further helium burning occurs via $^{12}\text{C}(\alpha,\gamma)^{16}\text{O}$ converting significant amounts of carbon to oxygen. The rate of this reaction is critical in determining the amount of carbon converted into oxygen and therefore the carbon/oxygen ratio in white dwarfs and the ejecta from massive stars. Consequently, much experimental effort has been undertaken on the measurement of this reaction (see e.g. [26], [27], [28] and references therein). However, these measurements cannot reach to sufficiently low temperatures due to the Coulomb barrier and so theoretical extrapolation is used to determine the rate. It is assumed that this reaction is non-resonant below about 2 x 10^9 K since it would otherwise proceed too quickly, processing too much carbon to explain the abundance observed today.

Under certain conditions, the temperature may rise as high as 10^9 K where advanced helium burning may proceed to neon and magnesium via the reaction path

$$^{16}\text{O}(\alpha,\gamma)^{20}\text{Ne}(\alpha,\gamma)^{24}\text{Mg}$$

Resonances in the ^{16}O-α system exist above the threshold but are presumed not to contribute due to spin and parity considerations. Consequently, the $^{16}\text{O}(\alpha,\gamma)^{20}\text{Ne}$ is thought to be non-resonant, although higher lying states may participate in later burning stages due to the higher temperatures. Thus this reaction, being much slower than the previous stage, effectively inhibits

further nucleosynthesis except in the case of very massive stars. Here the core temperatures are sufficient to allow the higher lying levels to participate so this reaction proceeds faster than ^{12}C$(\alpha,\gamma)^{16}$O. For temperatures higher than 0.2 x 10^9 K, ^{20}Ne$(\alpha,\gamma)^{24}$Mg is faster than ^{16}O$(\alpha,\gamma)^{20}$Ne and so helium burning in this regime does not result in much ^{20}Ne.

During helium burning, other nucleosynthetic processes are thought to occur. In second-generation stars, helium burning on other nuclei present will also contribute to nucleosynthesis. Some of these reactions produce neutrons, i.e. (α,n), which are very important for the synthesis of neutron-rich nuclei. In particular, ^{14}N is abundant in red giants being a major product of the CNO cycles. Radiative alpha capture on this nuclide produces ^{18}F which beta decays to ^{18}O. For temperatures below 0.2 x 10^9 K, the oxygen radiatively captures an alpha particle to give ^{22}Ne which also alpha captures resulting in ^{25}Mg and a neutron. For temperatures above this, the alpha capture on oxygen produces ^{21}Ne and a neutron. Thus in both temperature regimes, ^{14}N acts as a source of neutrons. Slow neutron capture (s-process) in the cores of massive stars is capable of producing nuclei up to the N=50 closed shell. The same process in intermediate mass stars occuring in the interaction area between H and He burning shells, could synthesise most of the heavier s-process nuclei from arsenic to lead. Once again, a detailed description of the s-process is outwith the scope of the present work, and the reader is advised to refer to [5], [9] and e.g. [29].

1.4.7   Advanced Burning Stages

If the core temperature reaches 6 x 10^8 K (60 keV), carbon burning can commence. Carbon burning progresses via many reactions and the most important are given below:

$$^{12}C + ^{12}C \rightarrow \begin{cases} ^{23}Na + p, \\ ^{20}Ne + \alpha, \\ ^{23}Mg + n, \\ ^{24}Mg + \gamma \end{cases} \qquad (1.16)$$
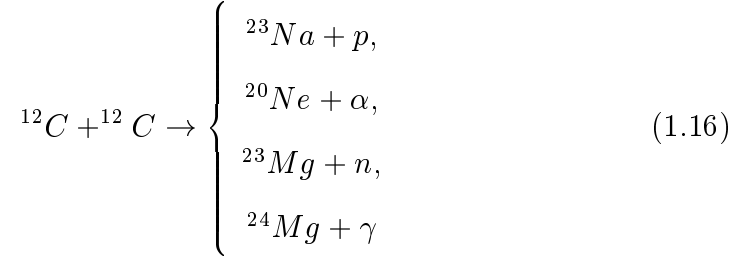
The main products of these reactions are ^{23}Na, ^{20}Ne, p and α. However, the protons and alphas react with other nuclei present and at the end of carbon burning material is mainly in the form of ^{16}O, ^{20}Ne, ^{23}Na, ^{24}Mg and ^{28}Si.

After the carbon fuel is exhausted, neon and oxygen burning start. Neon burning proceeds through photodisintegration rearrangement. This occurs at a temperature of around 1.3 x 10^9 K via the reaction:

$$^{20}Ne + \gamma \rightarrow ^{16}O + \alpha \qquad (1.17)$$

feeding the oxygen burning. This can be accompanied by radiative alpha capture reactions, namely:

$$^{20}Ne(\alpha, \gamma)^{24}Mg \qquad (1.18)$$

and

$$^{24}Mg(\alpha, \gamma)^{28}Si \qquad (1.19)$$

The reactions shown below are the main pathways for oxygen burning. There are a wide range of products, the main ones being ^{28}Si and ^{32}S.

$$^{16}O +^{16}O \rightarrow \begin{cases} ^{32}S + \gamma, \\ ^{31}P + p, \\ ^{31}S + n, \\ ^{28}Si + \alpha, \\ ^{24}Mg + 2\alpha \end{cases} \tag{1.20}$$
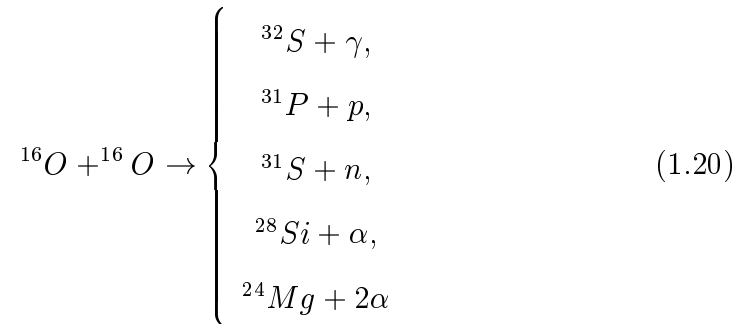
The final stage is silicon burning which starts at a core temperature of about 2.7 x 10^9 K. A large number of photodisintegration rearrangement reactions occur. The high gamma ray fluxes present strip nuclei of protons, neutrons and alphas in (γ,p), (γ,n) and (γ, α) reactions. These liberated particles are then recaptured by other nuclei. This process tends to break up loosely bound nuclei and form more tightly bound nuclei. Eventually, this leads to a build up of the most tightly bound nuclei, the iron peak elements, such as Cr, Mn, Fe, Co and Ni.

1.5 Explosive Stellar Environments

This section gives a brief description of explosive stellar scenarios relevant to the current work, namely novae and X-ray bursters. It is acknowledged that other explosive environments, in particular supernovae, are important sites of nucleosynthesis. However, it is not possible to give an adequate description of this vast topic here and so the reader is advised to refer to e.g. [30], [31] and [32] for a full discussion of those scenarios not covered here.

1.5.1 Novae

Novae are the third most violent explosions observed in the Universe after gamma ray bursts and supernovae. A nova is generally understood as being a thermonuclear runaway occuring in the hydrogen rich accreted envelope of a white dwarf in a binary system. The companion has filled its Roche Lobe and material passes through the inner Lagrangian point into the Roche Lobe of the white dwarf. This material forms an accretion disc around the white dwarf and spirals inwards onto the surface. This material, mainly consisting of hydrogen, builds up on the surface raising the temperature. However, it does so degenerately and thus there is no corresponding expansion to relieve the pressure. Eventually, the temperature has increased so much that the material suddenly becomes non-degenerate and the pressure is released by blowing off the outer layers of the star in a nova explosion. The nova ejecta typically have masses in the range 10^{-7} to 10^{-3} $M_\odot$.

Two types of white dwarf cores have been identified based on observations of novae ejecta. In addition to the carbon-oxygen (CO) white dwarf, oxygen-neon-magnesium (ONeMg) white dwarfs have been observed[33], characterised by strong emission lines of oxygen, neon and magnesium.

Observations of novae ejecta have shown that the abundances are highly non-solar and indicate that there is significant mixing between accreted and core material. Novae are thought to be important contributors to Galactic abundances for selected nuclear species. For example, significant amounts of ^{13}C, ^{15}N, ^{17}O and ^{26}Al may originate from novae[49]. Simulations of novae outbursts can be found in, for example, [35], [36], [37] and [33].

1.5.2   X-ray bursters

X-ray bursters are similar to novae but have a neutron star in place of the white dwarf. The gravitational field, therefore, is significantly greater and it is unclear if the material ejected has sufficient energy to escape or will instead fall back onto the surface. A review of this topic can be found in [38].

1.6   Explosive Nucleosynthesis

1.6.1   The Hot CNO Cycle

In these explosive scenarios, temperatures in the range 0.1-1.5 x 10^9 K and densities between 10^3 and 10^8 gcm^{-3} are typically encountered[39]. At these temperatures, the reaction ^{13}N(p,γ)^{14}O dominates the β-decay of ^{13}N turning the classical CNO cycle into the so-called hot CNO (HCNO) cycle. The HCNO cycle follows the path

$$^{12}C(p,\gamma)^{13}N(p,\gamma)^{14}O(e^+\nu_e)^{14}N(p,\gamma)^{15}O(e^+\nu_e)^{14}N(p,\alpha)^{12}C \qquad (1.21)$$
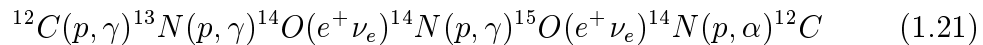
and is expected to dominate energy production. The fluorine isotopes ^{15}F and ^{16}F are proton unstable so no proton capture on ^{14}O and ^{15}O occurs and the rate of energy generation is limited by these two β-decays. Material then accumulates as ^{14}O(T$_{1/2}$=71 s) and ^{15}O(T$_{1/2}$=122 s). Due to its longer half-life, most of the material is in the form of ^{15}O and so the main product of the hot CNO cycle is ^{15}N. The relative abundance of ^{14}N to ^{15}N gives a signature of which CNO cycle has occurred. For the standard CNO cycles [^{14}N/^{15}N] is about 10^5, while for the hot CNO cycle this value is nearer 0.5.
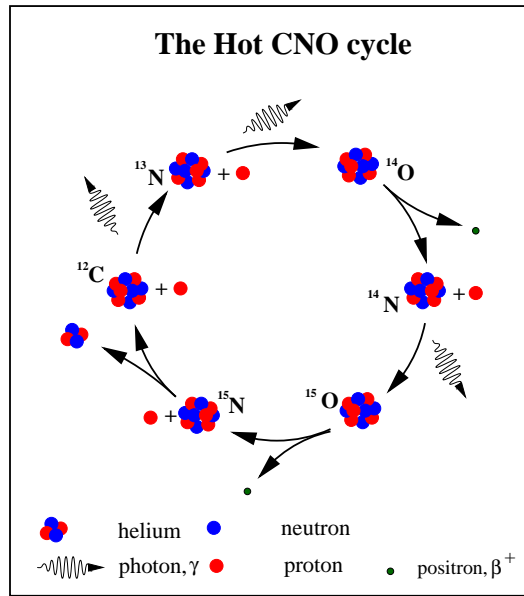
Figure 1.10: *The Hot CNO cycle.*

At higher temperatures (0.4×10^9 K) the ^{14}O bottleneck is bypassed by the chain

$$^{14}O(\alpha,p)^{17}F(p,\gamma)^{18}Ne(e^+\nu_e)^{18}F(p,\alpha)^{15}O \qquad (1.22)$$
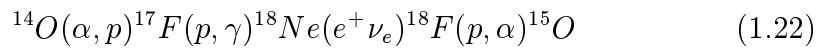
further enhancing the amount of ^{15}O and increasing the energy generation rate.

1.6.2 Hot CNO Cycle Breakout

However, if high enough temperatures (4×10^8 K) and densities are reached, the β-decay of ^{15}O will be superseded by radiative α-capture to ^{19}Ne[40]. The reaction pathway $^{15}O(\alpha,\gamma)^{19}$Ne(p,$\gamma$)^{20}Na then allows material to leave the HCNO cycles and be processed to higher masses by the rapid proton or rp-process. The second of these two stages has been measured by Vancraeynest

et al.[41]. Limits on the reaction rate were determined and it was shown that the first stage, $^{15}O(\alpha, \gamma)$, is the slower of the reactions and so it is this reaction which determines the rate of breakout.

An alternative breakout is the $^{18}Ne(\alpha,p)^{21}Na$ reaction. This reaction has been measured directly by Bradfield-Smith et al.[42, 43] and, more recently, by Groombridge et al.[44]. The first of these measurements was compared with theoretical predictions[45] and found to be in reasonable agreement. The temperatures required however for this reaction to supersede the β-decay of ^{18}Ne are such that this breakout path is only likely to contribute significantly in the case of accretion on the surface of a neutron star.

1.6.3 The rp-process

Once breakout has occured, material is processed by a sequence of proton capture reactions (rp-process) to higher masses. However, the rp-process may also occur without HCNO breakout if there is a sufficient abundance of intermediate mass nuclei already present. The path of the rp-process lies between the proton drip-line and the line of stability and is determined by competition between (p,γ), (α,γ), (α,p) reactions and β-decays. At low temperatures, the β-decays dominate and the path lies near the stability line. For higher temperatures, other reactions dominate and the path moves out towards the drip-line. The flow of material towards higher masses is impeded by waiting points, reaction cycles and photodisintegration reactions. In addition to proton-rich nucleosynthesis, the rp-process is responsible for a massive increase in energy production. Estimates suggest that the energy generation rate is increased by a factor of 100 over the hot CNO cycle[40].

Network calculations endeavour to simulate the flow of material through these reactions and hence predict energy generation rates and resultant abundances for different scenarios. These calculations rely on nuclear systematics but can be useful for identifying key reactions and thus concentrating experimental effort. References for such network calculations can be found in [46]. Such calculations predict that nuclei as heavy as mass 100 can be synthesised in the case of X-ray bursts[47, 48].

1.7 Observational Evidence

There have been many observations of novae ejecta in many regions of the electromagnetic spectrum, from infra-red studies[49], through the visible[50], into the ultraviolet, e.g. [51] and above. A recent paper by Starrfield[52] summarised several observations and noted what seemed to be general characteristics of novae ejecta abundances. Typically, the helium abundance is enhanced with respect to hydrogen, and CNO nuclei are also enhanced. About 25% of the novae observed show strong enrichment of neon and these cases often exhibit overabundances of Z>10 nuclei such as magnesium, aluminium and silicon.

This enhanced abundance of neon may be observational evidence for HCNO breakout occurring during a nova outburst via the reaction path:

$$^{15}O(\alpha, \gamma)^{19}Ne(p, \gamma)^{20}Na(p, \gamma)^{21}Mg(e^+\nu_e)^{21}Na(p, \gamma)^{22}Mg(e^+\nu_e)^{22}Na(e^+\nu_e)^{22}Ne$$

$$(1.23)$$
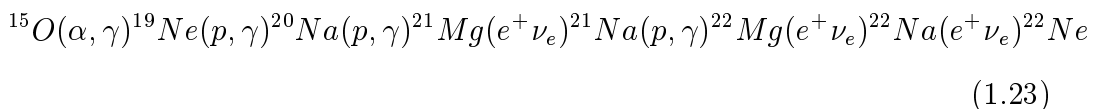
This neon enrichment should be accompanied by enhancement of nuclei with Z>10 and a depletion of CNO isotopes since material has been processed

away from the HCNO cycle up to higher masses.

However, this ignores the possible mixing of core material into the accreted material and its processing during explosive burning. In the case where the core is an ONeMg white dwarf, this would lead to increased abundance of neon due to core material, as well as higher Z nuclei from reactions on this material. Another feature of this case would be the depletion of carbon and oxygen. This is due to the build up of ^{14}O and ^{15}O during the HCNO cycle and their subsequent decay to ^{14}N and ^{15}N. The lack of carbon in the core adds to the carbon depletion.

Nevertheless, recent results from Werner and Wolff[53] on a post-AGB star entering the white dwarf stage show enhancements of the neon abundance of 20-50 times solar, as well as strong oxygen lines. The calculated mass indicates that this is a ONeMg white dwarf. This leads to the hypothesis that neon abundances in considerable excess of this figure, in novae ejecta, would be due to HCNO breakout rather than merely a mixing of core material from a ONeMg white dwarf. Ejecta with such overabundances of neon have been discussed in [51], [54] and [55]. Moreover, analysis of novae ejecta and comparison with nova models by Wiescher et al.[24] indicates that not all observations of high neon abundances can be explained by the mixing of ONeMg core material but that evidence suggests that HCNO breakout has indeed occured.

In the case where the mass of the white dwarf indicates that the core consists of carbon and oxygen, significant amounts of higher Z material cannot be produced without HCNO breakout due to the lack of seed nuclei. There will be, however, enhanced abundances of carbon, nitrogen and oxygen. The

nitrogen results, as before, from HCNO processing and the carbon and oxygen from core material.

Therefore, signatures of HCNO breakout occurring in novae can be summarised as follows. In the case of ONeMg cores, the enhancement of neon above that expected for mixing of core material will be observed. In addition, there will be an enhancement of nuclei with A higher than 20 together with a depletion of carbon and mitrogen. For CO cores, enhancements of carbon, neon and nuclei with A higher than 20 will be observed as well as the depletion of nitrogen.

1.8   The Present Work

In order to understand the origin and abundances of the proton-rich elements a detailed knowledge of the rp-process is required. Reaction rate information is needed to comprehend the path followed by the rp-process and the resultant energy generation. However, to achieve this it is necessary to understand the conditions that lead to the onset of the rp-process and the importance of the HCNO breakout in these scenarios. It has already been shown that in the conditions found in novae and X-ray bursters, the reaction $^{15}O(\alpha, \gamma)^{19}Ne$ plays a key role in breakout and thus a good knowledge of its reaction rate is important for not only understanding HCNO breakout but also the subsequent rp-process. The $^{15}O(\alpha, \gamma)^{19}Ne$ reaction rate is dominated by resonances[39] and figure 1.11 shows part of the ^{19}Ne level scheme above the α threshold. A full level scheme is given in appendix A.1. Using both theoretical and experimental data on the parameters of these resonances, Magnus et al.[56]

Ex	J^π		Ecm[keV]
5.092	$5/2^+$	———	1563
4.712	$5/2^-$		1183
4.635	$13/2^+$		
4.600	$5/2^+$		1071
4.549	$3/2^-$		
4.379	$7/2^+$	———	850
4.197	$7/2^-$	———	
4.140	$9/2^-$		
4.033	$3/2^+$	———	504
3.529			
		$^{15}O + \alpha$	
[MeV]		^{19}Ne	
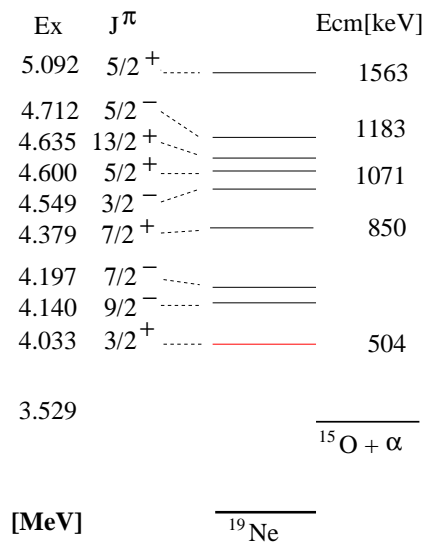
Figure 1.11: *The ^{19}Ne level scheme for the first nine levels above the α-threshold.*

calculated the contribution of each of these resonances to the total reaction rate and the result is shown graphically in figure 1.12. This shows that at typical novae temperatures the reaction rate is dominated by the 4.033 MeV state, while in X-ray bursters the 4.600 MeV state will dominate. While the 4.600 MeV parameters have been determined experimentally[56], those of the 4.033 MeV state have only been calculated theoretically[57].

The present work aims to investigate the viability of an indirect method for determining the parameters of the 4.033 MeV level in ^{19}Ne. This method involves populating states in ^{19}Ne via an inverse (d,p) reaction with a ^{18}Ne beam, and measuring the α-^{15}O decay of the relevant states.
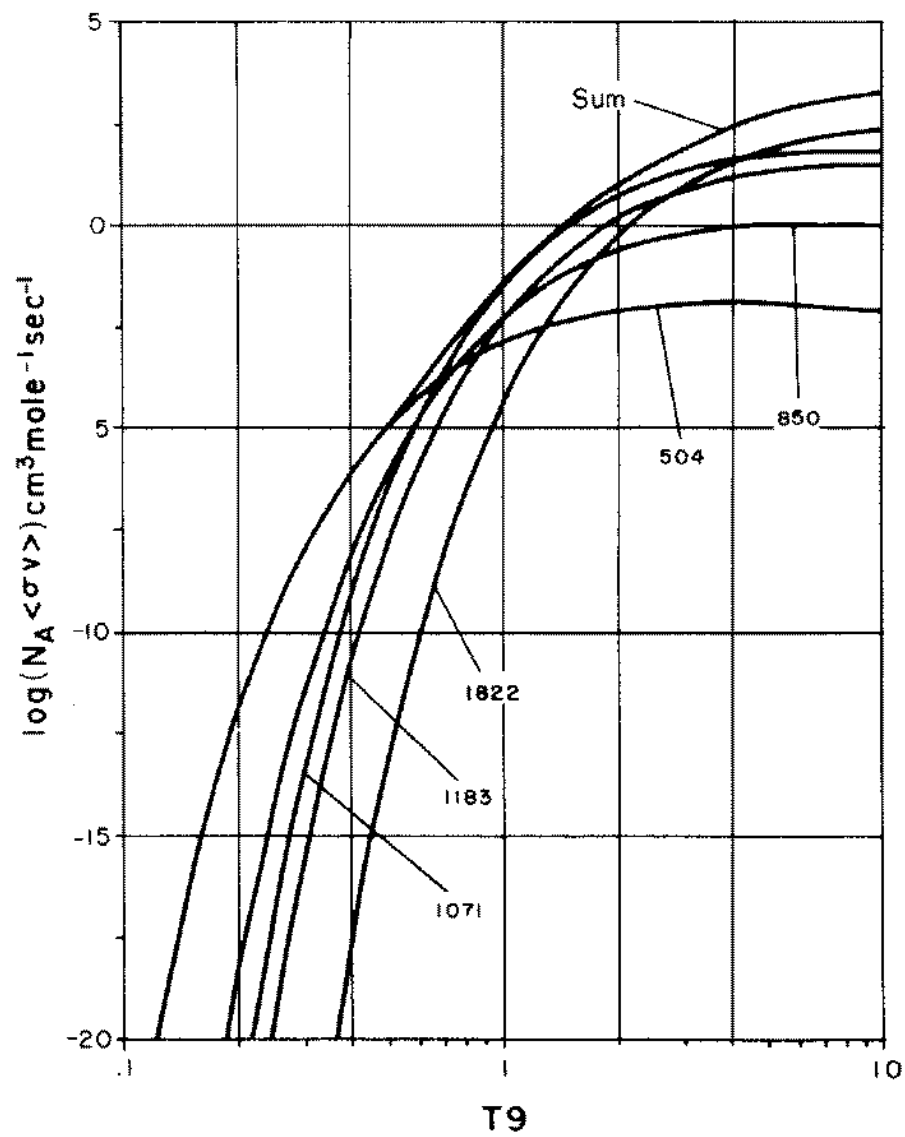
Figure 1.12: *Reaction rate calculation taken from Magnus et al.[56]. Temperatures are given in billions of Kelvin (10^9 K).*

Chapter 2

Experimental Approaches

A successful measurement of the reaction $^{15}\text{O}(\alpha, \gamma)^{19}\text{Ne}$, with the aim of determining the stellar reaction rate, must evaluate the pertinent parameters with sufficient accuracy. These parameters are the resonance energy (already known[58]) and the resonance strength, $\omega\gamma$, for each of the important levels in ^{19}Ne, or alternatively the cross section. This chapter describes different methods of determining these parameters and discusses current results, where applicable.

2.1 The Direct Reaction: $^{15}\text{O} + \alpha \rightarrow {}^{19}\text{Ne} + \gamma$

The most obvious method of determining the reaction rate is to measure the reaction cross section directly. Unsurprisingly, however, the most obvious method is experimentally extremely difficult.

Due to the short half-life of ^{15}O (122s), a direct measurement must use an

^{15}O beam on a helium target. This immediately leads to the problems inherent in using a radioactive beam: low intensity, poor beam quality, and high background from the β-decay of the beam particles.

In addition, using helium as a target requires either a gas target, or a helium implanted foil. A gas target requires a window, which results in beam degradation and acts as a source of background which needs to be accounted for. Windowless gas targets exist but provide only small target thicknesses and require complicated systems to maintain the flow of gas. Implanted targets have smaller thicknesses than gas targets. Also, sufficient knowledge of the background events from other materials in the foil is necessary. A discussion on solid and gas targets is given by Rolfs and Barnes[60], though the emphasis is on stable rather than radioactive beams.

However, the most difficult aspect of this measurement is the expected low cross section. This is due to the states of astrophysical interest lying near or below the Coulomb barrier of the compound system, with the resultant reduction in barrier penetrability.

Despite these difficulties, a direct measurement is planned at ISAC, TRIUMF, Canada. For a beam intensity of 10^{11} pps (16 pnA) at 0.154 MeV/u, the expected yield is 0.1 per hour[3] for the population of the astrophysically interesting state at 4.033 MeV in ^{19}Ne. Obviously, many weeks of measurement will be required in order to obtain the necessary statistics, and to provide sufficient understanding of the background components.

2.2 Nuclear Systematics and Mirror Nuclei

An alternative approach is to measure the relevant data for the mirror nuclide, ^{19}F, and then translate that information to the ^{19}Ne system. Several measurements have been published based on this approach and these are described and discussed in the following section.

2.2.1 The Mirror Reaction: ^{15}N$(\alpha,\gamma)^{19}$F

This reaction has been measured in the energy range of astrophysical interest by Magnus et al.[61] using a α-particle beam from a Van de Graaff Accelerator at 690 keV. The target was a thick Ti^{15}N foil, and the emitted γ-rays were measured with a 35% Ge(Li) detector. Resonances corresponding to states at 4.550$(\frac{5}{2}^{+})$ and 4.556 MeV$(\frac{3}{2}^{-})$ in ^{19}F were studied. These are the analogue of the states at 4.600 and 4.549 MeV in ^{19}Ne . The γ-yields for the population of these two states were measured and from this the γ-branching ratios were calculated. Then using the assumption that $\Gamma_{\gamma} \gg \Gamma_{\alpha}$, the reduced α-width, θ_{α}^{2}, was determined. Next, by assuming that $\theta_{\alpha}^{2}(^{19}$F $) = \theta_{\alpha}^{2}(^{19}$Ne $)$, Γ_{α} for the state in ^{19}Ne was calculated from

$$\Gamma_{\alpha} = \theta_{\alpha}^{2} E_{R} f_{\alpha} P_{l}(R_{l}, E_{\alpha}) \tag{2.1}$$

where the parameters are described in [61]. This corrects for the different barrier penetrabilities of the two systems. Finally, by assuming $\Gamma_{\gamma}(^{19}$F $) = \Gamma_{\gamma}(^{19}$Ne $)$, the resonance strengths in ^{19}Ne were calculated. While good agreement with the theoretical value determined by Langanke et al.[57], based on extrapolations of nuclear systematics, was obtained for the 4.600 MeV state,

the resonance strength of the 4.549 MeV state was measured to be at least 16 times smaller than the theoretical value.

This measurement has been repeated by Wilmes et al.[62] using a windowless gas target of enriched $^{15}N_2$ gas (99%) and an α-particle beam from a Dynamitron accelerator. A 100% high-purity germanium (HPGe) detector was used to measure the γ-rays, and elastically scattered α-particles were detected in surface barrier detectors for normalisation purposes. The aim was to improve the measurement of the 4.556 MeV state in ^{19}F for which Magnus only gave an upper limit. By using the resonance strength calculated by Magnus for the the 4.550 MeV state, the resonance strength for the 4.556 MeV state was determined. This value agreed well with the upper limit given by Magnus. Again using the assumption that $\theta_\alpha^2(^{19}F) = \theta_\alpha^2(^{19}Ne)$, $\omega\gamma$ for the 4.549 MeV state in ^{19}Ne was calculated.

However, the lowest lying level of interest at 4.033 MeV in ^{19}Ne corresponds to a state in ^{19}F (3.908 MeV) which is below the α-threshold and thus not accessible via the $^{15}N(\alpha,\gamma)^{19}F$ reaction.

2.2.2 Alpha transfer to mirror nucleus: $^{15}N(^6Li,d)^{19}F$

To overcome the problem that the ^{19}F analogue state lies below the α-threshold, Mao et al.[63] used the transfer of an α-particle from ^6Li to ^{15}N to populate this state in ^{19}F. Mao et al. used a 22 MeV $^6Li^{3+}$ beam from a Tandem Accelerator impinging on a nitrogen gas target, isotopically enriched in ^{15}N (99.5%). The outgoing deuteron tags were momentum analysed in a

multiangle spectrograph, before being detected on nuclear emulsion plates. The reaction ^{16}O(^{6}Li,d)^{20}Ne was also performed for normalisation purposes. The 1^{-} state at 5.788 MeV in ^{20}Ne has a known α width and the α transfer cross section was calculated. Then

$$\sigma_{exp}(20) = N\,S_{\alpha}(20)\sigma_{DW}(20) \tag{2.2}$$

for the ^{16}O(^{6}Li,d)^{20}Ne(1^{-}) reaction, and

$$\sigma_{exp}(19) = \frac{2}{3}N\,S_{\alpha}(19)\sigma_{DW}(19) \tag{2.3}$$

for the ^{15}N(^{6}Li,d)^{19}F($\frac{3}{2}^{-}$), where S_{α} is the α spectroscopic factor, N is a constant related to the structure of the incident particle, and σ_{DW} is the cross section calculated using the code DWUCK4[64]. Then, using the relationships

$$S_{\alpha}(19) = \Gamma_{\alpha}(19)/\Gamma_{sp}(19) \tag{2.4}$$

and

$$S_{\alpha}(20) = \Gamma_{\alpha}(20)/\Gamma_{sp}(20) \tag{2.5}$$

where 19 represents ^{19}Ne and 20 represents ^{20}Ne, and equating equations 2.2 and 2.3 gives the α-width for the state of interest as

$$\Gamma_{\alpha}(19) = \frac{3}{2}\Gamma_{\alpha}(20)\frac{\Gamma_{sp}(19)}{\Gamma_{sp}(20)}\frac{\sigma_{exp}(19)}{\sigma_{exp}(20)}\frac{\sigma_{DW}(20)}{\sigma_{DW}(19)} \tag{2.6}$$

The single-particle width, $\Gamma_{SP}(19)$, of the 4.033 MeV state in ^{19}Ne was calculated from the code **ABACUS**, by approximating the α-nucleus potential to a real Woods-Saxon well, and it was assumed that the α-particle spectroscopic factors are the same for mirror states. The results are model dependent and highly sensitive to, in particular, the radius of the α-particle potential well. The rate calculated in this way was between 22% and 53% higher than the previously accepted value.

2.2.3 Validity of Mirror Nuclide Approach

However, a recent paper by de Oliveira et al.[65] gives a comparison of results using mirror nucleus information with data obtained from the study of the α-decay of ^{19}Ne excited states[56]. This comparison showed a disagreement between the θ_α^2 values which exceeded one order of magnitude. In particular, the assumption that the reduced alpha widths are equal was called into question. Although this assumption is widely used, it is one that becomes less and less valid as the alpha structure of the states is reduced, and for the states below the Coulomb barrier, the alpha strength is weak. Additionally, de Oliveira questions the validity of equating the γ width for analogue levels. Consequently, de Oliviera states that a determination of the ^{15}O$(\alpha, \gamma)^{19}$Ne reaction rate, particularly for states below the Coulomb barrier, which relies on α-transfer data on ^{15}N, must be uncertain by one order of magnitude. Therefore, to obtain better precision in the determination of the ^{15}O$(\alpha, \gamma)^{19}$Ne rate, methods which do not depend on mirror nucleus argumentation and its inherent uncertainty must be employed.

2.3 Indirect Methods

An approach which has already proven successful to some extent is to populate excited states in ^{19}Ne via another initial channel and then measure the decay of these states into the $\alpha+^{15}$O channel. As stated previously, the reaction rate for a given resonance can be calculated if the energy and the strength are known. The resonance energies are known[59] and the strength is given

by

$$\omega\gamma = \frac{2J + 1}{(2J_1 + 1)(2J_2 + 1)}\frac{\Gamma_\alpha . \Gamma_\gamma}{\Gamma_T} \tag{2.7}$$

for a resonance which decays only by α or γ. However, rearranging the formula for γ gives

$$\Rightarrow \gamma = \Gamma_\alpha(1 - B_\alpha) \tag{2.8}$$

or

$$\gamma = \Gamma_\gamma . B_\alpha \tag{2.9}$$

In other words, for such a resonance the main unknown in the reaction rate is the partial alpha width. Consequently, a measurement of the α-branching ratio, B_α, with some knowledge of the total width, is sufficient to put limits on the $^{15}O(\alpha, \gamma)^{19}Ne$ reaction rate.

2.3.1 The $^{19}F(^3He, t)^{19}Ne^*$ reaction

The approach described in the above section has already been used with considerable success by Magnus et al.[56]. Excited states in ^{19}Ne were populated by impinging a ^3He beam (25 pnA) on a CaF_2 target. The triton ejectiles were identified using a QDDD magnetic spectrometer with a ΔE-E detector in the focal plane, allowing the populated state to be determined. α-particles from the decay to ^{15}O were detected using three silicon surface barrier detectors. Identification of the populated states was very good with little background, but due to the small solid angle for the detection of the decay α's, coincidence statistics were poor. Branching ratios were determined for the states at $4.379(7/2^+)$, $4.549(3/2^-)$, $4.600(5/2^+)$, $4.712(5/2^-)$ and 5.092 MeV$(5/2^+)$, and resonance strengths calculated using Γ_γ determined from analogue states

in ^{19}F. However, while important information was obtained on these states, no new data on the state at 4.033 MeV was available.

Improved measurements using this method are currently being undertaken, both in the USA[66] and Japan[67], to attempt to measure the lowest astrophysically interesting state at 4.033 MeV.

2.3.2 The d(^{18}Ne,^{19}Ne*)p reaction

The advent of post-accelerated radioactive ion beams has opened up new methods of producing ^{19}Ne*. The reaction d(^{18}Ne,^{19}Ne*)p is one such method. Since this reaction is only a single neutron transfer, the cross section for populating ^{19}Ne* should be qualitatively higher than that of, for example, the charge exchange reaction described in the previous section. The use of a heavy projectile on a light target, i.e. inverse kinematics, results in the ejectile, ^{19}Ne*, being forwardly focussed and thus the decay products also being emitted in a narrow forward cone. This reduces the solid angle necessary to detect a large percentage of the decay products. Additionally, the recoiling proton gives a tag of the state populated, allowing the branching ratios to be determined.

2.4 Summary

A number of good measurements have already been completed making use of mirror nuclei and nuclear systematics. However, any improved experiments would suffer from the same ambiguities arising from the possible invalidity

of the basic assumptions, particularly for states under the $\alpha + {}^{15}O$ Coulomb barrier. The results rely on nuclear physics input and consequently are highly model dependent.

Furthermore, despite the success of Magnus et al.'s measurement, for the determination of small B_α's, the need for, firstly, very large solid angle detectors to measure the small number of decay α's, and secondly, the very low energy with which the decay α's are emitted, together with the lower cross section of population, was deemed prohibitive with the available systems. So, after consideration of all the approaches discussed in this chapter, and in view of the available facilities, it was decided to attempt this measurement utilising the $d({}^{18}Ne, {}^{19}Ne^*)p$ reaction mechanism. The technique of determining $\omega\gamma$ by $d({}^{18}Ne, {}^{19}Ne^*)$ is almost model independent, relying only on Γ_γ from analogue states.

Additionally, the chosen method results in other nuclear physics output. For example, the elastic scattering of ${}^{18}Ne$ data would allow optical model fits and DWBA calculations to be made at these low energies. Data on the elastic scattering of ${}^{18}Ne$ is currently only available at much higher energies[68]. Also, comparisons with mirror nuclei systems could be made, testing the validity and applicability of the basic assumptions. Finally, the method of using (d,p) reactions in inverse kinematics at low energies with radioactive ion beams to populate states of astrophysical interest for other systems can be tested.

Chapter 3

Experimental Method

3.1 Experimental Design

When designing an experimental set-up, many features must be taken into account to ensure the best use of the available facilities is made. This section gives details of the main aspects of these experiments that had to be considered during the design stage.

Firstly, the experimental aims and conditions that any set-up to be used must fulfill had to be identified. The aim of the measurement was to determine α-branching ratios for excited states in ^{19}Ne in the region of the α-threshold. In order to determine this, it is necessary to know, firstly the number of ^{19}Ne nuclei produced in a particular excited state, and secondly how many of those decayed into the $\alpha+^{15}$O channel. To satisfy the first requirement, the set-up must be able to distinguish protons from other particles and relate unambiguously a particular proton energy to a particular excited

state. For the second requirement, discrimination between protons, alphas and heavy ions is necessary. Additionally, a high detection efficiency for α-^{15}O pairs is needed, i.e. large solid-angle. Other requirements were high granularity and good angular resolution to allow reconstruction of particle trajectories and background reduction.

The position of the detectors was crucial to the success of the experiment. The two factors which had the most bearing on this were:

1. measurement of the tagging protons such that different states in ^{19}Ne could be clearly identified

2. as large as possible coverage of the decay products' phase space

The Monte Carlo code UNIMONTE[69] was used to simulate the energy and angular distributions of the outgoing particles. UNIMONTE takes into account energy losses in the target and energy loss straggling, and is coded so that a known angular distribution can be applied to the outgoing particles.

Initially, the results of a previous measurement by Gul et al.[70] of a similar system were used to predict the angular distribution of the recoiling protons. This paper, on the reaction ^{18}O(d,n), presented angular distributions of the ejected neutrons corresponding to different populated states in ^{19}F. Assuming that for analogue states in ^{19}Ne, the centre of mass angular distribution would be similar, these results were translated to the d(^{18}Ne,^{19}Ne)p system. This distribution for the ^{19}Ne was used in UNIMONTE to produce the expected proton angular distribution in the laboratory. Due to the in-

verse kinematics, in the laboratory frame the ejected ^{19}Ne are very forwardly focussed, with a limiting angle of 6.3 deg for the 4.033 MeV state. Consequently, the application of this angular distribution has little effect on the distribution of either the ^{19}Ne or the decay products.

The proton angular distribution is peaked at around 70 deg. However, at these angles the protons have high energy (10-20 MeV) and the steep variation of energy with angle indicates that discrimination of different states in ^{19}Ne would be difficult. This can be seen in figure 3.1. Consequently, since the available detectors were only capable of stopping protons with energies up to 7 MeV, and these protons are emitted in the backward hemisphere where the kinematics are rather shallow, allowing the discrimination of ^{19}Ne excited states, it was decided to position the proton detector upstream from the target.

UNIMONTE also demonstrated that the ^{15}O particles emerge from the target at angles between 0 and 10 degrees. The α-particles are emitted between 0 and 20 degrees. Therefore two detectors were placed downstream to cover the angular ranges from 4 to 30 degrees. The use of LEDA detectors (see section 3.3) allowed these angular ranges to be covered while utilising the cylindrical symmetry of the system to optimise available statistics. Moreover, the high segmentation allowed these high multiplicity events to be measured with good efficiency, and the count rate per detector element of background events reduced. Previous measurements using the LEDA detector[71] had demonstrated that the energy and timing resolution obtained would be suf-
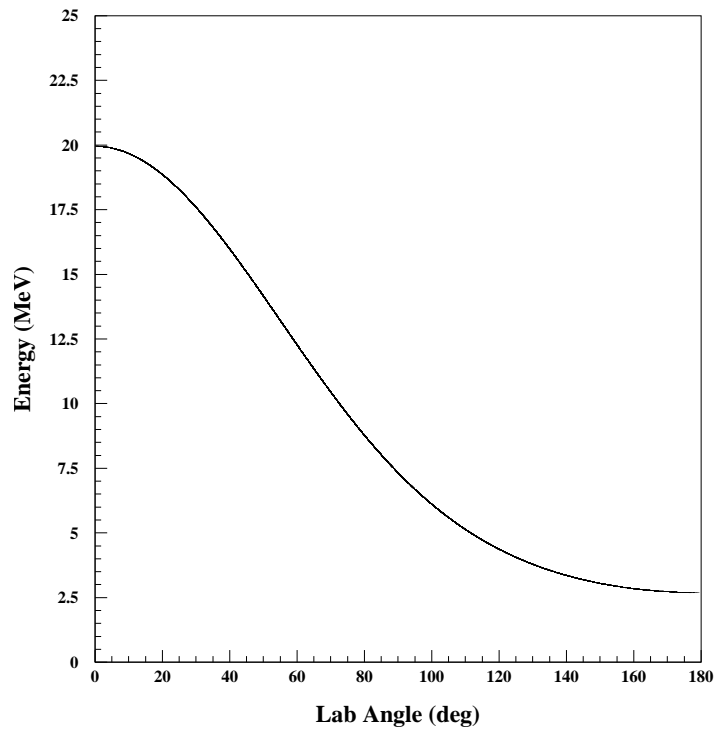
Figure 3.1: *UNIMONTE simulation of proton kinematics for 4.033 MeV state at E = 44 MeV (target effects have been removed for clarity).*

ficient for the requirements mentioned above. Two runs of the experiment were carried out under slightly different conditions. In the first experiment (runI), the beam energy was chosen to give the same centre of mass energy as in the Gul et al. paper so that a comparison could be made. In the second experiment (runII), the beam energy was increased and the proton detector moved closer to the target.
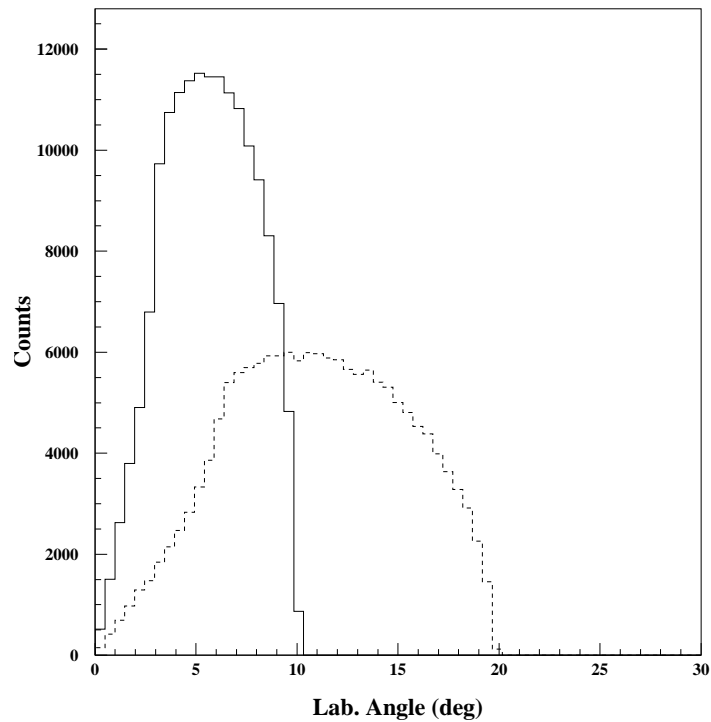
Figure 3.2: *UNIMONTE simulation of angular range of decay products for 4.033 MeV state at E = 44 MeV. Solid line denotes ^{15}O range and dashed line denotes α-particle range.*

3.2 Radioactive Nuclear Beams at Louvain-la-Neuve

The experiments were carried out at the radioactive nuclear beam facility in Louvain-la-Neuve, Belgium. The radioactive species are produced via an ISOL (Isotope Separation On Line) method, using two coupled cyclotrons [72, 73](see fig. 3.3).
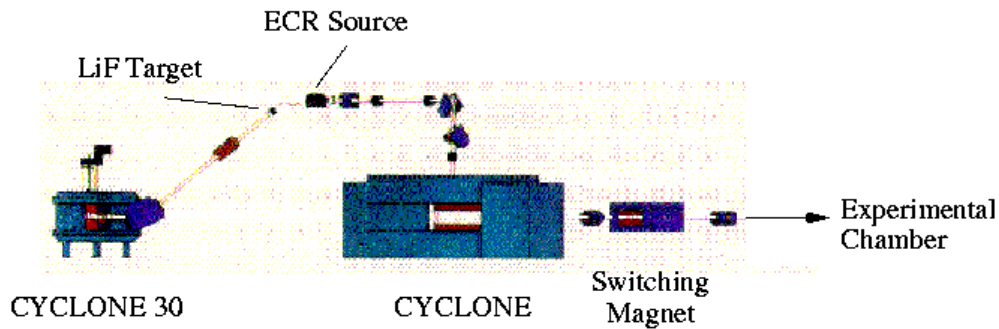
Figure 3.3: *Schematic of radioactive nuclear beam production.*

The first cyclotron, CYCLONE 30, accelerates H^- to 30 MeV. After stripping, these are incident on a production target containing LiF. A (p,2n) reaction on the fluorine component produces ^{18}Ne. The reaction products are then injected into an Electron Cyclotron Resonance (ECR) source[74] where they are ionised. They proceed via a 90 degree analysing magnet to a second cyclotron, CYCLONE, with K=110. The ^{18}Ne are then extracted at the correct energy and sent via a selection magnet into the experimental area. At the energy used in these experiments, the ^{18}Ne was in charge state 3+. The intensity was of the order of 10^5-10^6 pps. The emittance of the beam was 30πmm mrad. The energy resolution is about 0.5 percent, with the beam energy being accurate to a few percent[75].

The beam particles have a half-life of 1.7 s and the transport time from production target to experimental area is of the order of ms. The beam contains about 1 percent contamination from ^{12}C. This was determined from a comparison of the elastic scattering yields on gold(see fig. 3.4).
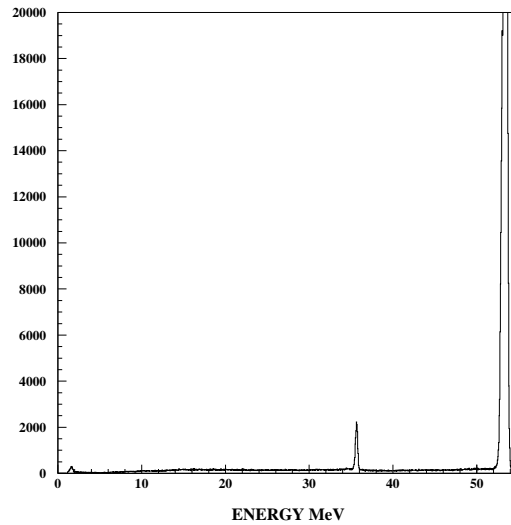
Figure 3.4: ^{12}C *contamination in the* ^{18}Ne *beam: Peak at 53 MeV is elastic scattering of* ^{18}Ne *on gold and smaller peak at 35 MeV is elastic scattering of* ^{12}C *on gold.*

3.3 Detector Set-up

The workings of all silicon detectors rely on the formation of a semiconductor junction[76]. The simple example considered here is that of a pn junction. Such a configuration can be produced, for example, by diffusing sufficient amounts of p-type impurities into one side of an n-type semiconductor. Consider such an interface between p and n-type semiconductors. The p-type has a large number of holes compared to the n-type, and the n-type has a large number of electrons compared to the p-type. Consequently, the holes begin to diffuse into the n-type capturing electrons, while electrons diffuse into the p-type annihilating with the holes. This, however, causes a build-up of charge on either side of the junction. Electrons moving into the p-type

produce a negative charge, leaving behind a positive charge in the n-type. This electric field gradient inhibits further diffusion across the junction and the region is thus empty of mobile charges. This region is called the depletion zone, and any electron-hole pairs created here will be carried out by the electric field. Consequently, it is this region which constitutes the basic part of a silicon detector. Ionising radiation impinging on the depletion zone produces electron-hole pairs, thereby losing an equivalent amount of energy. With electrical contacts on either side of the junction, the electrons and holes carried out by the electric field constitute a signal which can be detected.

Although the junction as described above will work in a detector, the situation can be improved by applying a reverse bias voltage across the junction. The application of a negative voltage on the p-side or a positive voltage on the n-side has the effect of attracting electrons from the n-side making it more positive, and pushing electrons onto the p-side making it more negative. This increases the size of the depletion zone, and consequently the size of the region sensitive to impinging radiation. In addition, the higher voltage increases the charge collection efficiency. The voltage cannot be increased without restriction, however, and is limited by the resistance of the semiconductor. Too high a voltage will cause the junction to breakdown and start conducting.

Ideally, a reversed biased junction will be nonconducting. In reality, however, a small current does flow when voltage is applied. This 'leakage' current has several sources. One is the flow of minority carriers. In other words, holes in the n-type which are attracted to the negative voltage on the p-type, and electrons in the p-type which are attracted by the positive

voltage on the n-side. Another source is thermally generated electron-hole pairs arising from unwanted impurity atoms (not to be confused with the doped impurities).
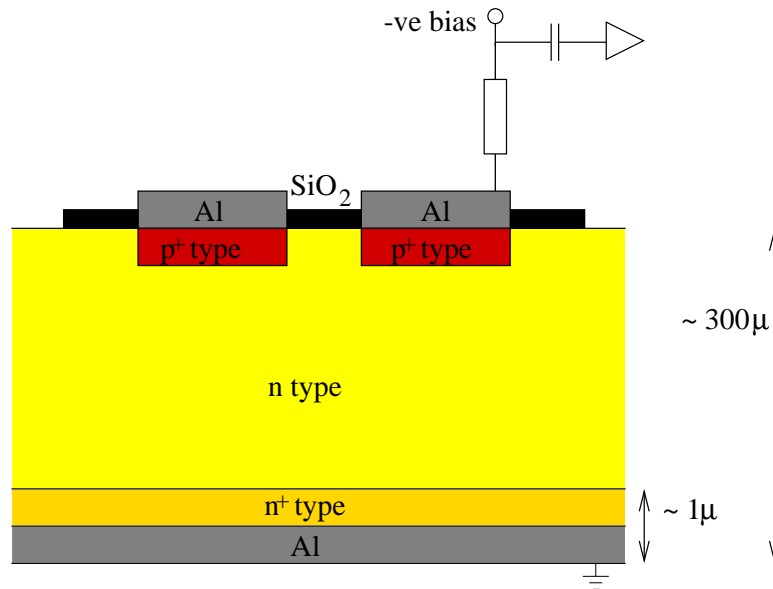
Figure 3.5: *Schematic structure of LEDA detector (not to scale).*

The detectors used during the experiments were LEDA detectors developed in conjunction with Micron Semiconductor Ltd[77, 78]. The LEDA array is a silicon strip detector fabricated using an ion-implantation method. The bulk of the detector is n-type silicon, as seen in figure 3.5. Strips of p^+-type silicon (boron doped) are implanted on the front of the detector. Aluminium contacts are added on top of each strip, and isolated by an inter-strip region of SiO_2. The rear of the detector has n^+-type silicon (arsenic doped) implanted in one complete layer, which is also covered with an aluminium contact.

LEDA is an annular detector, consisting of 8 sectors, each of which have 16 annular strips, giving a total of 128 separate detector elements. The inner diameter of the active area of the detector is 10 cm and the outer 26 cm. The strips are 4.9 mm in width, the inter-strip region being 100 μm. The 3 outermost strips have a reduced phi coverage of 18°, 28°, and 35° as compared to 40° for the remaining 13 strips. This gives a total active area of 361 mm^2. The detectors are approximately 300 μm thick. The p$^+$ implantation is 0.1 μm deep and the aluminium contact is 0.3 μm deep. The quoted depletion voltages are typically 30 V. However, the detectors are operated at up to 70 V to ensure full charge collection is achieved quickly. Leakage currents are typically < 1 μA at room temperature. Table 3.1 lists the characteristics of one LEDA sector.

The design of LEDA gives considerable flexibility in how the detector is mounted. The segmentation of the detector allows each sector to be removed and replaced individually should any strips fail. The position of LEDA can be optimised to cover the required phase space of the particles, and thus the angular resolution depends on the distance from the target. The energy resolution for α-particles at 5.486 MeV is of the order of 25 keV FWHM.

The detector setup used consisted of three full LEDA detectors, as shown in figure 3.6. Two LEDA's downstream from the target measured the α and ^{15}O from the decay, while the LEDA upstream measured the tagging proton. LEDA1 covers 4.5^o - 10.º, LEDA2 covers 14.2^o - 31.6^o, and LEDA3 covers 131.3^o - 154.9^o in runI and 120.1^o - 144.6^o in runII. A photograph of

Typical thickness	300 μm
Number of strips	16
Inner diameter	10 cm
Outer diameter	26 cm
Strip width	4.9 mm
Active area	45.9 cm^2
Inter-strip distance	0.1 mm
Thickness of Al contact	0.3 μm
Thickness of p$^+$ layer	0.1 μm
Leakage current	< 1 μA (25°C)

Table 3.1: *Characteristics of one LEDA sector.*
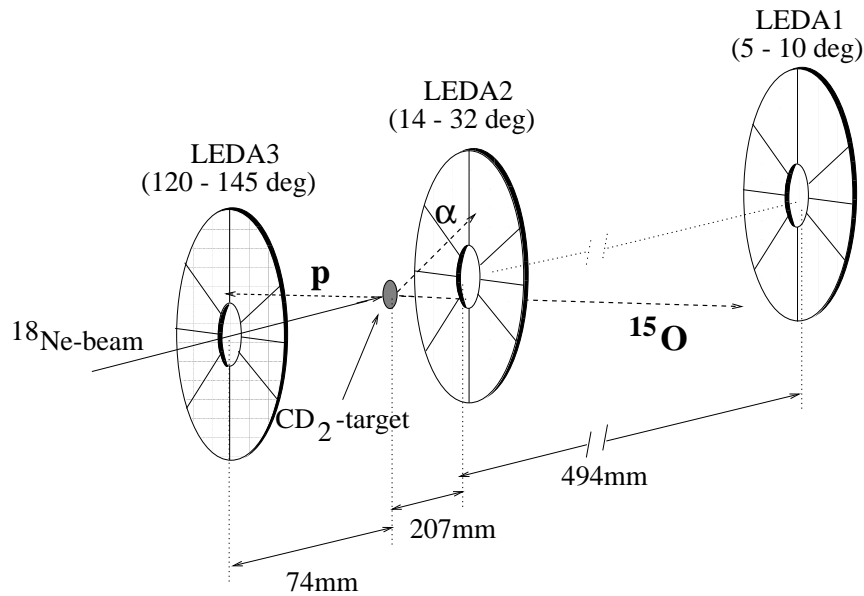
Figure 3.6: *Schematic of LEDA setup used in runII.*
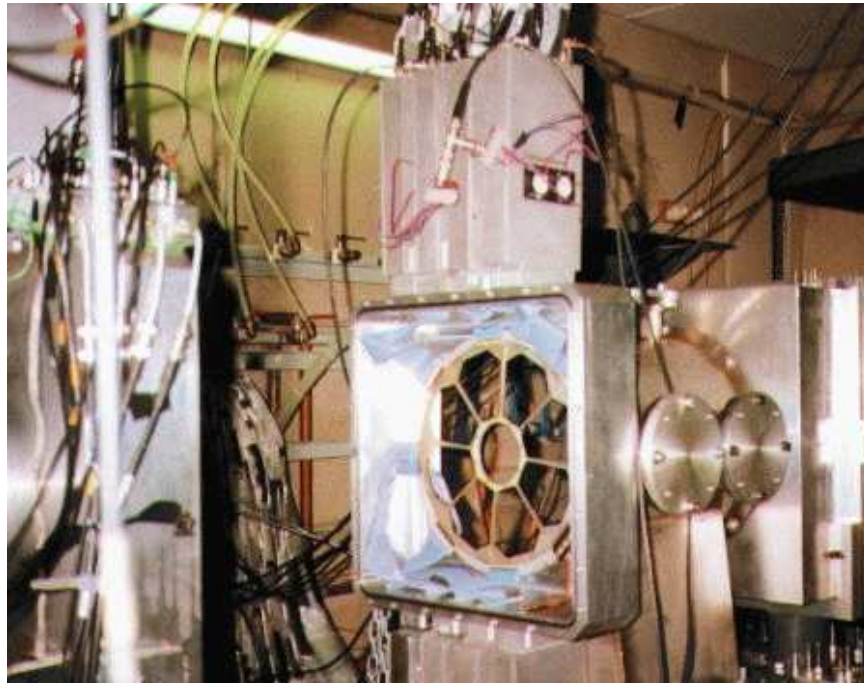
Figure 3.7: *Photograph of experimental chamber with LEDA2 detector.*

one LEDA detector in situ is shown in figure 3.7. Due to the limited electronic channels in the acquisition system, it was necessary for one LEDA to have each pair of strips connected together to halve the number of channels to 64, giving a total of 320 detector elements. This would deteriorate the angular resolution for that detector and so it was decided to double up LEDA1, since the angular straggling and beam emittance already limited the angular resolution of this detector.

3.4   Targets

The main target used during the experiments was 410 μg/cm^2 deuterated polyethylene. The target thickness was chosen such that the count rate was maximised but the energy loss straggling did not inhibit identification of the excited states in ^{19}Ne in the angular range covered by the detectors. This was accomplished by using the UNIMONTE code to simulate the distribution of proton energies after passing through various thicknesses of target material. In addition, four other targets were used to give information on the background present during the experiment. A blank target was used for two purposes. Firstly, this permitted regular checks to be made on possible beam scattering by the target frames. Secondly, a blank target also gave an indication of the background produced by β-particles from the decay of the beam particles (T$_{1/2}$=1.7 s). Elastic scattering on the gold target (carbon with gold) allowed a check of the calculated solid angle values for each detector element. A carbon target was used to determine the fusion background. However, polyethylene better matches the energy loss properties of the CD$_2$ target and was thus also used. In addition, the effect of the proton contamination in the (CD$_2$)$_n$ target could be taken into account by using this target.

The thickness of each target was measured using a triple line α-source (see appendix C). First, a measurement of the α-particle energy was made without a target foil in place, and the positions of the three α-peaks noted. This information together with the results of a pulser walkthrough allowed an energy calibration to be made (see section 4.2). Then the measurement was

Material	thickness ($\mu g/cm^2$)	
	runI	run II
$(CD_2)_n$	410 ± 62	410 ± 62
$(CH_2)_n$	590 ± 90	253 ± 38
carbon	270 ± 40	200 ± 30
gold/carbon	$24/38 \pm 5/8$	$22/20 \pm 4/4$
gold	320 ± 48	-

Table 3.2: *Details of targets used in experiments.*
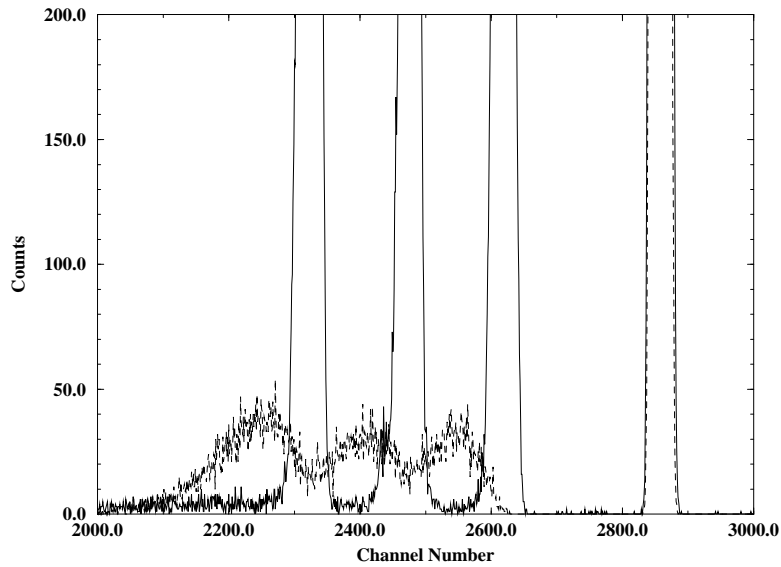
Figure 3.8: *Typical alpha spectrum from foil measurement. Soild line denotes alpha spectrum taken without foil and the dashed line denotes a measurement with a foil. The peak above channel 2800 is due to the pulser. The difference in amplitude for spectra with and without a foil is due to differences in measurement time.*

repeated with each foil in turn mounted between the detector and the source. Figure 3.8 shows such an alpha spectrum, with and without the foil in place. The new position of the peaks allowed the energy loss of the α-particles in the foil to be determined. Once the energy loss was known, the thickness of each target foil was calculated.

3.5 Electronics and Acquisition

Figure 3.9 shows a schematic of the main components of the electronic set-up.
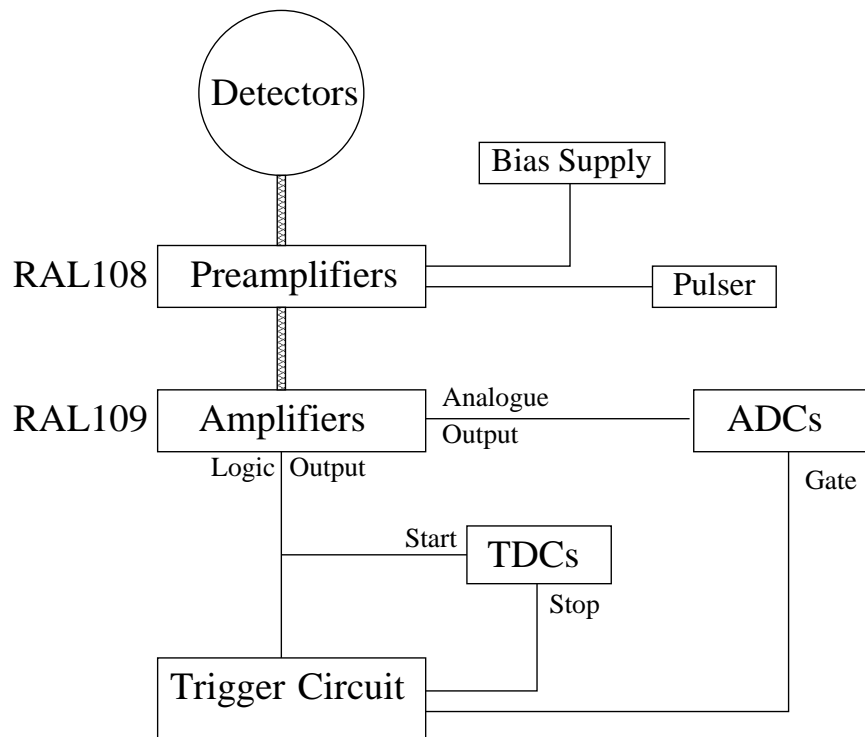
Figure 3.9: *Schematic of instrumentation.*

3.5.1 Preamplifiers and Amplifiers

Each LEDA sector of 16 strips is connected via ribbon cables and a vacuum feedthrough to a box, containing 17 charge sensitive RAL108 preamplifier chips[79], which is mounted on the exterior wall of the chamber. The output from each box is connected to RAL109 shaping amplifier/discriminator cards[79]. Figure 3.10 shows one LEDA sector with a preamplifier box and amplifier card. Each amplifier board handles 8 channels, with two output signals per channel. The analogue output is sent to the Silena 4418/V CAMAC ADCs (Analogue to Digital Converter), and the discriminated logic output is sent, via a trigger circuit, to the ADC gate initiating readout. Each detector element had its own ADC and TDC (Time to Digital Converter). The gain of the amplifiers, and thus full scale range (FSR), is determined by interchangeable resistor packs which plug into each card.
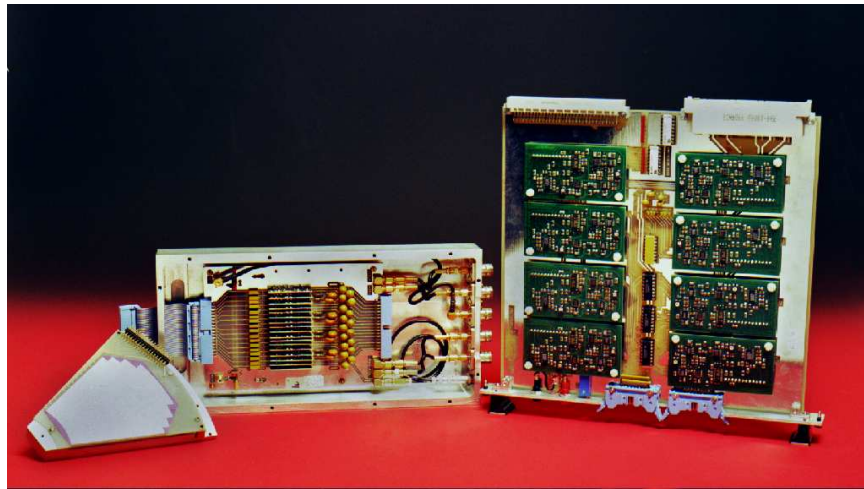
Figure 3.10: *Photograph of LEDA sector with RAL preamplifier box and amplifier card.*

3.5.2 Trigger Circuit

Due to the low beam intensity, and consequent low event rate, the trigger for the acquisition system consisted of a total OR of all detectors AND the signal from the cyclotron frequency (see fig 3.11).
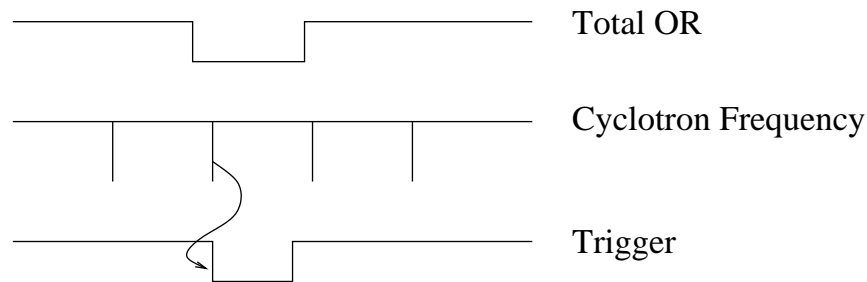
Figure 3.11: *Schematic of trigger.*

The logical outputs from the amplifiers are sent to LeCroy 4564 Logic Modules. The output from these modules corresponding to an OR of all inputs (output 10) was chosen and connected, via ECL-NIM convertors, to logic fan in/fan out (FI/FO) modules. Three FI/FO modules were used, each of which corresponded to the OR of a complete LEDA detector. The outputs of each module were sent separately to the scaler and ratemeter to record the rates in each detector. The scaler allowed the rates to be recorded by the acquisition system and ratemeter allowed the rates to be monitored by eye. The OR of each detector was also sent to another FI/FO to give the total OR of all detectors. This output was also sent to the scaler and ratemeter. The total OR was then shaped (using a Quad timer) before being put in coincidence with the signal from the cyclotron. This coincidence allowed tim-
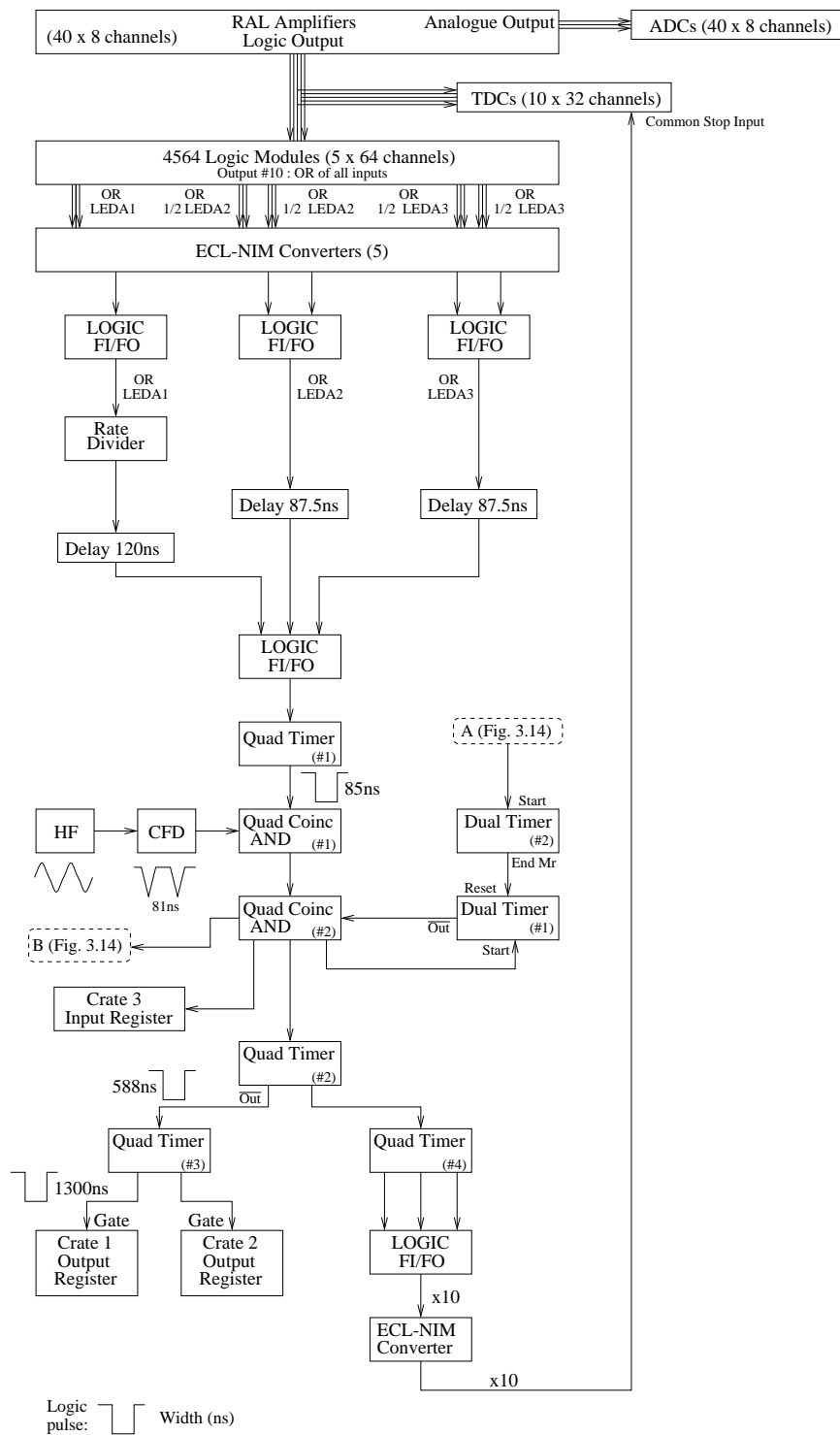
Figure 3.12: *Schematic of electronics from amplifiers to CAMAC crates.*

ing information to be determined. The cyclotron frequency signal was sent through a constant fraction discriminator to output pulses with the same frequency as the cyclotron to be used in the coincidence. This trigger signal was further shaped and then sent as the start of a dual timer. This module opens a 'gate'(sets the output signal negative) which initiates readout of the CAMAC modules. Once all modules have been read, the CAMAC output register sends a signal to the dual timer to reset its output signal to zero, i.e. close the gate. The system is then ready for the next event. Figures 3.12 and 3.13 show schematically the electronic set-up.
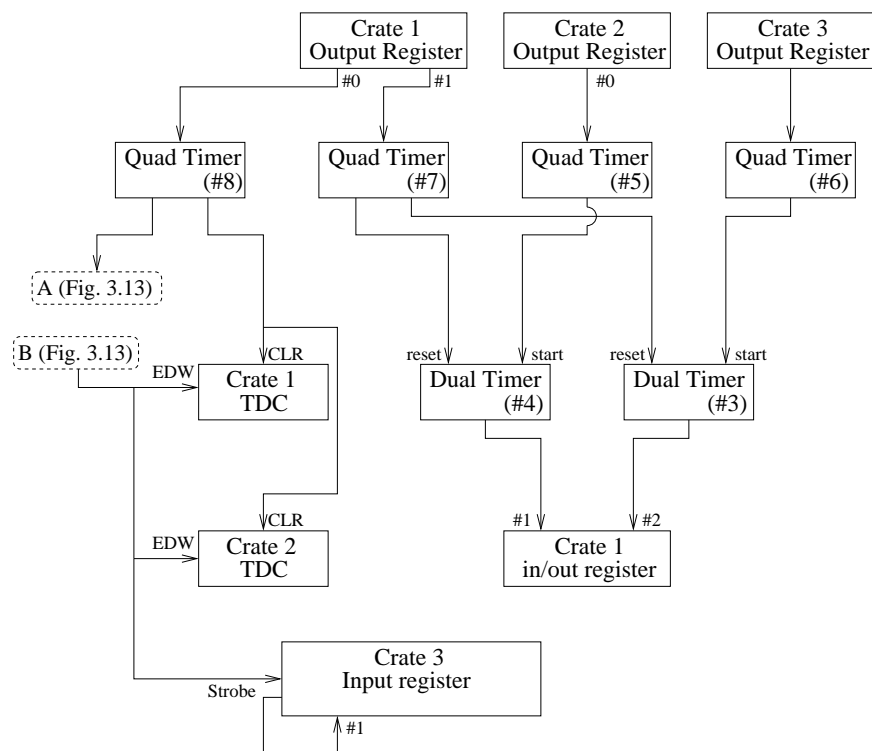
Figure 3.13: *Schematic of CAMAC configuration for three crates which ensures synchronisation of data readout.*

3.5.3 Timing Circuit

Timing information with respect to the cyclotron frequency was obtained using LeCroy 3377 CAMAC TDCs (Time to Digital Converter) in common stop mode. Ten TDCs were used, each having 32 channels. When a signal with enough energy to pass the discriminator arrives at an amplifier, the logic output starts the relevant TDC. The first signal to arrive, which is in coincidence with the cyclotron signal, is processed to provide the stopping signal after delay for all the TDCs (see fig. 3.14). The number of clock cycles between the START and STOP is converted to a digital output. Since the system is in inverse timing mode, the faster the particle the higher the TDC conversion. In other words, TDC conversion is proportional to the particle velocity and inversely proportional to its flight time.
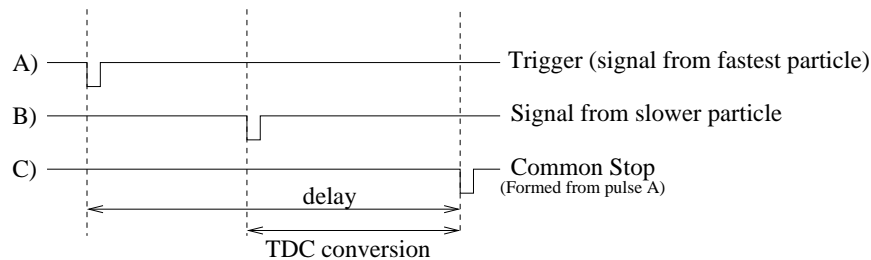
Figure 3.14: *Schematic of timing.*

3.5.4 Acquisition

The acquisition system consisted of three CAMAC crates controlled by VME cards. Crates one and two contained ADCs and crate three contained TDCs. When an ADC or TDC receives a signal while the acquisition gate is open,

they convert the data and send a LAM (Look At Me) to the crate controller. The crate controller initiates readout of these modules and these sub events are buffered. The VME CPU builds events from the data from each of the crate controllers and buffers the events in blocks. Finally, the data blocks are written to tape. In addition, spectra on a PC are incremented and these can be viewed online. The time taken for readout of all the activated modules determines the dead time of the system. The dead time is the percentage of time that the system is busy and thus unable to accept other events. This can be calculated by:

$$\text{dead time} = \frac{\text{total number of triggers - accepted triggers}}{\text{total number of triggers}}$$

The system can handle event rates of up to 5kHz without significant dead time losses.

Chapter 4

Calibration and Data Analysis

This chapter describes the procedures used for calibrating the data, calculating experimental resolutions and determining cross-sections.

4.1   Angle Determination

As LEDA is an annular detector and is mounted perpendicular to the beam axis, for a particular strip, the angle subtended at the target is given by

$$\theta = tan^{-1}(\frac{r}{d}) \tag{4.1}$$

where r is the distance from the centre of LEDA to the middle of the strip and d is the distance from the target. The distances to each detector are given in table 4.1, and the corresponding angles are given in tables B.1-B.3. Figure 4.1 shows this geometry. Table B.4 gives the values of $\Delta\phi$ for each strip. In each LEDA, the sectors are numbered 0-7 and in each sector the outermost strip is numbered 0 and the innermost 15. For LEDA1, as the strips are doubled up, the strips are numbered 0(outermost) to 7(innermost).

Detector	Distance (mm)
LEDA1	703 ± 2
LEDA2	207 ± 2
LEDA3 (run I)	112 ± 2
LEDA3 (runII)	74 ± 2

Table 4.1: *Distance to each LEDA detector.*

Figure 4.2 shows the identification system for each sector and strip.
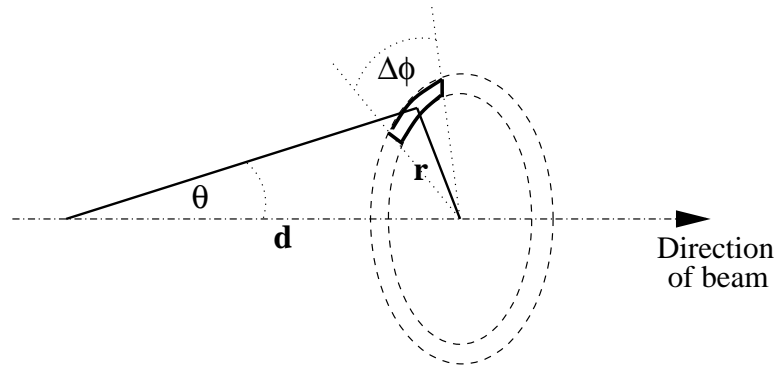
Figure 4.1: *Determination of strip angle.*

Since the LEDA set-up has cylindrical symmetry, the ϕ=0. degree point can be chosen arbitrarily. It was chosen to be in the centre at the top corresponding to the first sector in LEDA1, with increasing ϕ in the clockwise direction when facing downstream. LEDA3 faces downstream rather than upstream and so to agree with LEDA1 and LEDA2 increasing ϕ is anti-clockwise, when facing upstream. The sectors in LEDA3, however, are also numbered in the anti-clockwise direction, and so increasing sector number always corresponds to increasing ϕ. Table B.5 gives the values of ϕ for each

Figure 4.2: *Diagram of sector and strip identification*

sector in each detector.

4.2 Energy Calibration

The response of the electronics was shown to be linear by fitting pulser data with a straight line, as shown in figure 4.3. Consequently, for a given ADC channel, x, the corresponding energy, E, is given by

$$E = mx + c \qquad (4.2)$$

where c is some dc offset in channels and m is the total gain of the system. Both these parameters must be determined for each electronic channel in order to calibrate the data.
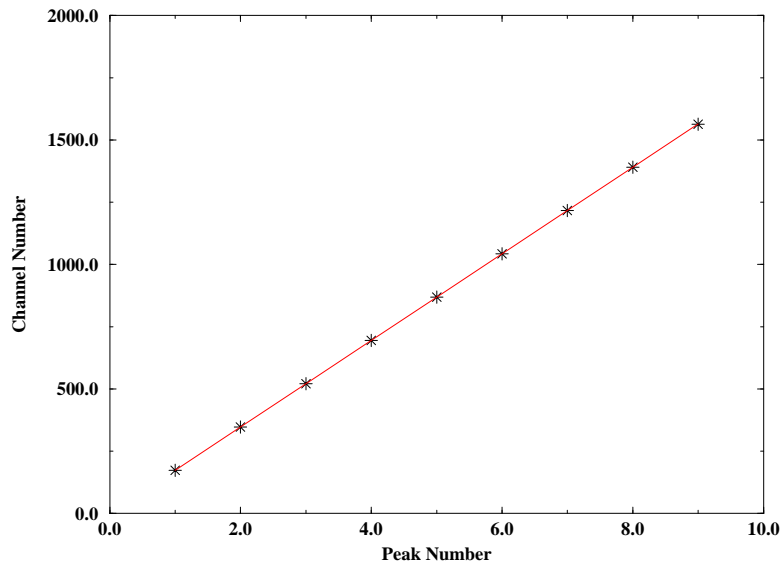
Figure 4.3: *Linear fit to pulser data.*

The dc offset was determined from a pulser walkthrough. The pulser signal was fed into the RAL preamplifiers and thus processed as if it was a detector signal. The pulser was set to output a sequence of voltage signals which were in the ratio 1:2:3:...:9. Then the resulting equally spaced peaks in the energy spectra were used to extrapolate to where the 0.0 V point would be, giving the offset. The linear regression formulae used are taken from [80].

The gain for each electronic channel was determined using the known energies of a triple line α-source, containing ^{239}Pu, ^{241}Am and ^{244}Cm. The details of this source are given in appendix C. The energy measured by the detector is the energy of the incident α-particle minus the energy loss in the dead layer. This energy loss is dependent on both the energy and angle of the incident particle. Alpha particles detected in strips at larger angles, with
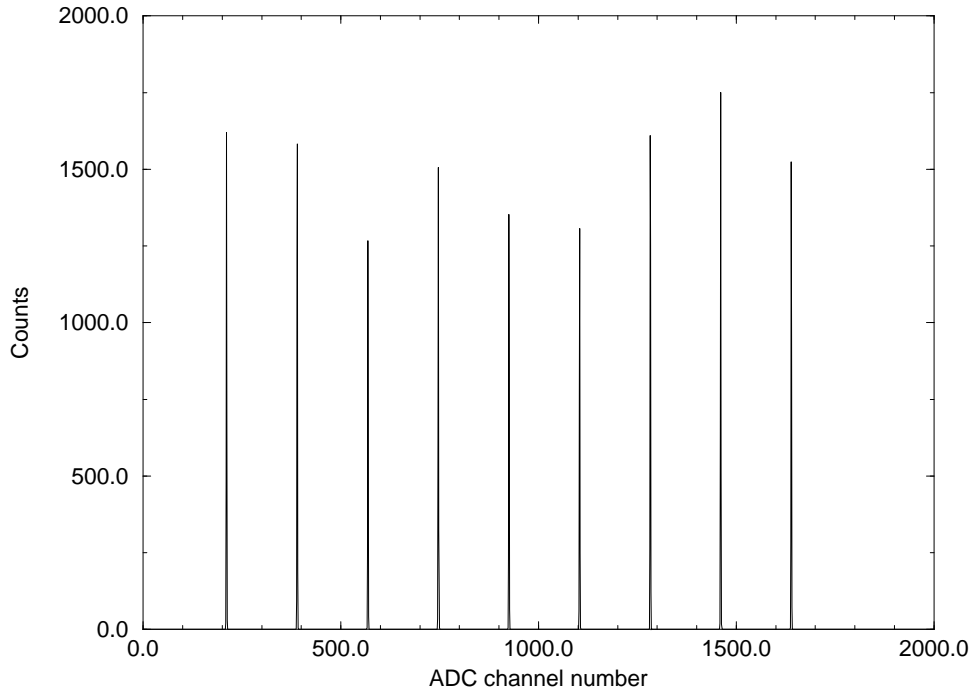
Figure 4.4: *Example of pulser walkthrough spectrum.*

respect to the source, experience a thicker effective dead layer and thus the energy loss is higher. For each angle and α-particle energy, the energy loss in the dead layer was calculated assuming a dead layer thickness of 0.4 μm of Si. The gain for each channel was then calculated from

$$m = \frac{\sum_{i=1}^{n} \frac{Energy(i) - \Delta E(i)}{(channelnumber(i) + offset(i))}}{n} \qquad (4.3)$$

where i is the index for each alpha peak and n is the number of peaks which, in this case, is three. Thus, the calculated gain is the average of the gain for each alpha peak.

To check the alpha calibration, a spectrum of calibrated ADC channel versus detector strip was plotted to show that alpha peaks of the same energy appeared at the same channel number for different strips. Figure 4.5 shows such a spectrum. The increase in α-energy with increasing strip number in a particular detector is an effect of the angle-dependent energy loss.
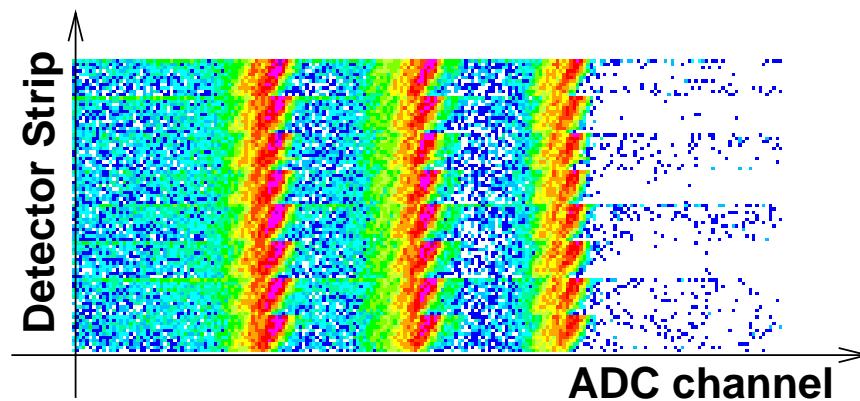
Figure 4.5: *Example of alpha particle energy vs. strip spectrum for all strips in LEDA3.*

Two additional checks on the energy calibration were made using the elastic scattering data. Firstly, it was ensured that for detector strips that corresponded to the same scattering angle, the values of the calibrated ADC channels matched, i.e. the peaks lay on top of one another. Secondly, a plot of angle versus elastic peak energy was plotted to check that the kinematics were as expected. This plot also allowed the initial energy of the incident beam to be determined. A computer program was used which plotted energy versus angle for a given elastic scattering system taking into account the energy loss in both the target and the detector dead layer. The actual data were plotted

on the same graph and the incident beam energy input to the calculation changed until the calculated curve agreed with the experimental data points. Figure 4.6 shows the data points (black stars) for the elastic scattering of ^{18}Ne on ^{12}C from the $(CD_2)_n$ target for runII. The red line shows the calculated kinematics for an initial beam energy of 54.3 MeV. As mentioned in section 4.1, the inital beam energy from the cyclotron is only known to a few percent [75], and thus this method allows a more accurate determination of the beam energy. This procedure was repeated for the data from runI and gave an initial beam energy of 44.1 MeV.

4.3   Timing Calibration

The elastic scattering on gold data was used to calibrate the TDC data for LEDA1 and LEDA2. For LEDA1 the time of flight for ^{18}Ne scattered elastically on gold into the outermost strip was compared to that scattered into the innermost, taking into account the different flight path lengths. The difference in time of flight was calculated to be 0.37 ns. Therefore, since each TDC channel corresponds to 0.5 ns(determined by TDC internal clock), this difference is less than one TDC channel. Consequently, the TDC data for each strip was shifted so that the elastic scattering peaks appear at the same TDC channel number. This procedure was repeated for LEDA2. The time of flight difference between inner and outer strips was calculated to be 1.36 ns. Although this is greater than a single TDC channel, it is still less than the timing resolution (see section 4.5) and so, as with LEDA1, the data were shifted so that the elastic peaks aligned. The average time of flight to LEDA1 for
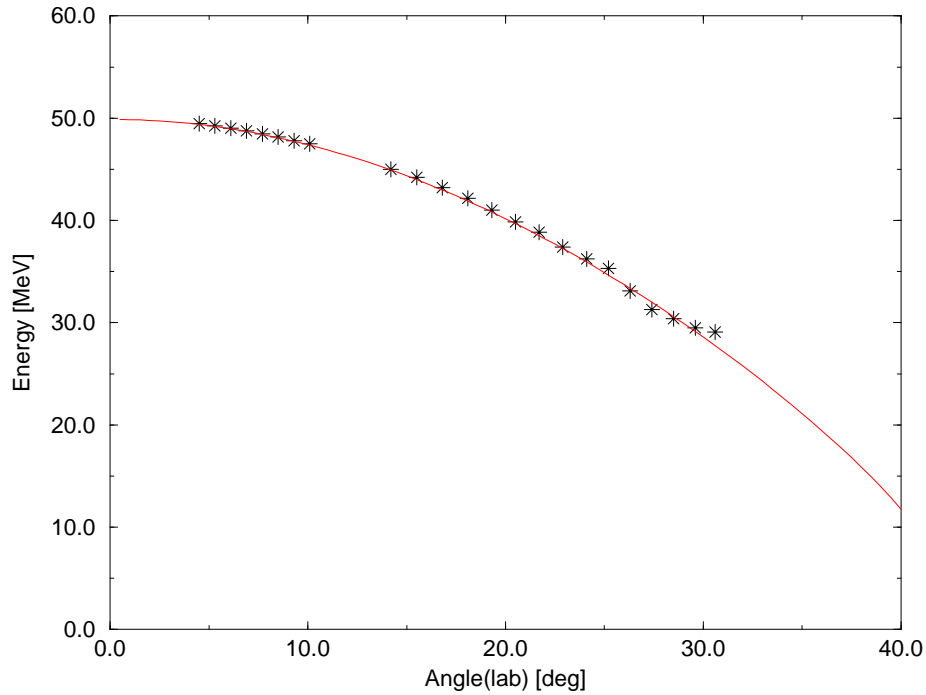
Figure 4.6: *Calculation and data points for the kinematics of the elastic scattering of ^{18}Ne by ^{12}C.*

elastically scattered ^{18}Ne is roughly 20 ns longer than for LEDA2. Therefore, the LEDA2 elastic TDC peaks were aligned to a TDC channel 40 channels lower than LEDA1 to reflect this relative timing. The LEDA3 TDC data were calibrated using the highest lying proton peak in the CD_2 data. As above, these peaks were aligned to the same TDC channel, which was arbitrarily chosen.

4.4 Solid angle determination
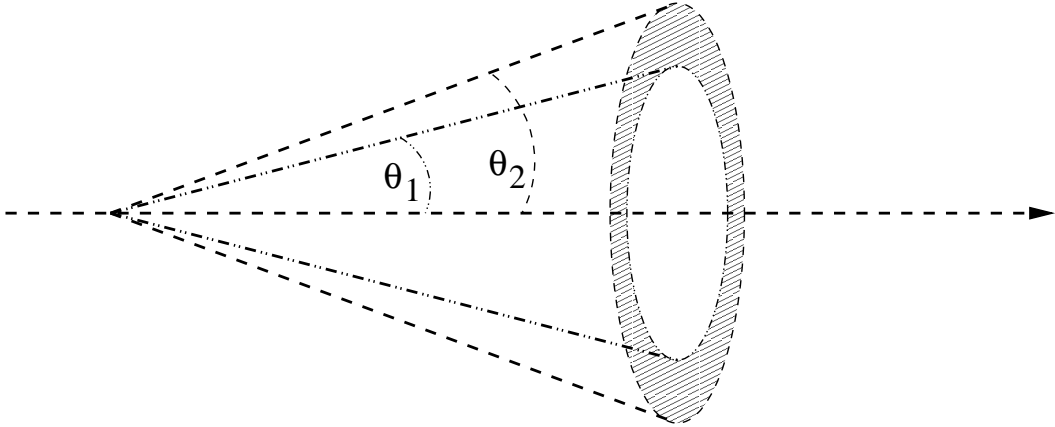
Figure 4.7: *Schematic of solid angle determination.*

As with the angle determination, since LEDA is annular and perpendicular to the beam axis, the solid angle can be calculated from a simple geometrical formula. Each set of strips at a fixed angle can be represented as a ring bounded by two cones, as shown in Figure 4.7. The solid angle of the ring is given by

$$\Omega = \int_0^{2\pi} d\phi \int_{\theta_1}^{\theta_1} sin\theta d\theta \Omega = 2\pi(cos\theta_1 - cos\theta_2) \qquad (4.4)$$

Thus the solid angle for any one of the strips in that ring is

$$\Omega = \int_{\phi_1}^{\phi_2} d\phi \int_{\theta_1}^{\theta_1} sin\theta d\theta \Omega = \Delta\phi(cos\theta_1 - cos\theta_2) \qquad (4.5)$$

Tables B.6-B.8 lists the values of Ω for each ring of eight strips in each detector. These values take into account the dead regions between sectors.

4.5   Energy and Time Resolutions

$$\sigma_T^2 = \sigma_{elec}^2 + \sigma_{det}^2 + \sigma_{beam}^2 + \sigma_{tar}^2 \qquad (4.6)$$

The measured energy and timing resolutions are the result of the convolution of several different factors. These are the electronic resolution, σ_{elec}, the detector resolution, σ_{det} which depends on the particle type, the beam resolution, σ_{beam} and the effects of the target, σ_{tar}. The LEDA detectors have intrinsic energy and timing resolutions as do the subsequent electronics. The electronic resolutions were determined from the pulser data. The detector energy resolution was calculated from the alpha calibration data after accounting for the electronic resolutions using the equation

$$\sigma_{det}^2 = \sigma_{alpha}^2 - \sigma_{elec}^2 \qquad (4.7)$$

This gives detector resolutions for α-particles only. However, proton resolutions are less than those of α-particles under the same conditions since the energy loss and thus energy loss straggling is smaller for protons. Consequently, this value for the detector resolution can be taken as an upper limit. Figure 4.8 shows typical alpha energy resolutions in LEDA3.

Figure 4.9 shows the electronic timing resolution. The upper spectrum shows a pulser walkthrough. The walk in time due to the leading edge discriminator in the amplifier can be clearly seen as a decrease in the TDC channel for low energy signals. The detector timing resolution cannot be obtained from the alpha calibration data since the α-particles are emitted randomly in time.

The properties of the incident beam and the target also affect the measured resolutions. From figure 4.10, measured total resolutions for elastic
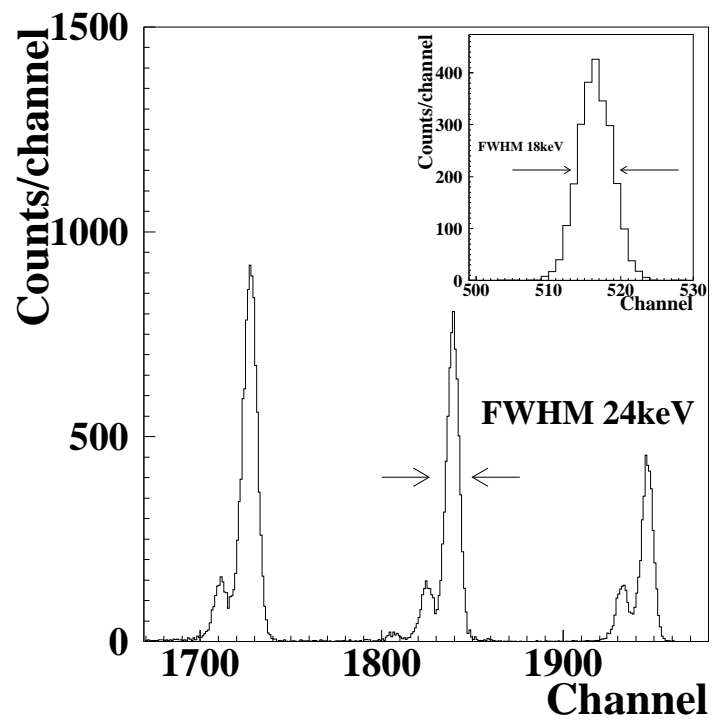
Figure 4.8: *Alpha spectrum with pulser spectrum inset.*
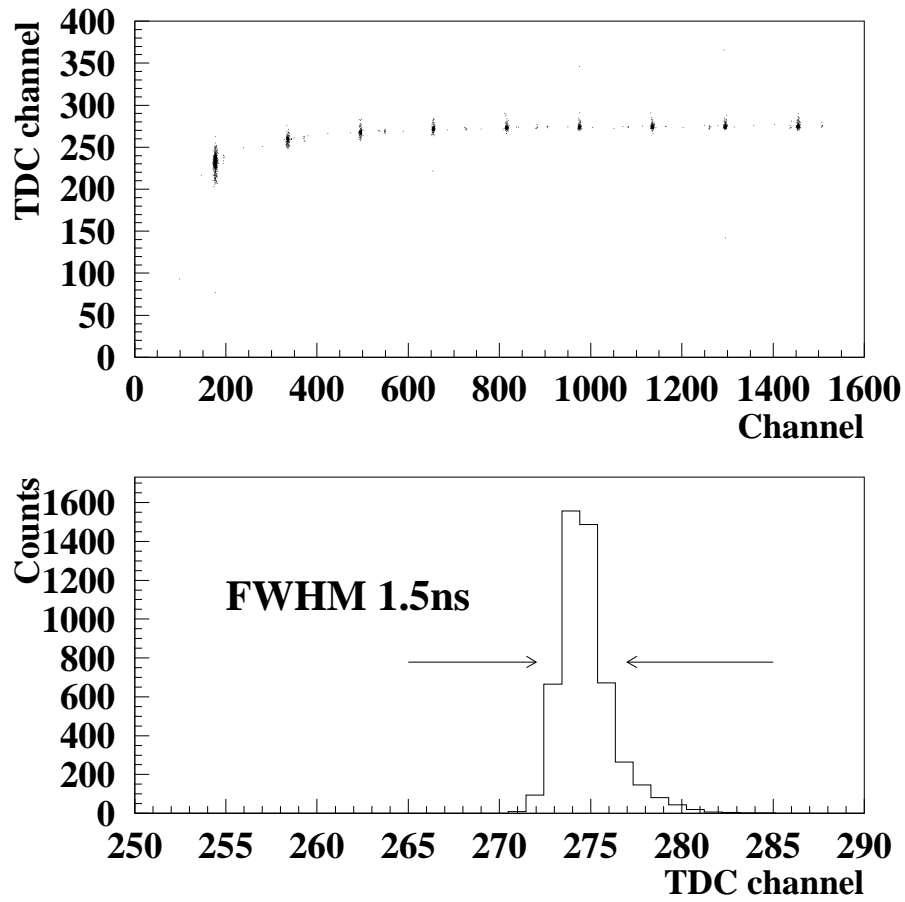
Figure 4.9: *TDC spectrum for pulser.*
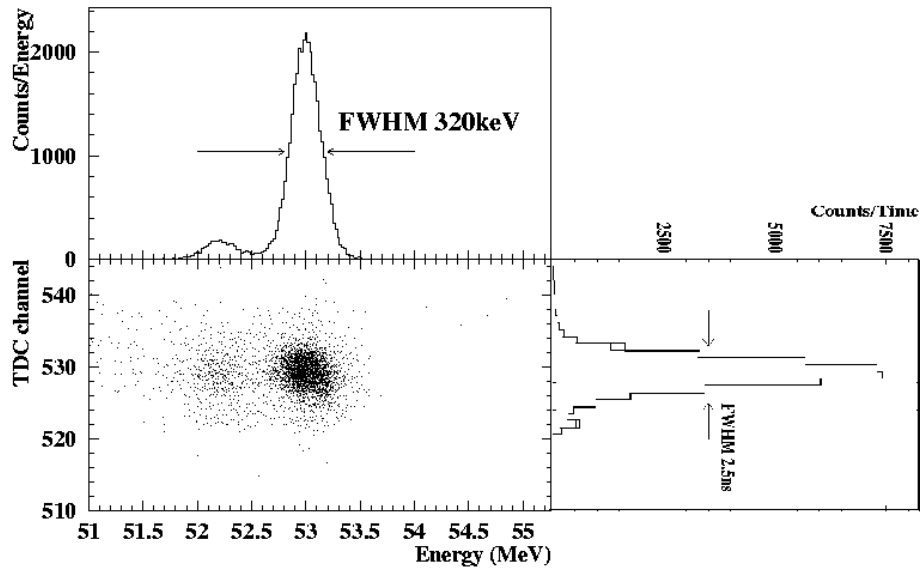
Figure 4.10: *Energy and time resolution for scattering on gold.*

scattering on a gold/carbon target can be seen. An estimate of the energy resolution of the beam could be obtained since this target was thin enough for its contribution to the energy resolution to be neglected. Table 4.2 gives typical energy and time resolution values.

Source	Energy FWHM [keV]	Timing FWHM [ns]
Electronic	18	1.5
Detector	16 (for α)	-
Beam	319	2.0

Table 4.2: *Typical energy and time resolutions*

4.6 Cross-section Determination and Normalisation

The cross-section can be calculated for a given yield from

$$\frac{d\sigma}{d\Omega}(\theta) = \frac{N.M}{N_o \Omega \rho N_A} \qquad (4.8)$$

where N is the yield

M is the atomic mass of the target

Ω is the solid angle for that detector element

ρ is target thickness in g/cm^2

N$_A$ is Avagadro's number

and N$_o$ is a normalisation parameter which accounts for beam intensity, time over which counts were accumulated, and dead time of the acquisition system.

For each angle in LEDA1 and LEDA2, the measured cross-section was calculated as described above for the elastic scattering of ^{18}Ne on ^{197}Au. Then, for the same angles, the Rutherford cross-section in the laboratory frame was calculated, and the ratio between the two cross-sections was plotted for each angle.

For this system, the Coulomb barrier is approximately twice the energy in the centre of mass and so the scattering was assumed to be purely Rutherford. Under this assumption, the normalisation parameter was adjusted until the ratio varied around 1. The ratio values varied around 1.0 because the values for the solid angle were slightly inaccurate, probably due to slight misalignment between the beam and detectors. This was corrected

for by multiplying the solid angle values by the corresponding ratio value. Next the differential cross-sections for ^{18}Ne on ^{12}C were calculated using the data from the CD$_2$ target. The grazing angle θ_g was calculated from [81]

$$\theta_g = 2arcsin(\frac{\epsilon_c}{2\epsilon - \epsilon_c}) \qquad (4.9)$$

where

$$\epsilon_c = \frac{Z_1 Z_2 e^2}{A_{12} R_c}; \quad \epsilon = \frac{E_{lab}}{A_1} \qquad (4.10)$$

Z$_1$ is the projectile charge, Z$_2$ is the target charge, A$_{12}$ is the reduced mass and R$_c$ is the Coulomb radius. For runII, the grazing angle was calculated to be 41° in the centre of mass. This corresponds to a laboratory angle of 16°. Since this angle lies outside the LEDA1 detector, the angular distribution measured by LEDA1 can be approximated to Rutherford. For runI, since the beam energy is lower the grazing angle is higher and so the same approximation can be applied. As before, the normalisation parameter was varied until the LEDA1 distribution was approximately 1. As the deuteron scattering data was obtained simultaneously, the same normalisation parameter could be used.

Chapter 5

Experimental Results

This chapter presents the main experimental results obtained from both experiments. Excitation energy spectra for ^{19}Ne and reaction angular distributions for various populated levels are presented. Excitation energy spectra for triple coincidence events together with the calculated branching ratios are also given.

5.1 Excitation Energy Spectra

Excitation energy spectra were produced from the raw proton energy data measured in LEDA3. Firstly, the data for each strip with the same angle were added together. Then, energy-time spectra were produced for each angle, an example of which is given in figure 5.1. The broad vertical band on the left corresponds to background events from β-particles originating from the radioactive beam. The slightly curved locus extending across the spectrum corresponds to prompt proton events. The three vertical lines correspond to
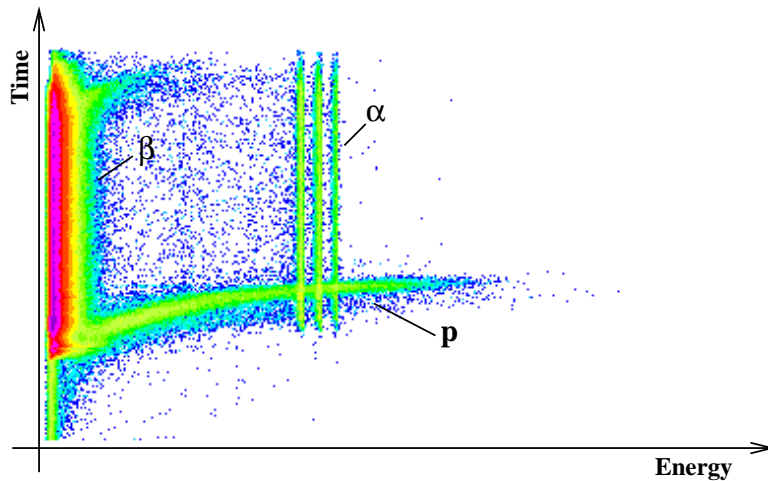
Figure 5.1: *Energy-time spectrum for LEDA3 showing protons, α's and β's (see text).*

α-particles from the calibration source, which have no timing correlation with the beam. The data were resorted with a gate on the prompt proton events. Once an event had been identified as falling into this gate, the energy was corrected for energy loss in the target and detector dead layer, on an event by event basis. Finally, the corrected energy was converted into ^{19}Ne excitation energy and the data from all detector rings summed together. The formulae used to calculate the energy loss and the transformation from proton energy to excitation energy are given in appendix D. The final spectra are shown in figures 5.2 and 5.3. Fits to these spectra were made to determine the yields and these are shown in figures 5.4, 5.5, 5.6 and 5.7. A full discussion of these spectra will be given in section 6.3 together with a discussion on the DWBA calculations.

For the state of astrophysical interest at 4.033 MeV, there is little evidence of its population in $E_{lab} = 44.1$ MeV, though it cannot be excluded. For
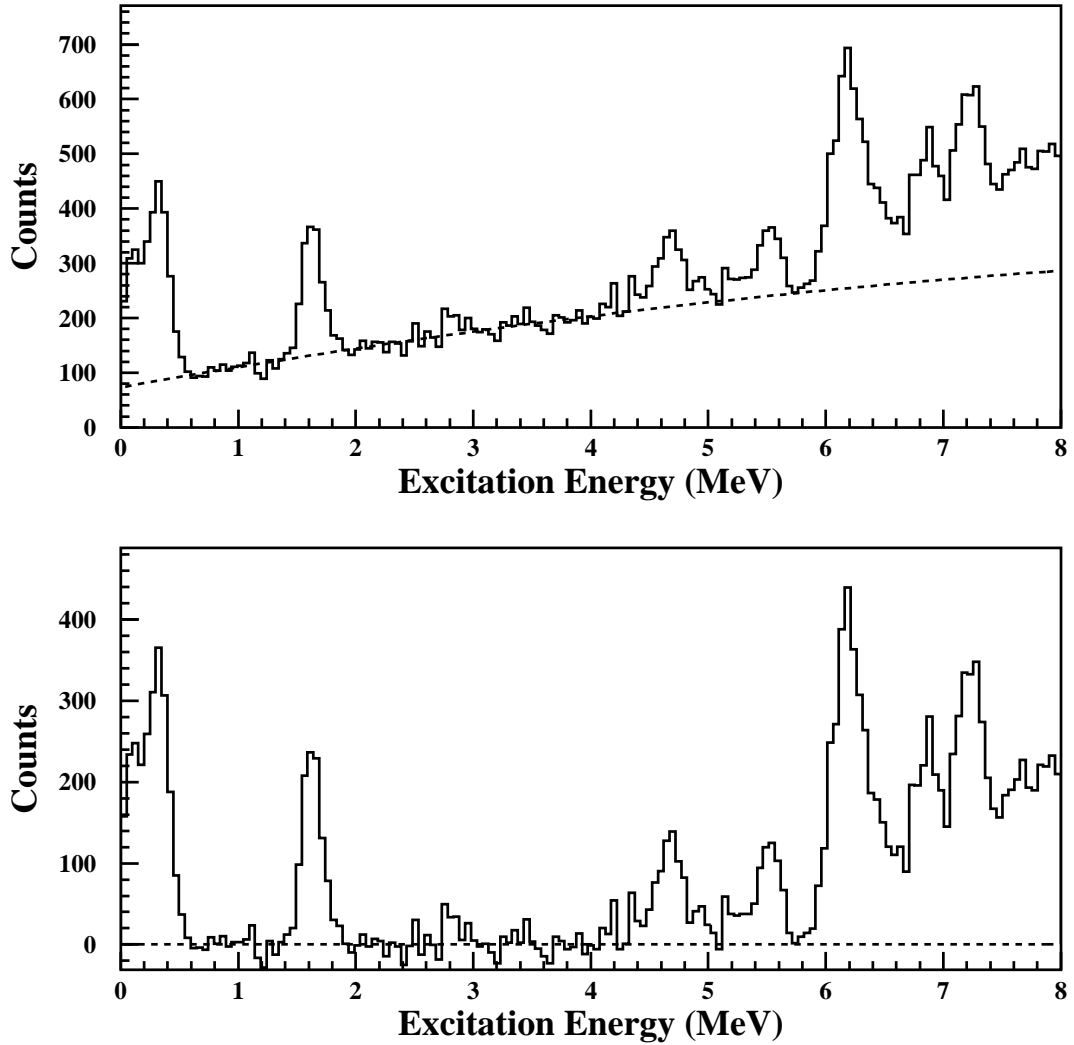
Figure 5.2: *Total excitation energy spectrum for $^{19}Ne^*$, populated via the $d(^{18}Ne,^{19}Ne^*)p$ reaction at $E_{lab} = 44.1$ MeV. Upper panel shows original spectrum and lower panel shows background subtracted spectrum.*
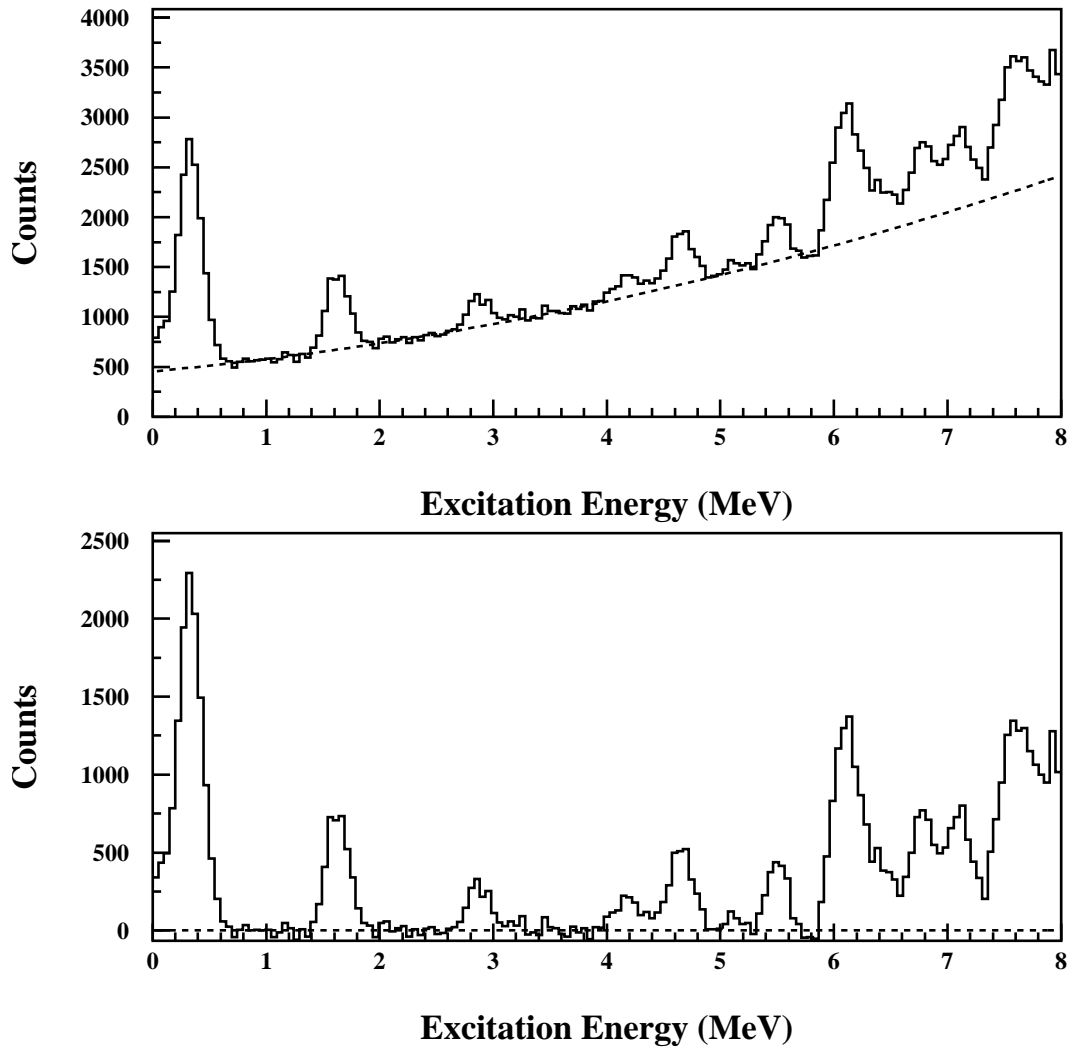
Figure 5.3: *Total excitation energy spectrum for $^{19}Ne^*$, populated via the $d(^{18}Ne,^{19}Ne^*)p$ reaction at $E_{lab} = 54.3$ MeV. Upper panel shows original spectrum and lower panel shows background subtracted spectrum.*
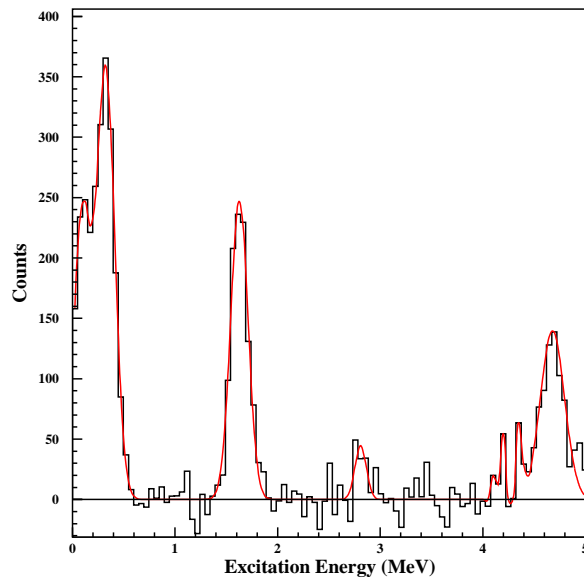
Figure 5.4: *Gaussian fits to peaks observed in lower section of ^{19}Ne excitation energy spectrum for $E_{lab} = 44.1$ MeV.*
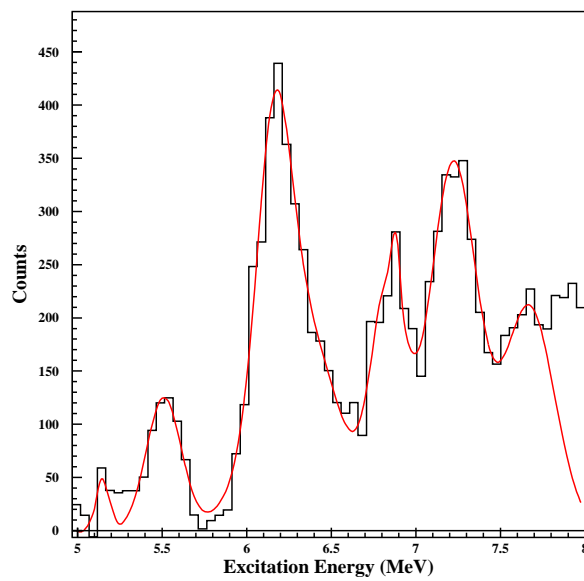
Figure 5.5: *Gaussian fits to peaks observed in higher section of ^{19}Ne excitation energy spectrum for $E_{lab} = 44.1$ MeV.*
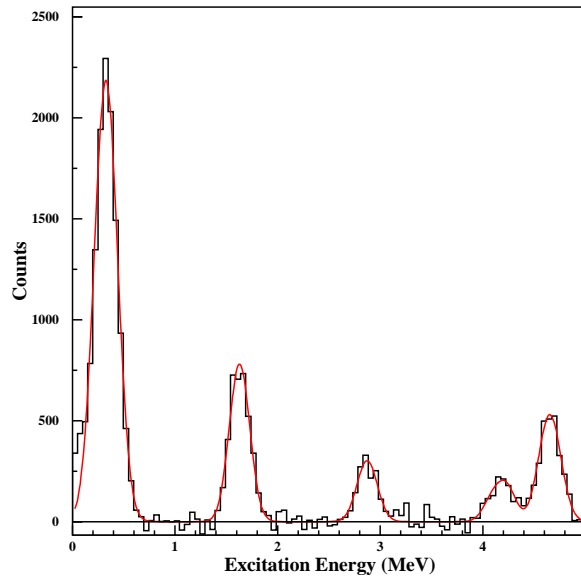
Figure 5.6: *Gaussian fits to peaks observed in lower section of ^{19}Ne excitation energy spectrum for $E_{lab} = 54.3$ MeV.*
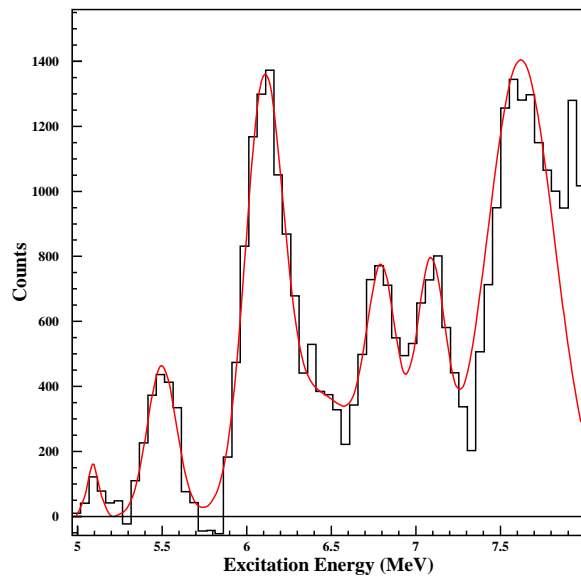
Figure 5.7: *Gaussian fits to peaks observed in higher section of ^{19}Ne excitation energy spectrum for $E_{lab} = 54.3$ MeV.*
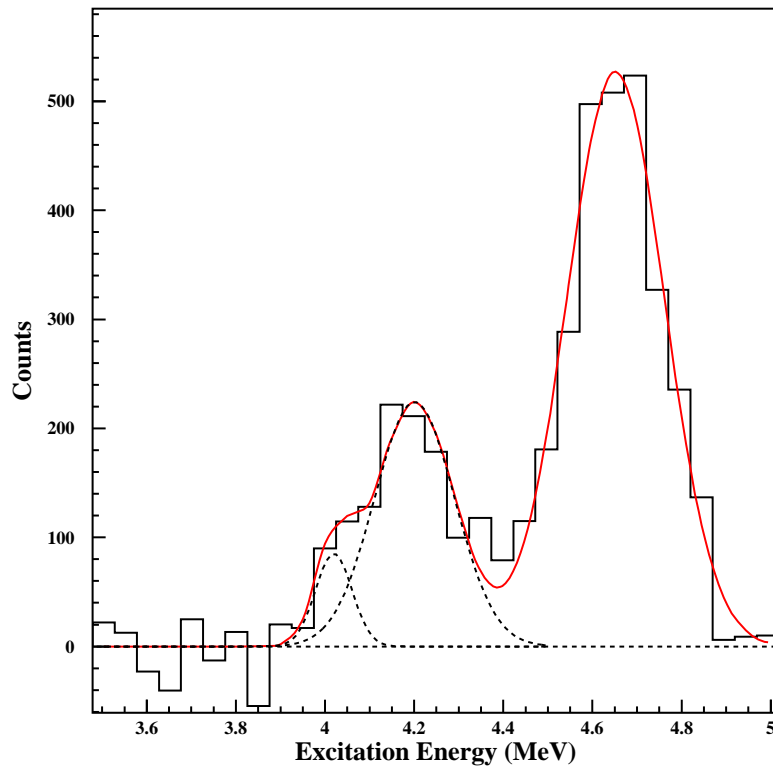
Figure 5.8: *Fit to region of ^{19}Ne excitation energy spectrum of astrophysical interest for $E_{lab} = 54.3$ MeV. Dashed lines show Gaussian deconvolution and red line shows resultant fit. The doublet at 4.140 and 4.197 MeV are described by one curve as they lie less than one channel apart.*

$E_{lab} = 54.3$ MeV, there is stronger evidence for its population. A magnified excitation energy spectrum of the region of astrophysical interest is shown in figure 5.8. The peak at 4.2 MeV corresponds to the unresolved doublet at 4.140 and 4.197 MeV. At the lower end of this peak there is an excess of counts which corresponds to the formation of the 4.033 MeV state. A Gaussian deconvolution of this region (dashed lines) yields a cross section of 25 $\pm$ 5 μb/sr.

5.2 Reaction Angular Distributions

Using the yields determined from the fits to the ^{19}Ne excitation energy spectra, angular distributions were calculated for each of the fitted peaks. The formulae used are given in appendix D. Angular distributions for $E_{lab} = 44.1$ MeV are shown in figures 5.9, 5.10 and 5.11. Due to the low statistics in the ringed spectra, each four consecutive rings were added to give four resultant excitation energy spectra. Fits were made to each of these spectra individually to give four points for each angular distribution. Although sixteen peaks were fitted in the summed spectra (figures 5.4 and 5.5), angular distributions are only given for the nine peaks where the statistics allowed a reasonable fit to the data. Angular distributions for $E_{lab} = 54.3$ MeV are given in figures 5.12, 5.13, 5.14 and 5.15. As with the $E_{lab} = 44.1$ MeV data, the statistics were not sufficient to fit each of the sixteen ringed spectra and so rings were added together. However, the statistics were better than for the $E_{lab} = 44.1$ MeV data and adding each two consecutive rings provided enough statistics to fit the data satisfactorily, giving eight points for each angular distribution.

5.3 Triple Coincidence Spectra

In order to obtain information on the decay properties of these states, i.e. branching ratios, it is necessary to have information on coincidences between the protons detected in LEDA3 and decay particles in LEDA1 and LEDA2. The channel of interest is α-decay and so coincidences between a proton, an α-particle and a heavy residue were demanded. Using a subset of the raw data which only included events containing three or more particles, the
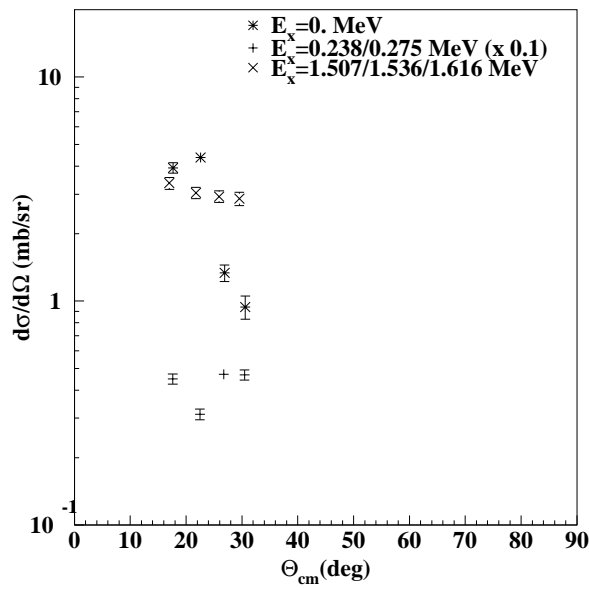
Figure 5.9: *Angular distributions for states, up to 2 MeV, populated in ^{19}Ne via the d(^{18}Ne,^{19}Ne*)p reaction at $E_{lab} = 44.1$ MeV.*
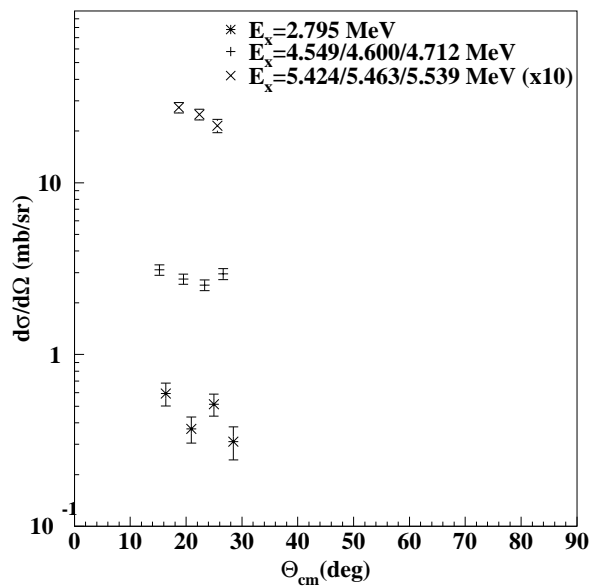
Figure 5.10: *Angular distributions for states, between 2 and 6 MeV, populated in ^{19}Ne via the d(^{18}Ne,^{19}Ne*)p reaction at $E_{lab} = 44.1$ MeV.*
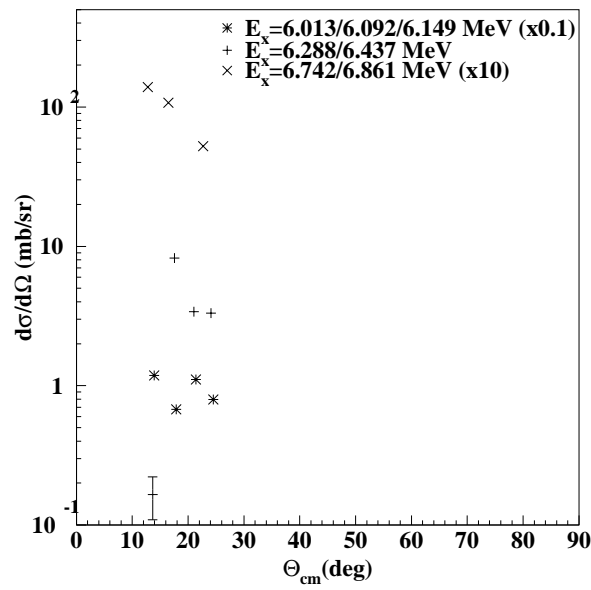
Figure 5.11: *Angular distributions for states between 6 and 7 MeV populated in ^{19}Ne via the $d(^{18}Ne,^{19}Ne^*)p$ reaction at $E_{lab} = 44.1$ MeV.*
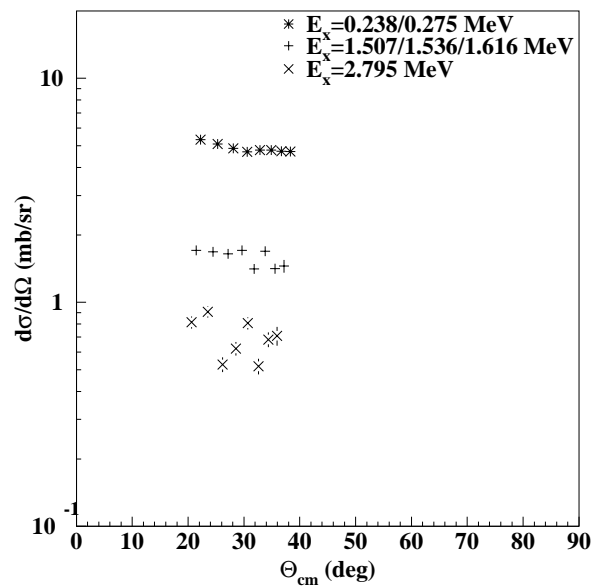
Figure 5.12: *Angular distributions for states, up to 3 MeV, populated in ^{19}Ne via the $d(^{18}Ne,^{19}Ne^*)p$ reaction at $E_{lab} = 54.3$ MeV.*
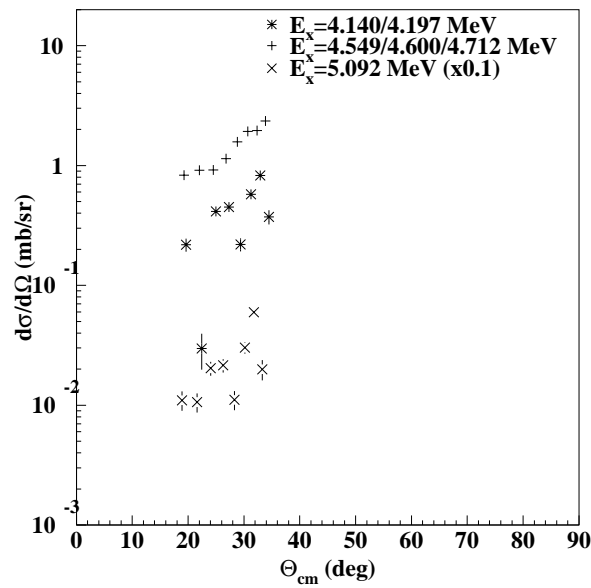
Figure 5.13: *Angular distributions for states, between 3 and 5.1 MeV, populated in ^{19}Ne via the $d(^{18}Ne,^{19}Ne^*)p$ reaction at $E_{lab} = 54.3$ MeV.*
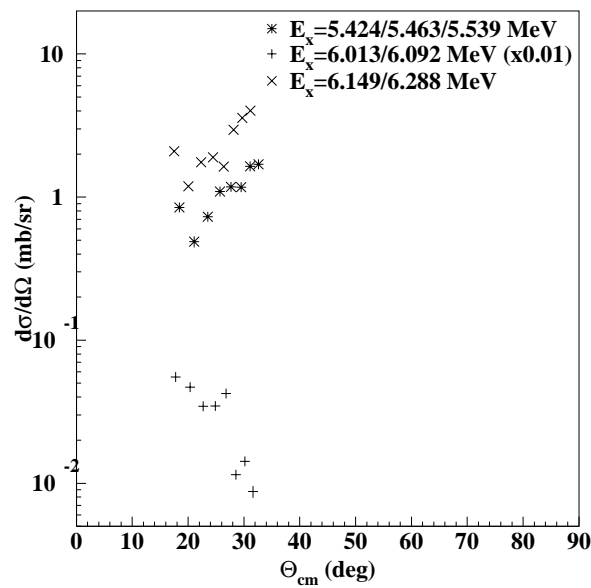
Figure 5.14: *Angular distributions for states, between 5.1 and 6.5 MeV, populated in ^{19}Ne via the $d(^{18}Ne,^{19}Ne^*)p$ reaction at $E_{lab} = 54.3$ MeV.*
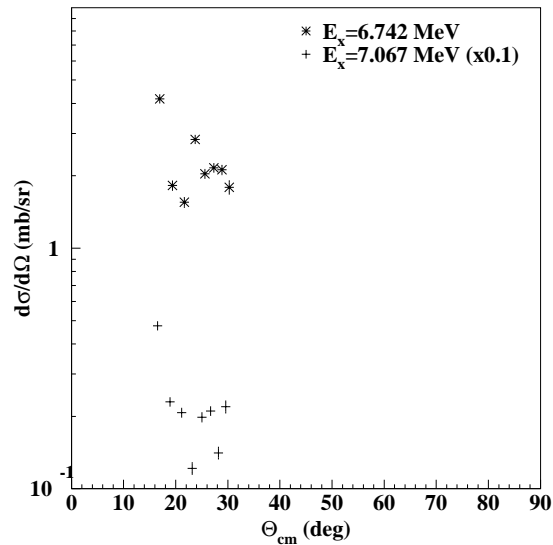
Figure 5.15: *Angular distributions for states, above 6.5 MeV, populated in ^{19}Ne via the d(^{18}Ne,$^{19}Ne^*$)p reaction at E_{lab} = 54.3 MeV.*

proton energy-time gate as described above was applied. For each event, it was tested whether or not there was a particle in LEDA3 falling inside the energy-time gate. A similar gate which identified prompt α-particles in either LEDA1 or LEDA2 was then applied, an example of which is shown in figure 5.16. If the event also contained such a particle, the energies of each of the three particles were added together. Then it was checked whether this total energy was consistent with the events of interest, i.e. if the total energy was equal to the beam energy plus the Q-value minus energy losses. The total energy spectrum for E_{lab} = 54.3 MeV is shown in figure 5.17. The events of interest correspond to the narrow peak at around 55 MeV in this figure. The last requirement on the events was the appropriate angular correlation between the α-particle and the heavy residue. The spectra resulting from the above requirements are shown in figures 5.18 and 5.19.
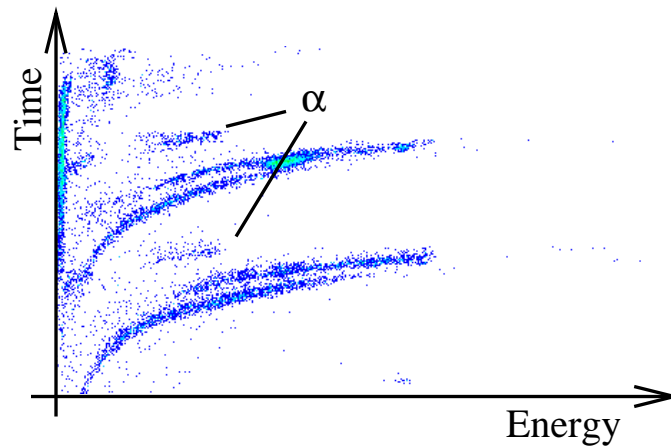
Figure 5.16: *Energy-time spectrum for LEDA2 ($E_{lab} = 54.3$ MeV) showing α-particle loci. There are two such loci because the acquisition gate was wider than the time between successive beam pulses.*
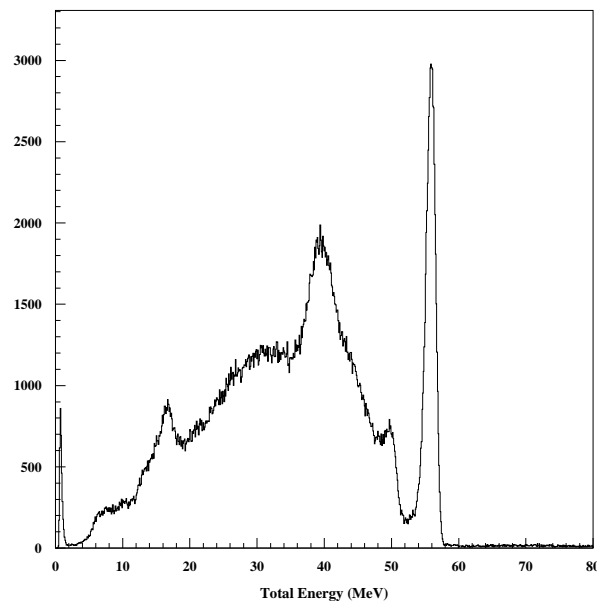
Figure 5.17: *Summed energy spectrum of triple coincidences for $E_{lab} = 54.3$ MeV (see text).*
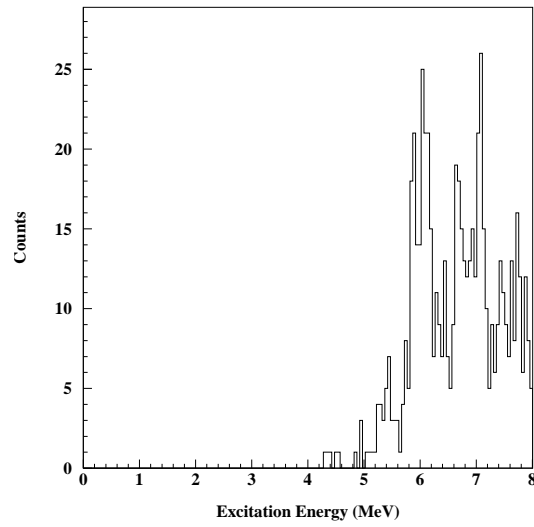
Figure 5.18: *Triple coincidence excitation energy spectrum for $d(^{18}Ne,p)^{19}Ne^*(\alpha)^{15}O$ for $E_{lab} = 44.1$ MeV.*
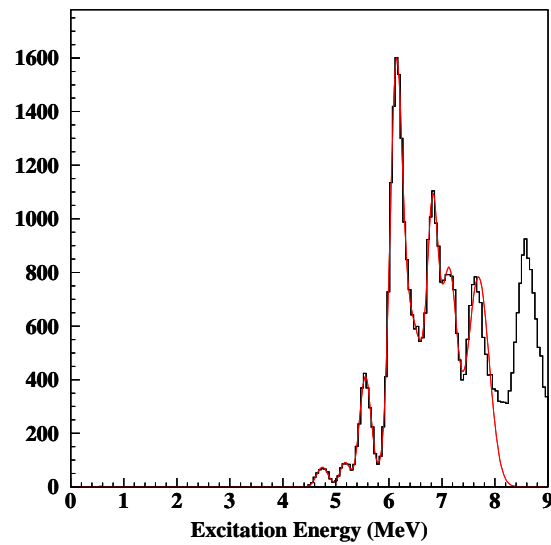
Figure 5.19: *Triple coincidence excitation energy spectrum for $d(^{18}Ne,p)^{19}Ne^*(\alpha)^{15}O$ for $E_{lab} = 54.3$ MeV. The red line denotes the result of Gaussian fits to the peaks.*

5.4   Branching Ratios

Branching ratios for the states in ^{19}Ne were determined by dividing the yield for a given peak in the triple spectrum with that determined from the singles spectrum. The detection efficiency was taken into account by multiplying by the probability that for a given proton detected in LEDA1, the corresponding α and ^{15}O would be detected in LEDA1 and LEDA2. This was determined by using the Monte Carlo simulation, UNIMONTE[69] under the assumption that the ^{19}Ne decays isotropically in the centre-of-mass. The calculated branching ratios are given in table 5.1 and compared with previous measured and theoretical values.

All branching ratios, except the upper limit for the 4.379 MeV state, are derived from the data for E_{lab} = 54.3 MeV. The statistics were insufficient to derive any information on the other branching ratios. The upper limit derived for the 4.033 MeV state is in agreement with the theoretical value calculated by Langanke[57]. The branching ratio for the 4.600 MeV state is in agreement, within error bars, with that calculated by Magnus et al.[56], as is the upper limit determined for the 4.379 MeV state. For the two states between 5.0 and 6.0 MeV, the calculated branching ratios are higher than expected, particularly for the 5.092 MeV state. This is probably due to background events from fusion on deuterium which have been subtracted in the singles spectra but not from the triples.

^{19}Ne E$_x$ (MeV)	B$_\alpha$ (present work)	B$_\alpha$ (previous work[56])
4.033	< 0.01	(10^{-4})
4.379	< 0.2	0.044 ± 0.032
4.549	-	0.07 ± 0.03
4.600	0.32 ± 0.03	0.25 ± 0.04
4.712	-	0.82 ± 0.15
5.092	1.8 ± 0.9	0.90 ± 0.09
5.351/5.424/5.463	1.3 ± 0.3	-
6.013/6.092	0.96 ± 0.2	-

Table 5.1: *Branching ratios from the present and previous experimental studies (The value in brackets is a theoretical estimate by Langanke et al.[57].)*

Chapter 6

Theoretical Interpretation

This chapter describes the theoretical interpretation of the experimental results. Firstly, optical potentials for d+^{18}Ne were obtained by fitting the elastic scattering data at both energies. Then, using these potentials together with p+^{19}Ne and n+^{18}Ne potentials, theoretical angular distributions were calculated using the distorted wave Born approximation (DWBA) for several excited states in ^{19}Ne. These distributions were compared with the experimental angular distributions, given in section 5.2, and spectroscopic factors derived. Finally, a reaction rate calculation was performed using the branching ratios given in table 5.1.

6.1   Optical Model Fits

The optical model was developed to describe elastic scattering in the presence of absorptive effects, i.e removal of particle flux from the elastic channel into other exit channels. The basic assumption is that all the individual nucleon-

nucleon interactions between the target and projectile nuclei can be described by a single one-body central potential, V(r), where r is the projectile-target separation distance. A knowledge of the nucleon-nucleon potential suggested that V(r) should be uniform inside the nucleus and fall off rapidly beyond the nuclear surface. Consequently, the potential usually used has a so-called Woods-Saxon shape given by

$$V(r) = \frac{-V_o}{1 + e^{x_i}} \tag{6.1}$$

where V_o is the potential depth, x_i=(r-RA$^{1/3}$)/a, R is the radius and a is the diffuseness parameter. However, to account for the absorption into channels other than elastic scattering, a complex potential of the form

$$U(r) = V(r) + iW(r) \tag{6.2}$$

is used. W(r) is responsible for the removal of flux from the elastic channel and at low energies is often taken to be the first derivative of a Woods-Saxon potential, W_D, which is peaked at the nuclear surface. This corresponds to only surface nucleons participating in absorption at these energies. In addition, two other potential terms should be included. In the case of charged particles, a Coulomb potential given by

$$V_c(r \leq R_c) = \frac{1}{4\pi\epsilon_o} \frac{Z_p Z_t}{2R_c} \left(3 - \frac{r^2}{R_c^2}\right) \tag{6.3}$$

and

$$V_c(r > R_c) = \frac{1}{4\pi\epsilon_o} \frac{Z_p Z_t e^2}{r} \tag{6.4}$$

is commonly used. Here, Z_p is the projectile charge, Z_t is the target charge and R_c is the Coulomb radius. The second potential term arises from the

spin-orbit interaction and is given by

$$V_{so}(r) = (\frac{\hbar}{m_\pi c})^2 V_{so} L.\sigma \frac{1}{r} \frac{df(x_{so})}{dr} \tag{6.5}$$

where f(x$_{so}$) has a Woods-Saxon form. Thus the total potential becomes

$$U(r) = V_c(r) - V_o f(x_o) + i4W_D \frac{d}{dx_D} f(x_D) + (\frac{\hbar}{m_\pi c})^2 V_{so} L.\sigma \frac{1}{r} \frac{df(x_{so})}{dr} \tag{6.6}$$

Optical model fits to d(^{18}Ne,^{18}Ne) experimental data were performed to provide optical potentials for use in the subsequent DWBA calculations. The code **CUPID**[82] was used to fit these data and initial parameters were taken from Lohr and Haeberli[83] and Perey and Perey[84]. The initial parameters were chosen from typical values for nuclei in this mass range. The final parameters derived, for both beam energies, are given in table 6.1 and the fits along with the experimental data sets are shown in figures 6.1 and 6.2. Initially, the fit to the E$_{lab}$=44.1 MeV was attempted by allowing only the real and imaginary well depths to vary. However, the resultant fit failed to reproduce even the general form of the data. Consequently, the real and imaginary radius and diffuseness values were also allowed to vary to obtain the final fit shown in figure 6.1. For the E$_{lab}$=54.3 MeV, however, the best fit was obtained by varying only the well depths and not all six aforementioned parameters.

The elastic scattering distributions at both energies exhibit a minimum at around 100° and a rise in cross section at backward angles. Similar features were found by Davison et al.[85] for the elastic scattering of deuterons by ^{16}O in the same centre of mass energy range. Davison et al.[85] also found

that the optical model fits to their data were significantly improved by the inclusion of a spin-orbit term. However, due to the inverse kinematics, the cut-off angle for elastic scattering on deuterons in this work was 6.4 degrees. Unfortunately, the available angular resolution in LEDA1 yielded only five data points in this angular range. Including the spin-orbit potential did not improve the fit significantly and introduced an extra three parameters to a system with already more parameters than data points. Consequently the fitted d+^{18}Ne potentials do not include spin-orbit terms. The p+^{19}Ne and the n+^{18}Ne potentials are taken from [86] and [58] respectively.

Potential	V_o [MeV]	r_o [fm]	a_o [fm]	W_D [MeV]	r_D [fm]	a_D [fm]	V_{so} [MeV]	r_{so} [fm]	a_{so} [fm]	r_c [fm]
d+^{18}Ne (runI)	94.55	1.14	0.71	10.88	1.34	0.59				1.15
d+^{18}Ne (runII)	97.46	1.05	0.86	32.53	1.43	0.59				1.30
p+^{19}Ne	48.43	1.25	0.65	13.5	1.25	0.47	7.5	1.25	0.47	1.25
n+^{18}Ne	57.90	1.25	0.65							1.25

Table 6.1: *Optical model potential parameters.*
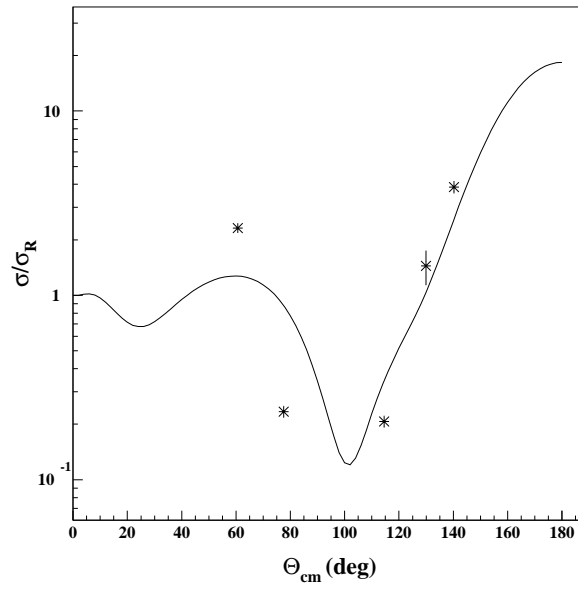
Figure 6.1: *Elastic scattering data for $d(^{18}Ne,^{18}Ne)$, at $E_{lab} = 44.1$ MeV, with optical model fit.*
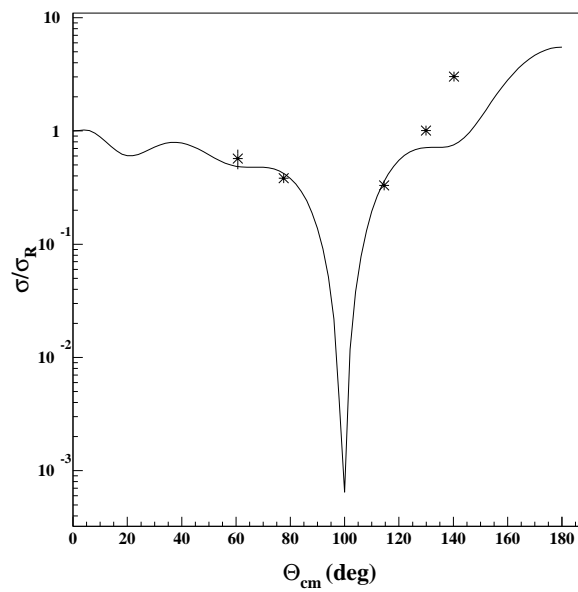
Figure 6.2: *Elastic scattering data for $d(^{18}Ne,^{18}Ne)$, at $E_{lab} = 54.3$ MeV, with optical model fit.*

6.2 Distorted Wave Born Approximation Calculations

The distorted wave Born approximation is one of the most commonly used models for calculating angular distributions for transfer reactions and has been particularly successful in the case of (d,p) reactions. Comparison between experimental and DWBA angular distributions allows information on the structure of the populated states to be deduced. The single particle nature of states can be investigated and spin and parity values can be determined.

The DWBA calculations presented in this section were performed using the code **DWUCK4**[64]. A brief outline is given below and more detailed descriptions of the use of DWBA to study transfer reactions can be found in [87] and [81].

For the reaction A(d,p)B, the DWBA cross section can be written as

$$\frac{d\sigma}{d\Omega} = \frac{\mu_i \mu_f}{(2\pi\hbar^2)^2} \frac{k_f}{k_i} \frac{1}{(2I_d + 1)(2I_A + 1)} \sum_{m_i m_f} |T_{m_i m_f}|^2 \qquad (6.7)$$

where all the symbols have their usual meanings and the summation is over the inital and final spin projections. The transition amplitude, T, is given by

$$T = \int \chi_f^{(-)*}(\mathbf{k_f}, \mathbf{r_f}) \langle pB|V|dA \rangle \chi_i^{(-)}(\mathbf{k_i}, \mathbf{r_i}) \qquad (6.8)$$

where χ^+ and χ^- are the incoming and outgoing distorted waves describing elastic scattering in the initial and final channels, respectively. The parameters $\mathbf{r_i}$ and $\mathbf{r_f}$ are the distances between the mass centres of the colliding nuclei in the initial and final channels. V is the perturbing potential described by

$$V = V_{pB} - U_f \approx V_{pn} + V_{pA} + U_f \qquad (6.9)$$

where V_{pB} represents the true interaction between the proton and B, in this case the ^{19}Ne, and U_f is the optical model potential describing the final channel. The potential V_{pn} is between the proton and the neutron and V_{pA} is the potential between the proton and A, in this case ^{18}Ne. This relation is given in the 'post' form as this is appropriate for transfers from a light to a heavier nucleus.

The spectroscopic factor gives a measure of the overlap between the wavefunction of a state and its populating channel. In this case, it describes how well the states in ^{19}Ne can be described as ^{18}Ne plus a valence neutron, i.e. if this is an appropriate description, the state can be described by the single particle model and the spectroscopic factor will be of the order of one. For states with more complicated structures, the spectroscopic factor will be much smaller. The spectroscopic factor, S, can be determined by normalising the theoretical angular distributions to that determined experimentally, i.e.

$$\left(\frac{d\sigma}{d\Omega}\right)_{exp} = S\left(\frac{d\sigma}{d\Omega}\right)_{DWBA} \tag{6.10}$$

Since the structure of a particular state, single particle or otherwise, is independent of the reaction populating it, the spectroscopic factor should be independent of the beam energy and thus the values determined for the two experiments should be comparable.

The DWBA calculations for both beam energies are given in the following figures together with the relevant experimental data sets. The resultant spectroscopic factors are given in table 6.2. However, it must be noted that the information that can be derived from these calculations is limited due to the limited angular range of the data and the low statistics.
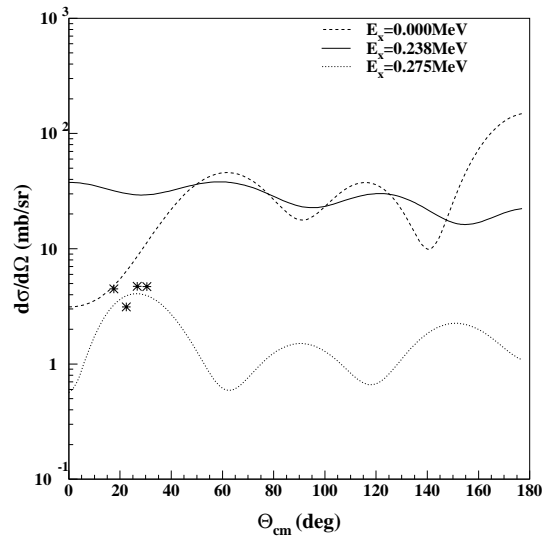
Figure 6.3: *DWBA calculations for $d(^{18}Ne,^{19}Ne^*)p$ at $E_{lab} = 44.1$ MeV for $E_x=0.0(1/2^+)/0.238(5/2^+)/0.275(1/2^-)$ MeV with experimental data points.*
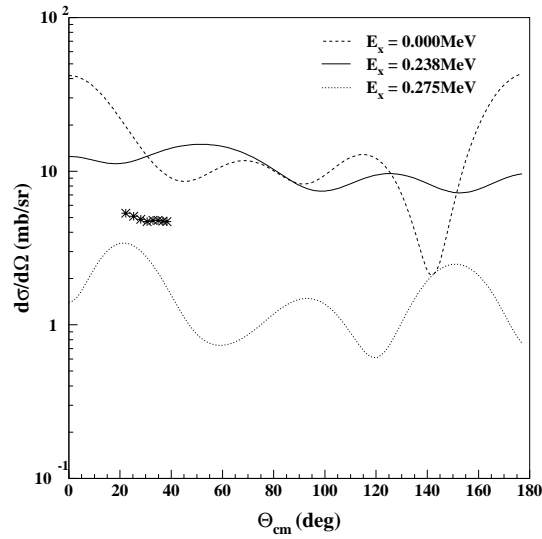
Figure 6.4: *DWBA calculations for $d(^{18}Ne,^{19}Ne^*)p$ at $E_{lab} = 54.3$ MeV for $E_x=0.0(1/2^+)/0.238(5/2^+)/0.275(1/2^-)$ MeV with experimental data points.*
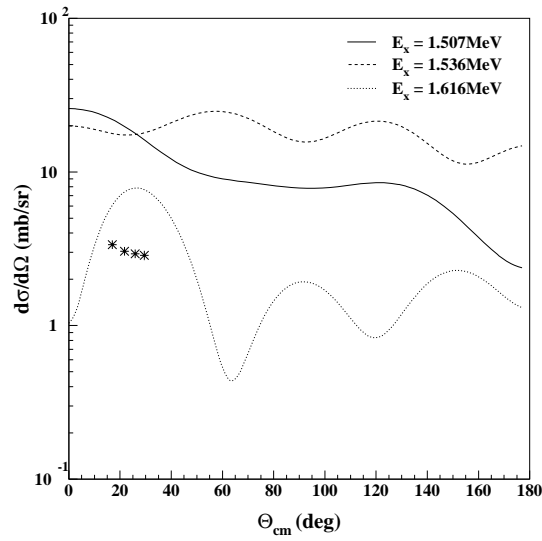
Figure 6.5: *DWBA calculations for $d(^{18}Ne,^{19}Ne^*)p$ at $E_{lab} = 44.1$ MeV for $E_x=1.507(5/2^-)/1.536(3/2^+)/1.616(3/2^-)$ MeV with experimental data points.*
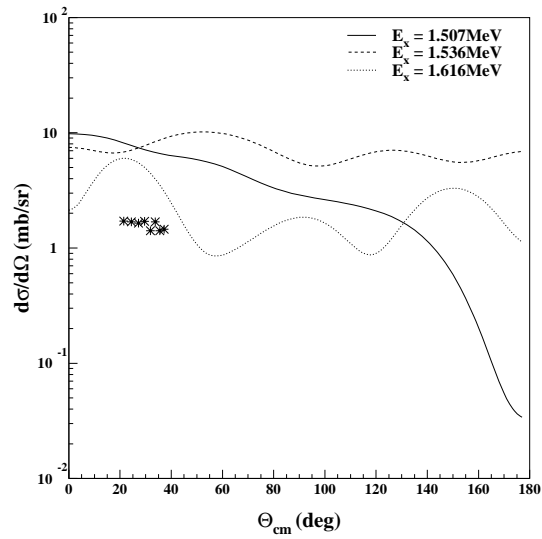
Figure 6.6: *DWBA calculations for $d(^{18}Ne,^{19}Ne^*)p$ at $E_{lab} = 54.3$ MeV for $E_x=1.507(5/2^-)/1.536(3/2^+)/1.616(3/2^-)$ MeV with experimental data points.*
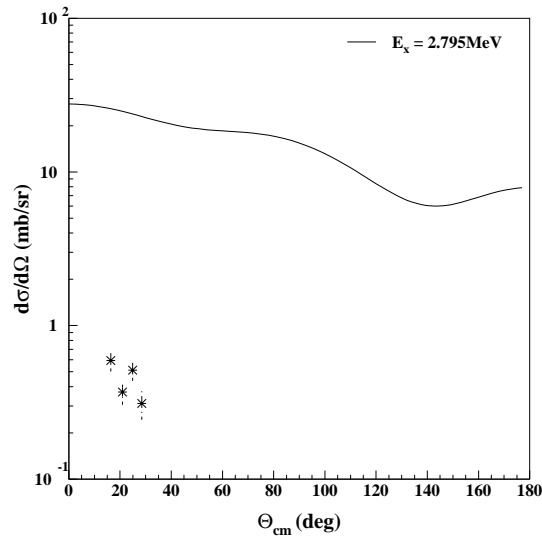
Figure 6.7: *DWBA calculations for $d(^{18}Ne,^{19}Ne^*)p$ at $E_{lab} = 44.1$ MeV for $E_x = 2.795(9/2^+)$ MeV with experimental data points.*
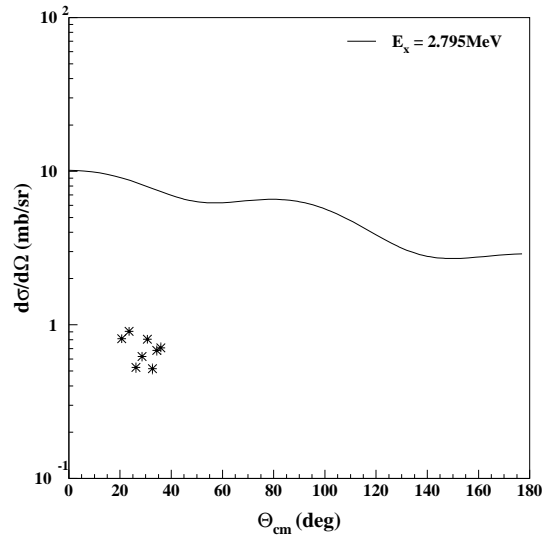
Figure 6.8: *DWBA calculations for $d(^{18}Ne,^{19}Ne^*)p$ at $E_{lab} = 54.3$ MeV for $E_x = 2.795(9/2^+)$ MeV with experimental data points.*
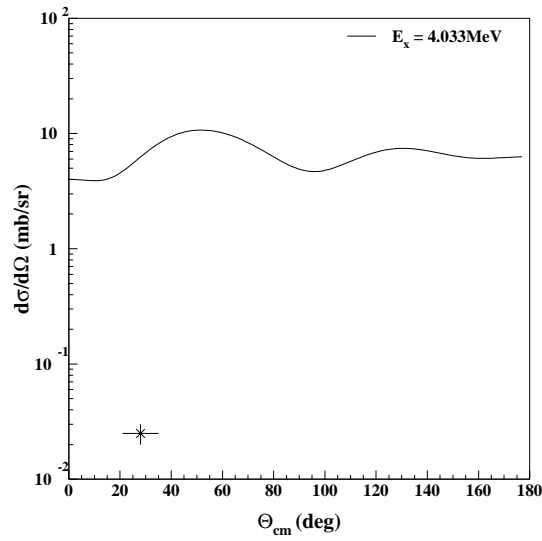
Figure 6.9: *DWBA calculations for $d(^{18}Ne,^{19}Ne^*)p$ at E_{lab} = 54.3 MeV for E_x =4.033(3/2$^+$) MeV with the experimental data point.*
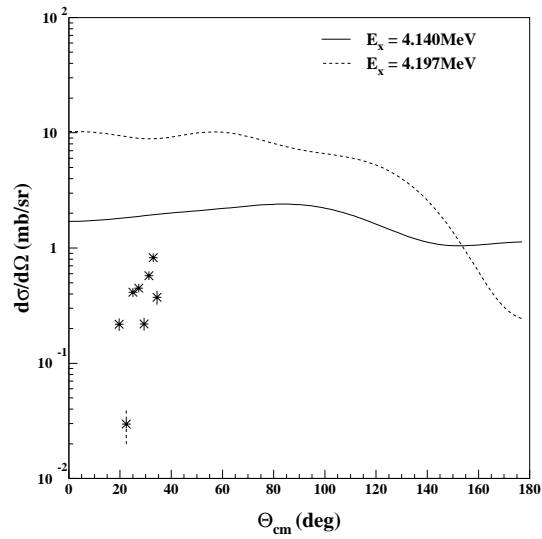
Figure 6.10: *DWBA calculations for $d(^{18}Ne,^{19}Ne^*)p$ at E_{lab} = 54.3 MeV for E_x =4.140(9/2$^-$)/4.197(7/2$^-$) MeV with experimental data points.*
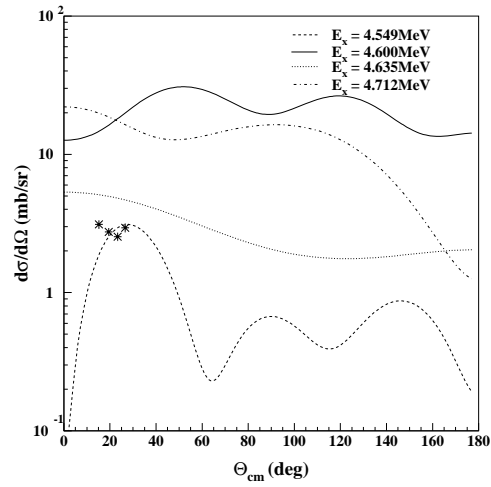
Figure 6.11: *DWBA calculations for $d(^{18}Ne,^{19}Ne^*)p$ at $E_{lab} = 44.1$ MeV for $E_x=4.549(3/2^-,1/2^-)/4.600(5/2^+)/4.635(13/2^+)/4.712(5/2^-)$ MeV with experimental data points.*
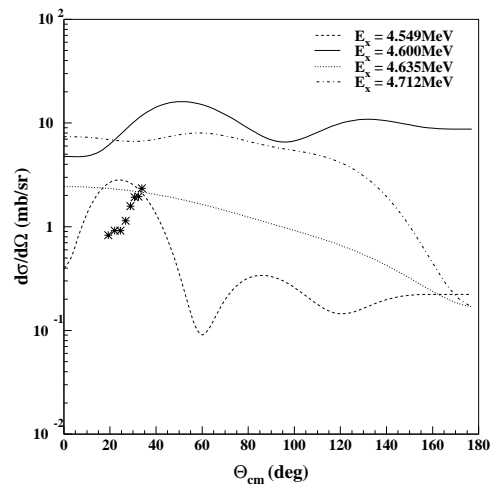
Figure 6.12: *DWBA calculations for $d(^{18}Ne,^{19}Ne^*)p$ at $E_{lab} = 54.3$ MeV for $E_x=4.549(3/2^-,1/2^-)/4.600(5/2^+)/4.635(13/2^+)/4.712(5/2^-)$ MeV with experimental data points.*
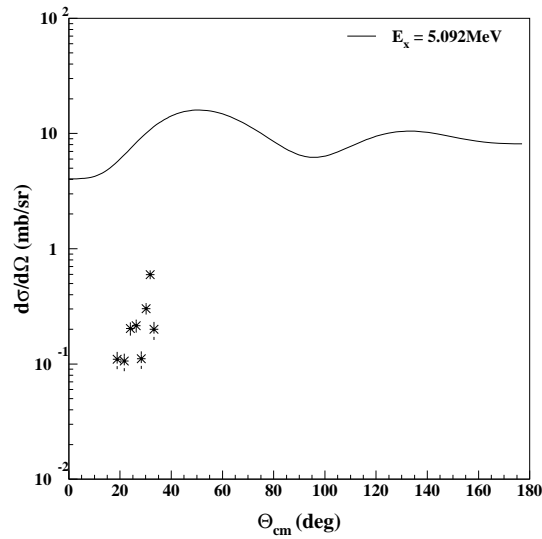
Figure 6.13: *DWBA calculations for $d(^{18}Ne,^{19}Ne^*)p$ at $E_{lab} = 54.3$ MeV for $E_x = 5.092(5/2^+)$ MeV with experimental data points.*
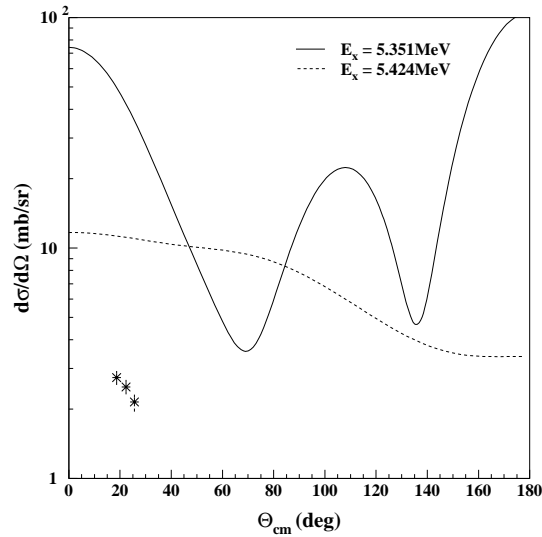
Figure 6.14: *DWBA calculations for $d(^{18}Ne,^{19}Ne^*)p$ at $E_{lab} = 44.1$ MeV for $E_x = 5.351(1/2^+)/5.424(7/2^+)$ MeV with experimental data points.*
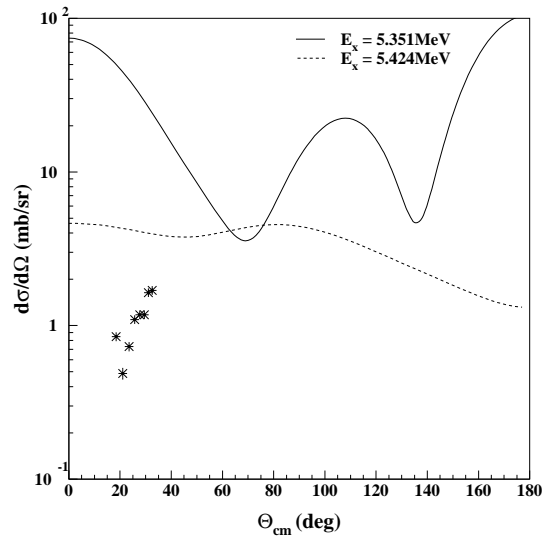
Figure 6.15: *DWBA calculations for $d(^{18}Ne,^{19}Ne^*)p$ at $E_{lab} = 54.3$ MeV for E_x=5.351(1/2$^+$)/5.424(7/2$^+$) MeV with experimental data points.*
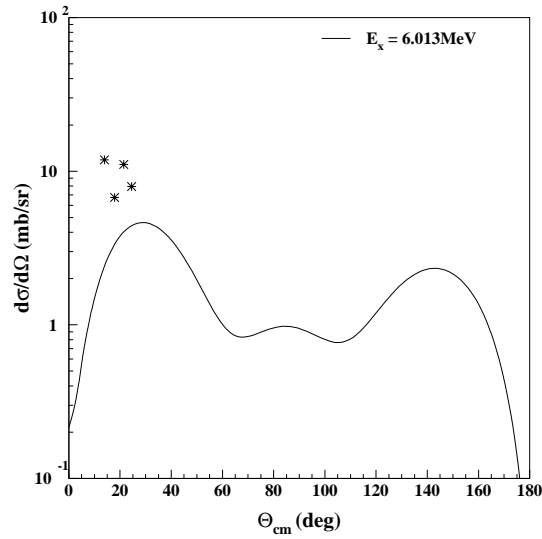
Figure 6.16: *DWBA calculations for $d(^{18}Ne,^{19}Ne^*)p$ at $E_{lab} = 44.1$ MeV for E_x=6.013(3/2$^-$,1/2$^-$) MeV with experimental data points.*
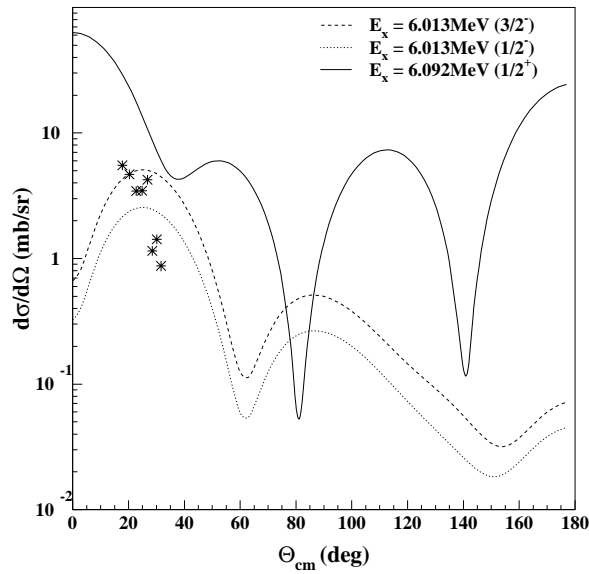
Figure 6.17: *DWBA calculations for $d(^{18}Ne,^{19}Ne^*)p$ at $E_{lab} = 54.3$ MeV for $E_x = 6.013(3/2^-, 1/2^-)/6.092(1/2^+)$ MeV with experimental data points.*
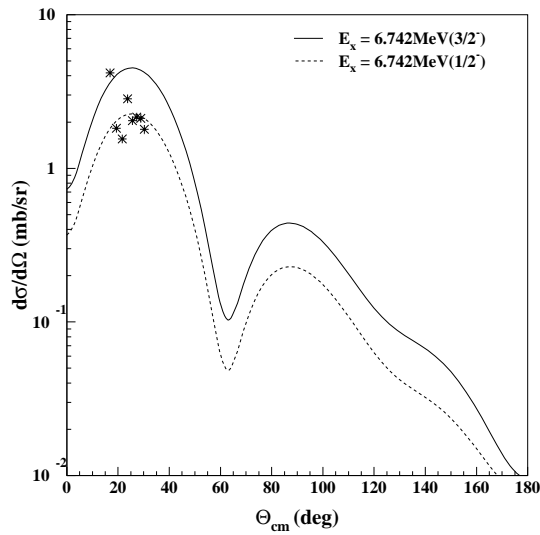
Figure 6.18: *DWBA calculations for $d(^{18}Ne,^{19}Ne^*)p$ at $E_{lab} = 54.3$ MeV for $E_x = 6.742(3/2^-, 1/2^-)$ MeV with experimental data points.*

6.3   Discussion

6.3.1   The ground state ($1/2^+$), 0.238 MeV ($5/2^+$) and 0.275 MeV ($1/2^-$) triplet

A comparison between the experimental data points and the DWBA calculations for the three levels is shown in figure 6.3 for $E_{lab} = 44.1$ MeV (runI) and in figure 6.4 for $E_{lab} = 54.3$ MeV (runII). Both figures suggest that the angular distribution calculated for the 0.238 MeV state best fits the data points. The calculated spectroscopic factors are given in table 6.2. The discrepancy between the two values obtained at the two beam energies is probably due to differences in the fits used to the excitation energy spectra. In the $E_{lab} = 44.1$ MeV excitation energy spectrum there is evidence that the lowest peak is actually the convolution of two states and was fitted as such, as shown in fig. 5.4). Thus the yield for the 0.238 MeV state may be higher than calculated due to the limitations of attempting to fit states which are so close together.

6.3.2   The 1.507 MeV ($5/2^-$), 1.536 MeV ($3/2^+$) and 1.616 MeV ($3/2^-$) triplet

The second peak in the excitation energy spectra may be due to either one or a combination of three levels. Figures 6.5 and 6.6 show that the DWBA calculations, at both energies, indicate that it is the state at 1.507 MeV that is most probably populated. The calculated spectroscopic factors, given in table 6.2, agree well within the experimental limits.

6.3.3 The 2.795 MeV ($9/2^+$) level

This state is sufficiently distant from other states to be unambiguously identi-
fied. It was observed at both beam energies and angular distributions at both
energies were calculated. These distributions are shown in figures 6.7 and 6.8.
The spectroscopic factor was determined for both energies, and these values
are given in table 6.2. There is some discrepancy between the two values.
This may be due to differences between the subtracted background in the
two cases.

6.3.4 The 4.033 MeV ($3/2^+$) level

For this state, only runII ($E_{lab} = 54.3$ MeV) provided evidence for its popu-
lation. The statistics were insufficient to obtain an angular distribution and
so only a single cross section value and an upper limit to the α branching
ratio were determined. Previous work by Fortune et al.[88] used the reaction
^{21}Ne(p,t)^{19}Ne to study the configuration of this state. The results suggest
that this state has a complex structure consisting of ($2s_{1/2}$) and ($1d_{3/2}$) con-
tributions. Nevertheless, an attempt was made to obtain a spectroscopic
factor (see fig. 6.9) and the value is given in table 6.2.

6.3.5 The 4.140 MeV ($9/2^-$) and 4.197 MeV ($7/2^-$) doublet

A comparison between the DWBA calculations for these two states and ex-
perimental data points was only possible for the higher beam energy ($E_{lab} =$
54.3 MeV) and is shown in figure 6.10. Although there is some evidence for

their population at the lower beam energy, the lack of statistics prohibited any further analysis. Figure 6.10 shows a large scatter in the data points and their general trend agrees with neither of the two DWBA calculations. Due to this no information on the relative population of the two states could be derived.

6.3.6 The 4.379 MeV ($7/2^+$) level

This state was only observed at $E_{lab} = 44.1$ MeV (runI) and the statistics were insufficient to derive an angular distribution. However, as with the state at 4.033 MeV, an upper limit for the branching ratio was obtained as shown in table 5.1.

6.3.7 The 4.549 MeV ($3/2^-$,$1/2^-$), 4.600 MeV ($5/2^+$), 4.635 MeV ($13/2^+$) and 4.712 MeV ($5/2^-$) group

Figures 6.11 and 6.12 show the DWBA calculations for these four states together with the experimental data points. Figure 6.11 suggests that both the 4.600 MeV and the 4.712 MeV levels contribute to the data, with the 4.712 MeV level dominating at lower angles and the 4.600 MeV contribution increasing for higher angles. Figures 6.12 however indicates that at $E_{lab} =$ 54.3 MeV the 4.600 MeV dominates and in fact reproduces the data almost perfectly. The spectroscopic factors calculated at the two beam energies agree very well.

6.3.8   The 5.092 MeV ($5/2^+$) level

As with the 2.795 MeV state, this level is well separated from the adjacent states. However, an angular distribution was only obtained for $E_{lab} = 54.3$ MeV due to low statistics for the data obtained at $E_{lab} = 44.1$ MeV. Unfortunately, there is scatter in the data points (see fig. 6.13). Nevertheless, the general trend follows the DWBA distribution and the spectroscopic factor obtained is given in table 6.2.

6.3.9   The 5.351 MeV ($1/2^+$), 5.424 MeV ($7/2^+$) and 5.463 MeV triplet

Since J^π values are only available for the 5.351 MeV and 5.424 MeV states, a DWBA calculation was not performed for the 5.463 MeV level. Figure 6.14 indicates that for the $E_{lab} = 44.1$ MeV calculation the 5.351 MeV distribution seems to follow the data very well and a spectroscopic factor was calculated. For the $E_{lab} = 54.3$ MeV data, figure 6.15 shows however that the trend of the data points does not agree with either DWBA calculation. This suggests that at the higher energy, the peak observed in the excitation energy spectrum is due to either the 5.463 MeV state or a combination of all three levels.

6.3.10   The 6.013 MeV ($3/2^-$,$1/2^-$) and 6.092 MeV doublet

The DWBA calculations for the 6.013 MeV at the two beam energies are shown in figures 6.16 and 6.17. Neither reproduce the data particularly well.

This could suggest that it is the 6.092 MeV state that is populated. The DWBA calculation for this state was performed under the assumption that trend of the data obtained at $E_{lab} = 54.3$ MeV follows the behaviour of a $3s_{1/2}$ state, which might be populated at this excitation energy. The result of the calculation is shown in fig. 6.17 and the derived spectroscopic factor is given in table 6.2. This procedure was not followed for the $E_{lab} = 44.1$ MeV data due to the lack of data points.

6.3.11   The 6.288 MeV level

Due to the lack of spin and parity information on this state, no DWBA calculations were made. Several DWBA calculations were performed with various spin and parity values, but none followed the trend of the data and so no new information could be derived.

6.3.12   The 6.742 MeV (3/2$^-$,1/2$^-$) and 6.861 MeV levels

The excitation energy spectra for both beam energies show the population of a state or states in this energy range. However, a DWBA calculation could only be performed for the 6.742 MeV state since no spin and parity assignment is available for the 6.861 MeV. For $E_{lab} = 44.1$ MeV, there is an indication in the excitation energy spectrum (fig. 5.5) that there are contributions from both states. However, at $E_{lab} = 54.3$ MeV, the population of two states is less apparent in the excitation energy spectrum (fig. 5.7). Additionally, it is difficult to draw any conclusion from the comparison with the DWBA calculation for the $E_{lab} = 54.3$ MeV data, shown in Fig. 6.18, due to the

scatter in the data points.

6.3.13 The 7.067 MeV level

Figure 5.15 gives the angular distribution for this state at $E_{lab} = 54.3$ MeV data. As with the 5.092 MeV state, this level is well separated from adjacent states. However, no information on the J^π of this state was available. Various spin and parity assignments were tried but, as with the 6.288 MeV state, the resultant DWBA calculations failed to reproduce the trend in the data points.

6.4 Spectroscopic factors

^{19}Ne E_x [MeV]	Spectroscopic factors	
(J^π)	$E_{lab} = 44.1$ MeV (runI)	$E_{lab} = 54.3$ MeV (runII)
0.238 ($5/2^+$)	0.15 ± 0.04	0.4 ± 0.1
1.507 ($5/2^-$)	0.16 ± 0.04	0.20 ± 0.05
2.795 ($9/2^+$)	0.02 ± 0.01	0.08 ± 0.03
4.033 ($3/2^+$)	-	0.004 ± 0.002
4.600 ($5/2^+$)	0.15 ± 0.04	0.15 ± 0.04
5.092 ($5/2^+$)	-	0.02 ± 0.01
5.351 ($1/2^+$)	0.06 ± 0.02	-
6.092 ($1/2^+$)	-	0.2 ± 0.06

Table 6.2: *Spectroscopic factors for the reaction $d(^{18}Ne,^{19}Ne^*)p$ derived from a comparison between experimental and DWBA angular distributions at both beam energies.*

In order to attempt to verify the spectroscopic factors obtained, a comparison was made between the values obtained in this work and those obtained for the two similar reactions, ^{16}O(d,p)^{17}O and ^{18}O(d,p)^{19}O. These reactions were chosen as they provided information on similar neutron configurations to that of ^{19}Ne.

The shell structure for ^{19}Ne and ^{17}O both consist of an ^{16}O core with one valence neutron. Though ^{19}Ne has an additional proton pair, comparisons of the transfer of a neutron in the two cases can be made. In the case of ^{17}O, the ground state has $J^\pi = 5/2^+$ and the first excited state at $E_x = 0.871$ MeV has $J^\pi = 1/2^+$. For ^{19}Ne, however, the ground state has $J^\pi = 1/2^+$ and the first excited state at $E_x = 0.238$ MeV has $J^\pi = 5/2^+$. This suggests that the $1d_{5/2}$ and $2s_{1/2}$ shells are inverted in the case of ^{19}Ne. Thus the spectroscopic factors for the ground state in ^{17}O and the first excited state in ^{19}Ne should be compared. A study was made by Alty et al.[89] who found the ground state spectroscopic factor to be in range 0.33 - 0.6 depending on the optical model potentials used.

In the case of ^{19}O, there are three valence neutrons on the ^{16}O core. According to the shell model, these three neutrons will be found in the $1d_{5/2}$ shell. Thus as with the above argumentation, spectroscopic factors for the ^{19}O ground state should be compared with the first excited state in ^{19}Ne. The ^{18}O(d,p)^{19}O reaction has been investigated by Sen et al.[90] and spectroscopic factors for several states determined. For the ground state they find 0.57.

Both these values agree reasonably well with the value determined here at $E_{lab} = 54.3$ MeV. This gives some confidence in the values determined for other states since the same potentials and normalisation has been applied.

6.5 Reaction Rate Calculations
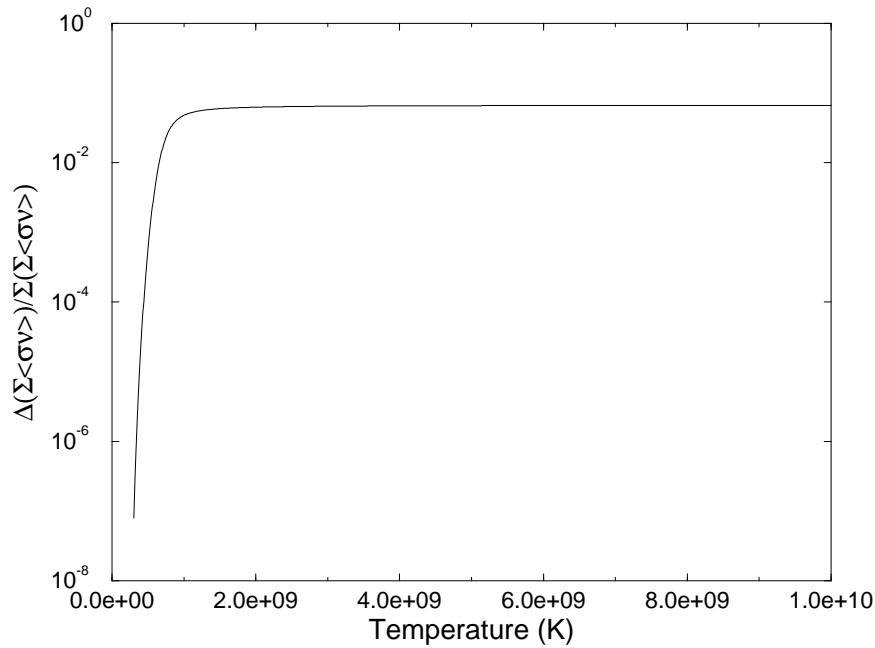
Figure 6.19: *Difference in total reaction rate, from that previously calculated by Magnus et al.[56], due to the new branching ratio value for the 4.600 MeV state determined in the present work.*

A calculation was performed to determine the effect of the new value for the 4.600 MeV branching ratio on the $^{15}O(\alpha,\gamma)^{19}Ne$ reaction rate. The total reaction rate for the resonances between 4.033 and 4.600 MeV was calculated using the values given by Magnus et al.[56]. The calculation was then repeated using the 4.600 MeV branching ratio determined in the present work. Figure 6.19 shows that difference between these two total reaction rates only becomes significant, i.e. of the order of a few percent, above about 8 x 10^8 K.

Chapter 7

Conclusions

Two experiments have been performed to investigate the (d,p) reaction in inverse kinematics using a post accelerated radioactive ^{18}Ne beam. Excited states up to 7 MeV have been populated in ^{19}Ne and angular distributions calculated for several of these states. Additionally, the α-decay of states above 4 MeV has been observed and α-branching ratios for four of these states determined. Evidence for the population of the 4.033 MeV state has been observed at E$_{lab}$=54.3 MeV. Although there was no such evidence at E$_{lab}$=44.1 MeV, this was probably due to the statistics which were eight times lower than at the higher beam energy. Due to the lack of statistics, the α-decay of the astrophysically important state at 4.033 MeV has not been observed, though an upper limit was derived.

A comparison was made between the derived branching ratios for the present work with those obtained by Magnus et al.[56] using a stable beam experiment. The results of Magnus et al. have better resolution for identifying the population of the states but have very low statistics for identifying

their decay. Both results agree for the state at 4.600 MeV within experimental limits. For lower states only upper limits could be derived for the present work though they do not contradict the current accepted values. However, for excited states above 5 MeV the branching ratios derived here are higher than expected. This could be due to one of two reasons. Firstly, the α-decay of ^{19}Ne may not be isotropic in the centre of mass as has been assumed. The actual distribution may be peaked in the angular range covered by the detectors and so the detection efficiency would be calculated too low, increasing the branching ratio. However, for these states above 5 MeV the geometrical efficiency is above 50% and so much of the effect of having a non-isotropic distribution would be integrated over. The alternative explanation is that there are some background events which have been accounted for in the single events by the background subtraction but not in the triple coincidence events. This would also result in higher branching ratios. The origin of the background must be related to reactions on deuterium. The background from the carbon in the target present in the singles spectra is well understood and the background present in the triple coincidence events is negligible. The observed background may be due to fusion on deuterium or the break up of deuterium in the Coulomb field of the ^{18}Ne.

Using the branching ratios determined in this work, a reaction rate calculation was performed and compared with that performed by Magnus et al.[56]. The difference in branching ratio for the 4.600 MeV state resulted in a change in the reaction rate of about 6% at a temperature of 10^9 K. While this will have little impact in novae scenarios, it may begin to be significant for X-ray bursters.

Using elastic scattering data, optical model parameters for the d+^{18}Ne potential were determined. DWBA calculations were performed and compared with experimental angular distributions. Spectroscopic factors were suggested for 8 states and a tentative spin assignment made for the 6.092 MeV state. However, these conclusions were reached with low statistics and a limited angular range for the data points. Higher statistics and more angular coverage are needed to give a fuller comparison with the DWBA calculations in order to verify the interpretation given here.

Further attempts to measure the ^{15}O(α, γ) reaction rate by this method are planned. The analysis performed in the present work has indicated several areas where future measurements could be enhanced. Firstly, the major factor affecting the results of these experiments was the limited statistics. Increasing both the beam intensity and the running time would help to put the measurement of the 4.033 MeV state branching ratio within reach. Secondly, improved proton resolution would allow unambiguous identification of populated states and so a thinner target is recommended. Finally, better identification of the heavy residue would significantly improve the determination of the branching ratios by reducing background. This could be accomplished by using either a spectrometer or ΔE/E telescope to provide particle identification. A ΔE/E telescope may be the preferred option due to its potential for covering large solid angles. For example, the current LEDA detector could be used by placing a double sided transmission detector of similar dimensions in front of it. In addition to the particle identification capabilities, the improved phi resolution would allow trajectories to be reconstructed to aid in background subtraction.

Assuming the efficiency for detecting the tagging protons is the same, and the beamtime can be increased from 30 to 300 hours, then a beam intensity of about 10^8 pps is needed. If the target thickness is reduced, by say half, to improve the energy resolution, then a beam intensity of 10^9 pps is sufficient to provide the necessary statistics to verify the currently accepted theoretical value for the interesting state at 4.033 MeV. Such beam intensities are expected to become available in the near future[91].

However, if the statistics were insufficient to measure the 4.033 MeV branching ratio with high confidence, an additional check is possible with the set up described above. Knowing the absolute cross section for the population of the 4.033 MeV allows one to normalise a DWBA calculation. Assuming the shape of the calculated distribution is correct, this would allow one to predict the yield for the population of this state at forward angles, which is expected to be considerably higher than for backward angles. Although the kinematics restrict the identification of populated states in the case where the tagging proton is emitted forwards, if a proton event is detected as part of a triple coincidence, the excitation energy can be reconstructed from the alpha and ^{15}O information. Thus the yield of 4.033 MeV decay can be calculated and compared with the yield for its population derived from the DWBA, allowing the branching ratio to be determined.

Appendix A

Full level scheme for ^{19}Ne

Figure A.1: *Level scheme of* ^{19}Ne, *taken from Tilley et al.[58].*

Appendix B

Angles and Solid Angles

B.1   Detector Angles

Ring	θ[deg]
0	10.1
1	9.3
2	8.5
3	7.7
4	6.9
5	6.1
6	5.3
7	4.5

Table B.1: *Angles for LEDA1.*

Ring	θ[deg]	Ring	θ[deg]
0	31.6	8	22.9
1	30.6	9	21.7
2	29.6	10	20.5
3	28.5	11	19.3
4	27.4	12	18.1
5	26.3	13	16.8
6	25.2	14	15.5
7	24.1	15	14.2

Table B.2: *Angles for LEDA2.*

Ring	θ[deg] runI	θ[deg] runII	Ring	θ[deg] runI	θ[deg] runII
0	131.3	120.1	8	142.0	130.2
1	132.4	121.1	9	143.6	131.9
2	133.6	122.2	10	145.3	133.7
3	134.9	123.3	11	147.1	135.6
4	136.2	124.5	12	148.9	137.6
5	137.5	125.8	13	150.8	139.8
6	139.0	127.2	14	152.8	142.1
7	140.4	128.7	15	154.9	144.6

Table B.3: *Angles for LEDA3 for runI.*

Ring	$\Delta\phi$ [deg]	Ring	$\Delta\phi$ [deg]
0	18.1	8	39.7
1	28.0	9	39.7
2	35.1	10	39.7
3	39.7	11	39.7
4	39.7	12	39.7
5	39.7	13	39.7
6	39.7	14	39.7
7	39.7	15	39.7

Table B.4: *Values of $\Delta\phi$ for each strip in one LEDA sector.*

Sector	LEDA1	LEDA2	LEDA3
0	0.	270.	315.
1	45.	315.	0.
2	90.	0.	45.
3	135.	45.	90.
4	180.	90.	135.
5	225.	135.	180.
6	270.	180.	225.
7	315.	225.	270.

Table B.5: *Definition of ϕ for each sector in each LEDA.*

B.2 Solid angles

Ring	Ω[deg]
0	7.7
1	11.6
2	11.4
3	10.3
4	9.3
5	8.2
6	7.2
7	6.1

Table B.6: *Solid angles for LEDA1.*

Ring	Ω[msr]	Ring	Ω[msr]
0	19.8	8	43.2
1	34.8	9	41.8
2	43.3	10	40.2
3	48.2	11	38.5
4	47.5	12	36.7
5	46.6	13	34.6
6	45.6	14	32.5
7	44.5	15	26.4

Table B.7: *Solid angles for LEDA2.*

Ring	$\Omega[msr]$ (runI)	$\Omega[msr](runII)$	Ring	$\Omega[msr]$ (runI)	$\Omega[msr](runII)$
0	36.0	36.3	8	92.5	117.
1	57.3	59.1	9	93.0	122.
2	73.9	78.0	10	93.1	126.
3	85.4	92.4	11	92.6	131.
4	87.2	97.0	12	91.6	135.
5	77.8	102.	13	78.6	138.
6	90.4	107.	14	76.5	140.
7	91.6	112.	15	73.6	141.

Table B.8: *Solid angles for LEDA3.*

Appendix C

Details of triple alpha source

Isotope	Energy[MeV]	Percentage
^{239}Pu	5.105	11.5
	5.143	15.1
	5.155	73.3
^{241}Am	5.443	12.7
	5.486	86.0
^{244}Cm	5.764	23.3
	5.806	76.6

Table C.1: *Energy and alpha decay probabilities*

Appendix D

Energy Loss and

Transformation Formulae

D.1 Energy Loss Calculations

The method used to reconstruct the initial energy of a particle, knowing its energy after travelling through a medium as well as the thickness and composition of the medium, is based on the relationship between the range of the particle before and after it travels through the medium[76]. The range of the particle after the medium, R_f, can be calculated from the final energy, E_f, by

$$R_f = aE_f^b \qquad \text{(D.1)}$$

where a and b are parameters dependent on the medium and the incident particle. The range before the medium, R_i, is related to the range after by

$$R_f = R_i + d \qquad \text{(D.2)}$$

where d is the thickness of the medium. Finally, the initial energy is given by

$$E_i = (\frac{R_f}{a})^{1/b} \tag{D.3}$$

The parameters, a and b, were determined from GEANT simulations[92] and are given in table D.1 for protons in silicon and deuterated polyethylene.

Medium	a	b
Si	0.1289×10^{-2}	1.755
$(CD_2)_n$	0.1841×10^{-2}	1.832

Table D.1: *Parameters*

D.2 Transformation from proton energy to excitation energy

The excitation energy of the state populated in ^{19}Ne was reconstructed from the tagging proton energy by calculating the reaction Q value. From two body kinematics, the Q value is given by [93]

$$Q = \frac{1}{M_3}[M_1 E_1 + M_4 E_4 + M_3(E_4 - E_1) - 2(M_1 M_4 E_1 E_4)^{1/2} cos\theta] \tag{D.4}$$

where M_1 is the projectile mass, in this case ^{18}Ne; M_3 is the ejectile mass, in this case ^{19}Ne; M_4 is the recoil mass, in this case the proton; E_1 is the beam energy; E_4 is the recoil energy and θ is the emission angle of the recoiling particle. From this, the excitation energy can be calculated from

$$E_x = Q_o - Q \tag{D.5}$$

Here Q_o is the Q value for the population of the ground state.

D.3   Cross Section Formulae

The procedure used for calculating the centre of mass reaction cross sections was as follows

1. calculate the laboratory cross section, as described in Section 4.6, for the recoil

2. transform the recoil laboratory cross section into the ejectile laboratory cross section[94]

$$\sigma(\theta) = \sigma(\phi).\frac{sin^2\phi \ cos(\phi' - \phi)}{sin^2\theta \ cos(\theta' - \theta)} \tag{D.6}$$

Here θ relates to the ejectile angle and ϕ relates to the recoil angle. Primed quantities are in the centre of mass. The recoil and ejectile angles are related in the lab. by

$$\theta = arcsin\left[\left(\frac{M_4 E_4}{M_3 E_3}\right)^{1/2} sin\phi\right] \tag{D.7}$$

and the ejectile centre of mass angle is related to the lab. angle by

$$\theta' = arcsin\left[\left(\frac{E_3}{AE_T}\right)^{1/2} sin\theta\right] \tag{D.8}$$

where

$$\phi' = \pi - \theta' \tag{D.9}$$

$$E_3 = E_1 + Q - E_4; \quad E_T = E_1 + Q \tag{D.10}$$

and

$$A = \frac{M_2 M_4}{(M_1 + M_2)(M_3 + M_4)}\left(1 + \frac{M_1 Q}{M_2 E_T}\right) \tag{D.11}$$

3. transform the ejectile laboratory cross section into the ejectile centre of mass cross section

$$\sigma(\theta') = \sigma(\theta).\frac{sin^2\theta}{sin^2\theta'}cos(\theta' - \theta) \qquad (D.12)$$

Bibliography

[1] Sirius Science, Central Laboratory of the Research Councils Publication (1998), ISBN 0-90376-75-6.

[2] D. D. Warner, Proceedings of the Second International Conference on Radioactive Nuclear Beams (1992) pp139

[3] ISAC A Proposal for an Intense Radioactive Beams Facility, (1995)

[4] F. Kappeler, F.-K. Thielemann, M. Wiescher, Ann. Rev. Nucl. Part. Sci. **48** (1998) 175

[5] G. Wallerstein *et al*, Rev. Mod. Phys. **69** (1997) 995

[6] Opportunities in Nuclear Astrophysics - Origin of the Elements, White paper from Town Meeting, University of Notre Dame (1999), www.nscl.msu.edu/ austin/nuclear-astrophysics.pdf

[7] M. Wiescher *et al*, Phil. Trans. R. Soc. Lond. A **356** (1998) 2105

[8] E. M. Burbidge *et al*, Rev. Mod. Phys. **29** (1957) 547

[9] B. E. J. Pagel, "Nucleosynthesis and Chemical Evolution of the Galaxies", Cambridge University Press, Cambridge (1997)

[10] J. W. Truran, Ann. Rev. Nucl. Part. Sci. **34** (1984) 53

[11] M. V. Berry, "Principles of Cosmology and Gravitation", IOP Publishing Ltd, Bristol (1989)

[12] M. S. Longair, "High Energy Astrophysics, Vol.1: Particles, photons and their detection", Cambridge University Press, Cambridge (1997)

[13] S. Weinberg, "The First Three Minutes", Flamingo, London (1993).

[14] M. S. Longair, "High Energy Astrophysics, Vol.2: Stars, the Galaxy and the interstellar medium", Cambridge University Press, Cambridge (1997)

[15] M. Zeilik and S. A. Gregory, "Introductory Astronomy and Astrophysics", Saunders College Publishing, Orlando (1998)

[16] D. Arnett, "Supernovae and Nucleosynthesis", Princeton, University Press, Princeton (1996)

[17] C. E. Rolfs and W. S. Rodney, "Cauldrons in the Cosmos", The University of Chicago Press, Chicago (1988)

[18] H. A. Bethe and C. L. Critchfield, Phys Rev **54** (1938) 248

[19] D. Clayton, "Principles of Stellar Evolution and Nucleosynthesis", University of Chicago Press, Chicago (1983).

[20] H. A. Bethe, Phys. Rev. **55** (1939) 103

[21] C. F. von Weizsäcker, Physik Z. **38** (1937) 176

[22] C. F. von Weizsäcker, Physik Z. **39** (1938) 633

[23] M. Wiescher, Signatures of Nucleosynthesis in Explosive Stellar Processes.

[24] M. Wiescher *et al.*, Astron. Astrophys. **160** (1986) 56

[25] F. Hoyle, Ap. J. Suppl. **1** (1954) 121

[26] P. Tischhauser *et al.*, Proceedings of the Nuclei in the Cosmos V, Volos 1998, Editions Frontières, pp99

[27] N. P. T. Bateman *et al.*, Proceedings of the Nuclei in the Cosmos V, Volos 1998, Editions Frontières, pp103

[28] C. R. Brune *et al.*, Proceedings of the Nuclei in the Cosmos V, Volos 1998, Editions Frontières, pp107

[29] F. Käppeler, Proceedings of the Nuclei in the Cosmos V, Volos 1998, Editions Frontières, pp174

[30] D. Arnett, Ann. Rev. Astron. Astrophys. **33** (1995) 115

[31] S. E. Woosley *et al.*, Nucl. Pnys. **A621** (1997) 445c

[32] K. Nomoto *et al.*, Nucl. Phys. **A616** (1997) 79c

[33] S. Starrfield *et al.*, Mon. Not. R. Astron. Soc. **296** (1998) 502

[34] R. D. Gehrz *et al.*, Pub. Astron. Soc. Pac. **110** (1998) 3

[35] A. Kercek, Astron. Astrophys. **345** (1999) 831

[36] S. Wanajo *et al.*, Ap. J. **523** (1999) 409

[37] J. José and M. Hernanz, Ap. J. **494** (1998) 680

[38] R. E. Taam, Ann. Rev. Nucl. Part. Sci **35** (1985) 1

[39] A. E. Champagne and M. Wiescher, Ann. Rev. Nucl. Part. Sci. **42** (1992) 39

[40] R. K. Wallace and S. E. Woosley, Ap. J. Suppl. **45** (1981) 389

[41] G. Vancraeynest *et al.*, Nucl. Phys. **A616** (1997) 107c

[42] W. Bradfield-Smith *et al.*, Phys. Rev. **C59** (1999) 3402

[43] W. Bradfield-Smith, Ph.D. thesis, University of Edinburgh (1999)

[44] D. Groombridge *et al.*, Proceedings of the Nuclei in the Cosmos 2000, to be published

[45] J. Görres, M. Wiescher, and F. K. Thielemann, Phys. Rev. **C51** (1995) 392

[46] F. Rembges *et al.*, Astrophys. J. **484** (1997) 412

[47] H. Schatz *et al.*, Nucl Phys. **A621** (1997) 417c

[48] H. Schatz *et al.*, Phys. Rep. **294** (1998) 167

[49] R. D. Gehrz, Phys. Rep. **311** (1999) 405

[50] E. M. Sion, Phys. Rep. **311** (1999) 353

[51] K. M. Vanlandingham *et al.*, Mon. Not. R. Astron. Soc. **308** (1999) 577

[52] S. Starrfield, Phys. Rep. **311** (1999) 371

[53] K. Werner and B. Wolff, A & A **347** (1999) L9

[54] K. M. Vanlandingham *et al.*, Mon. Not. R. Astron. Soc. **290** (1997) 87

[55] J. Andreä *et al.*, A & A **291** (1994) 869

[56] P. V. Magnus *et al.*, Nucl. Phys. **A506** (1990) 332

[57] K. Langanke *et al.*, Ap. J. **301** (1986) 629

[58] D. R. Tilley *et al.*, Nucl. Phys. **A595** (1995) 1

[59] R.B. Firestone and V. S. Shirley (eds), "Table of Isotopes", 8th ed., Wiley, 1996

[60] C. Rolfs and C. A. Barnes, Ann. Rev. Nucl. Part. Sci. **40** (1990) 45

[61] P. V. Magnus *et al.*, Nucl. Phys. **A470** (1987) 206

[62] S. Wilmes *et al.*, Phys. Rev. **C52** (1995) R2823

[63] Z. Q. Mao *et al.*, Phys. Rev. Lett. **74** (1995) 3760

[64] P. D. Kunz and E. Rost, Computational Nuclear Physics 2, Ed.s K. Langanke, J. A. Maruhn and S. E. Koonin, Springer-Verlag, New York 1993

[65] F. de Oliveira *et al.*, Phys. Rev. **C55** (1997) 3149

[66] M. Wiescher, private communication

[67] S. Kubono *et al.*, Proceedings of the Nuclei in the Cosmos V, Volos 1998, Editions Frontières, pp409

[68] L. A. Riley *et al.*, Phys. Rev. Lett. 82 (1999) 4196

[69] UNIMONTE, A General Purpose Monte-Carlo Code for Break-up Reactions, Euan Macdonald, University of Edinburgh 1990

[70] K. Gul *et al.*, Nucl. Phys. **A122** (1968) 81

[71] A. N. Ostrowski *et al.*, J. Phys. (London) **G23** (1997) 1259 1

[72] D. Darquennes *et al.*, Phys. Rev. **C42** (1990) R804

[73] P. Decrock *et al.*, Proc. 2nd Int. Conf. on Radioactive Nuclear Beams, Louvain-la-Neuve, 1990

[74] R. Geller *et al.*, Ann. Rev. Nucl. Part. Sci. **40** (1990) 15

[75] G. Ryckewaert, private communication

[76] W. R. Leo, "Techniques for Nuclear and Particle Physics Experiments", Springer-Verlag 1994

[77] Micron Semiconductor Ltd, Lancing, UK.

[78] T. Davinson *et al.*, Nucl. Inst. Meth. **A** In press

[79] S. L. Thomas *et al.*, Nucl. Inst. Meth. **A288** (1990) 212

[80] J. R. Taylor, "An Introduction to Error Analysis", University Science Books, California 1997

[81] R. Bass, "Nuclear Reactions with Heavy Ions", Spinger-Verlag, Heidelberg 1980

[82] J. R. Comfort, Computer Phys. Commun. **16** (1978) 35

[83] J. M. Lohr and W. Haeberli, Nucl. Phys. **A232** (1974) 381

[84] C. M. Perey and F. G. Perey, Phys. Rev. **132** (1963) 755

[85] N. E. Davison *et al.*, Can. J. Phys. **48** (1970) 2242

[86] F. G. Perey, Phys. Rev. **131** (1963) 745

[87] G. R. Satchler, "Direct Nuclear Reactions", Oxford University Press, Oxford 1983

[88] H. T. Fortune *et al.*, Phys. Rev. **C18** (1978) 1563

[89] J. L. Alty *et al.*, Nucl. Phys. **A97** (1967) 541

[90] S. Sen *et al.*, Nucl. Phys. **A219** (1974) 429

[91] www.triumf.ca/people/baartman/ISAC

[92] GEANT simulations courtesy of Steven Morrow

[93] J. B. Marion and F. C. Young, "Nuclear Reaction Analysis", North-Holland Publishing Company, Amsterdam 1968

[94] P. Marmier and E. Sheldon, "Physics of Nuclei and Particles", New York Academic Press, New York (1969)